



PB99-149569

Development of Radar Techniques for Monitoring Bridge Deck Deterioration

**September 1998
Final Report**

Dr. Ram M. Narayanan, Scott G. Hudson and Chris J. Kumke

Department of Electrical Engineering
Center for Electro-Optics
209 N Walter Scott Engineering Center
University of Nebraska-Lincoln
Lincoln, NE 68588-0511

Mid-America Transportation Center

University of Nebraska-Lincoln
W333.2 Nebraska HallX
Lincoln, NE 68588-0530
Telephone: (402) 472-1974
Fax: (402) 472-0859
MATC Project No. MATC UNL97-4



Sponsored by:

Nebraska Department of Roads

1500 Nebraska Hwy 2
Lincoln, NE 68509
Telephone: (402) 479-4337
Fax: (402) 479-3884

DISCLAIMER

This document is disseminated under the sponsorship of the Department of Transportation, University Transportation Centers of University Research Institutes Program, in the interest of information exchange. The U.S. Government assumes no liability for the contents or use thereof.

REPRODUCED BY: **NTIS**
U.S. Department of Commerce
National Technical Information Service
Springfield, Virginia 22161

REPORT DOCUMENTATION PAGE			<i>Form Approved</i> OMB No. 0704-0188	
Public reporting burden for this collection of information is estimated to average 1 hour per response, including the time for reviewing instructions, searching existing data sources, gathering and maintaining the data needed, and completing and reviewing the collection of information. Send comments regarding this burden estimate to any other aspect of this collection of information, including suggestions for reducing this burden, to Washington Headquarters Services, Directorate for Information Operations and Reports, 1215 Jefferson Davis Highway, Suite 1204, Arlington, VA 22202-4302, and to the Office of Management and Budget, Paperwork Reduction Project (0704-0188), Washington, DC 20503.				
1. AGENCY USE ONLY (Leave Blank)		2. REPORT DATE September 1998	3. REPORT TYPE AND FINAL REPORT Final Report	
			PB99-149569	
4. TITLE AND SUBTITLE Development of Radar Techniques for Monitoring Bridge Deck Deterioration			5. FUNDING NUMBERS DTRS95-G-0007	
6. AUTHOR(S) Dr. Ram M. Narayanan, Scott G. Hudson and Chris J. Kumke				
7. PERFORMING ORGANIZATION NAME(S) AND ADDRESS(ES) Mid-America Transportation Center University of Nebraska-Lincoln W333.2 Nebraska Hall Lincoln, NE 68588-0530			8. PERFORMING ORGANIZATION REPORT NUMBER MATC UNL97-4	
9. SPONSORING / MONITORING AGENCY NAME(S) AND ADDRESS(ES) Nebraska Department of Roads 1500 Nebraska Hwy 2 Lincoln, NE 68509 Telephone: (402) 479-3884			10. SPONSORING / MONITORING NUMBER	
11. SUPPLEMENTARY NOTES				
12a. DISTRIBUTION/AVAILABILITY STATEMENT This document is available to the public			12b. DISTRIBUTION CODE	
13. ABSTRACT (Maximum 200 words) The use of ground-penetrating radar (GPR) systems to investigate civil engineering structures has become a topic of great interest since the 1970s. Of particular interest is the use of GPR to detect deterioration in bridge decks. As of 1994, an estimated 450% of the 578,000 highway bridges in the United States were deemed structurally unsound due to deterioration in the upper layer of the bridge deck. The majority of deterioration takes place as the embedded reinforcing steel (rebars) in the upper layer of concrete corrodes, increasing the potential of the formation of planar cracks, or delaminations, between successive rebars. Traditional methods, including a sounding method known as the chain drag method, are useful only after delaminations have become prominent. Two methods are presented in which the statistical variances of the radar return signals are used to determine if the reinforcing steel rebars are experiencing corrosion. Additionally, the methods are tested using two frequencies, 400 MHz and 900 MHz, to determine the effect of transmit frequency, if any, on the ability to detect corrosion. Results using these methods demonstrated that it was possible to determine the extent of individual rebar corrosion with respect to a sample of the bridge deck's best rebars, but could not determine the actual extent of corrosion.				
14. SUBJECT TERMS Ground-penetrating radar (GPR), Bridge Decks			15. NUMBER OF PAGES 147	
			16. PRICE CODE	
17. SECURITY CLASSIFICATION OF REPORT	18. SECURITY CLASSIFICATION OF THIS PAGE	19. SECURITY CLASSIFICATION OF ABSTRACT	20. LIMITATION OF ABSTRACT	
Unclassified	Unclassified	Unclassified		

NSN 7540-01-280-5500

Standard form 298 (Rev. 2-89)
Prescribed by ANSI Std. Z39-18

PROTECTED UNDER INTERNATIONAL COPYRIGHT
ALL RIGHTS RESERVED.
NATIONAL TECHNICAL INFORMATION SERVICE
U.S. DEPARTMENT OF COMMERCE

DISCLAIMER

This document contains
tone-on-tone or color
graphs, charts and/or pictures
which have been reproduced in
black and white.

DEVELOPMENT OF RADAR TECHNIQUES FOR MONITORING BRIDGE DECK DETERIORATION

ABSTRACT

The use of ground-penetrating radar (GPR) systems to investigate civil engineering structures has become a topic of great interest since the 1970's. Of particular interest is the use of GPR to detect deterioration in bridge decks. As of 1994, an estimated 40% of the 578,000 highway bridges in the United States were deemed structurally unsound due to deterioration in the upper layer of the bridge deck. The majority of deterioration takes place as the embedded reinforcing steel (rebars) in the upper layer of concrete corrodes, increasing the potential for the formation of planar cracks, or delaminations, between successive rebars. Traditional methods, including a sounding method known as the chain drag method, are useful only after delaminations have become prominent.

Two methods are presented in which the statistical variances of the radar return signals are used to determine if the reinforcing steel rebars are experiencing corrosion. Additionally, the methods are tested using two frequencies, 400 MHz and 900 MHz, to determine the effect of transmit frequency, if any, on the ability to detect corrosion. Results using these methods demonstrated that it was possible to determine the extent of individual rebar corrosion with respect to a sample of the bridge deck's best rebars, but could not determine the actual extent of corrosion. A review of existing literature on the topic is discussed, as well as basic GPR theory, computer simulations, and a description of the GPR system used. Results from experimental data taken on ten bridge decks is presented. The experimental results of six of these bridges are then compared to ground truth data obtained by the Nebraska Department of Roads using the chain drag method.

Acknowledgments

We wish to acknowledge the logistic support and ground truth data provided by David Hall, Michael Beacham, and others from the Nebraska Department of Roads.

Contents

Abstract	i
Acknowledgments	ii
Contents	iii
List of Figures	vi
List of Tables	xiv
1 Introduction	1
2 Literature Review	3
2.1 History	3
2.2 Bridge Deck Monitoring	4
2.2.1 Traditional Monitoring Methods	6
2.2.2 Pulsed Ground-Penetrating Radar Techniques	6
2.2.3 Frequency-Modulated, Continuous-Wave (FMCW) Ground-Penetrating Radar Techniques	10
2.2.4 Stepped-Frequency Ground-Penetrating Radar Techniques	12
2.2.5 Other Pulsed Radar Signal Processing Techniques	14
3 Ground Penetrating Radar Theory	16
3.1 Basic Electromagnetic Theory	16
3.1.1 Reflection Coefficient, Transmission Coefficient, and Relative Di- electric Constant	17
3.1.2 Antenna Radiation Pattern	19

3.1.3	Effects of Dielectric Constant on Velocity and Frequency	21
3.2	Radar Range Equation	23
3.3	Ground-Penetrating Radar System Operation	25
3.3.1	Choice of Transmitting Frequency	25
3.3.2	Acquisition of Radar Data	25
3.3.3	Other GPR System Parameters	29
4	Computer Simulations	31
4.1	Transmitted Waveform	31
4.2	Theoretical 1-D Return Waveform Analysis	34
4.2.1	Theoretical Radar Signature: Cases 1 and 2	35
4.2.2	Theoretical Radar Signature: Cases 3 and 4	38
4.3	Theoretical 2-D Return Waveform Analysis	41
4.3.1	Theoretical B-Scan: Cases 1 and 2	43
4.3.2	Theoretical B-Scan: Cases 3 and 4	43
5	Equipment Description	48
5.1	SIR System-10B	48
5.1.1	MF-10B Mainframe Unit	50
5.1.2	CD-10A Control/Display Unit	51
5.2	GS-608P Thermal Plotter/Printer	52
5.3	Antennas	53
5.4	Data Collection Software	56
5.5	<i>RADAN</i> Post-Processing Software	58
5.6	Van and Antenna Pullcart	62
6	Experimental Setup	64
6.1	Control Data Collection Setup	64
6.1.1	Construction of Bridge Deck Model	64

6.1.2	Calibration	64
6.1.3	Collection of Control Data	66
6.2	Experimental Bridge Deck Data Collection Setup	67
6.2.1	Bridges Studied	67
6.2.2	Calibration	67
6.2.3	Gridding the Bridge Deck	69
6.2.4	Log Sheet	69
6.2.5	Collection of Bridge Deck Data	70
6.2.6	Data Transfer and Back-Up	70
7	Experimental Results	72
7.1	Post-Processing	72
7.2	Data Analysis Procedure	73
7.3	Constant Threshold Level (CTL) Method	75
7.3.1	Model Bridge Deck Data Analysis Results	77
7.3.2	Ground Truth Data	78
7.3.3	Experimental Data Analysis Results	83
7.3.4	Comparison of Experimental 400 MHz Data With Ground Truth Data	100
7.3.5	Comparison of Experimental 900 MHz Data With Ground Truth Data	100
7.3.6	Comparison of Experimental 400 and 900 MHz Data With Ground Truth Data	108
7.3.7	General Observations Using Constant Threshold Level Method . .	108
7.4	Varying Threshold Level (VTL) Method	112
7.4.1	General Observations Using Varying Threshold Level Method . . .	113
8	Concluding Remarks and Future Research	126
	Bibliography	130

List of Figures

2.1	Delamination of a concrete bridge deck due to corrosion of the reinforcing rebar [<i>Warhus et al.</i> , 1997].	5
2.2	Differentiated monocycle waveform transmitted by the radar system used in experiments by Chung et al. [1992].	7
2.3	Expected return signal from an undamaged, reinforced concrete bridge deck with asphalt overlay [<i>Chung et al.</i> , 1992].	8
2.4	Expected return signal from a bridge deck with an air-filled delamination. (a) Component waveforms. (b) Total reflected waveform [<i>Chung et al.</i> , 1992].	9
2.5	Expected return signal from a bridge deck with a water-filled delamination. (a) Component waveforms. (b) Total reflected waveform [<i>Chung et al.</i> , 1992].	9
2.6	Plot of sign changes between points C and D (see previous figures) versus distance for data collected by Chung [<i>Chung et al.</i> , 1992].	10
2.7	Transmitted, received, and beat waveforms for an FMCW radar system [<i>Olver and Cuthbert</i> , 1988].	11
2.8	Typical FMCW radar return signal versus distance [<i>Daniels</i> , 1996].	13
2.9	Stepped-frequency radar profile of a rock surface 15 to 25 m beneath sandy soil [<i>Kong and By</i> , 1995].	15
3.1	Layers comprising the upper layer of a bridge deck.	17
3.2	Elliptical cone formed by the antenna radiation pattern in the ground [<i>Conyers and Goodman</i> , 1997].	20

3.3	Focusing and dispersion effects caused by increasing/decreasing the relative dielectric constant [<i>Conyers and Goodman, 1997</i>].	21
3.4	The convolution of the antenna radiation pattern with a point target creates a hyperbola in a wiggle plot [<i>Daniels, 1996</i>].	22
3.5	Sequential sampling technique utilized by most commercially available GPR systems, including GSSI's SIR System models.	28
4.1	Gaussian current pulse used to excite a 900 MHz GPR dipole antenna. . . .	32
4.2	Theoretical response of a 900 MHz antenna to the Gaussian current excitation shown in the previous figure.	33
4.3	Illustration of the four bridge deck cases considered for simulation.	34
4.4	Return waveforms from a Case 1 bridge deck. The incident signal is a 900 MHz pulse.	36
4.5	Return waveform from a Case 2 bridge deck. The incident signal is a 900 MHz pulse.	36
4.6	Return waveform from a Case 1 bridge deck. The incident signal is a 400 MHz pulse.	37
4.7	Return waveform from a Case 2 bridge deck. The incident signal is a 400 MHz pulse.	37
4.8	Return waveform from a Case 3 bridge deck. The incident signal is a 900 MHz pulse.	39
4.9	Return waveform from a Case 4 bridge deck. The incident signal is a 900 MHz pulse.	39
4.10	Return waveform from a Case 3 bridge deck. The incident signal is a 400 MHz pulse.	40
4.11	Return waveform from a Case 4 bridge deck. The incident signal is a 400 MHz pulse.	40

4.12	Three primary reflections from a bridge deck with an asphalt overlay (Cases 3 and 4). A second-time-around reflection within the asphalt layer can interfere with the reflection from a rebar [<i>Carter et al.</i> , 1986].	41
4.13	Layout of the model bridge deck considered for the two-dimensional simulations.	42
4.14	Theoretical B-scan for a Case 1-2 bridge deck. The incident signal is a 900 MHz pulse.	43
4.15	Theoretical B-scan for a Case 1-2 bridge deck with frequency loading considered. The incident signal is a 900 MHz pulse loaded down to 680 MHz. . . .	44
4.16	Theoretical B-scan for a Case 1-2 bridge deck. The incident signal is a 400 MHz pulse.	44
4.17	Theoretical B-scan for a Case 1-2 bridge deck with frequency loading considered. The incident signal is a 400 MHz pulse loaded down to 302 MHz. . . .	45
4.18	Theoretical B-scan for a Case 3-4 bridge deck. The incident signal is a 900 MHz pulse.	45
4.19	Theoretical B-scan for a Case 3-4 bridge deck with frequency loading considered. The incident signal is a 900 MHz pulse loaded down to 697 MHz. . . .	46
4.20	Theoretical B-scan for a Case 3-4 bridge deck. The incident signal is a 400 MHz pulse.	46
4.21	Theoretical B-scan for a Case 3-4 bridge deck with frequency loading considered. The incident signal is a 400 MHz pulse loaded down to 310 MHz. . . .	47
5.1	Simple block diagram of the SIR-10B radar system.	49
5.2	The SIR-10B ground-penetrating radar system (courtesy GSSI).	49
5.3	Sketch of the MF-10B mainframe unit [<i>GSSI</i> , 1996].	50
5.4	Sketch of the CD-10A control/display unit [<i>GSSI</i> , 1996].	52
5.5	Picture of the GS-608P thermal plotter/printer (courtesy GSSI).	53

5.6	Picture of the Model 5103 400 MHz antenna (courtesy GSSI).	54
5.7	Picture of the Model 3101D 900 MHz antenna (courtesy GSSI).	54
5.8	Menu structure of the data-collection software utilized by the SIR-10B radar system [GSSI, 1996].	57
5.9	Example of a <i>RADAN</i> color linescan image.	59
5.10	Example of a <i>RADAN</i> wiggle plot image.	59
5.11	Example of a <i>RADAN</i> oscilloscope trace.	60
5.12	View of the internal van set-up.	62
5.13	Picture of the pullcart designed for towing the antennas.	63
6.1	Layout of the bridge deck model constructed in the laboratory. The slab was constructed using pre-mixed Portland cement and contains a total of four rebars, two good and two corroded.	65
6.2	Illustration of how a bridge is gridded prior to data collection (top view). The filled squares indicate points where chalk marks are placed on the bridge deck and where fiduciary marks are placed on the data record.	69
6.3	Example of a log sheet completed in the field prior to collecting bridge deck data.	71
7.1	Example of variance plotted against scan number for a single survey line. Note that the plot appears “noisy.”	76
7.2	Data of the previous figure after averaging over 50 scans, which is the number of scans between two consecutive rebars. The bad sections of this particular survey line are easily seen at points A, B, and C.	76
7.3	Variance plotted against scan number for model bridge deck simulations assuming corroded rebar reflectivity of -0.35.	79

7.4	2-D plot representing deterioration areas of the model bridge deck according to the 400 MHz data.	80
7.5	2-D plot representing deterioration areas of the model bridge deck according to the 900 MHz data.	81
7.6	2-D plot representing deterioration areas of the model bridge deck agreed upon by both the 400 MHz and 900 MHz data sets.	82
7.7	2-D plot representing deterioration areas determined from a chain drag survey for the mile marker 33.50 (Highway 63) bridge.	83
7.8	2-D plot representing deterioration areas determined from a chain drag survey for the mile marker 34.87 (Highway 63) bridge.	84
7.9	2-D plot representing deterioration areas determined from a chain drag survey for the mile marker 37.20 (Highway 63) bridge.	85
7.10	2-D plot representing deterioration areas determined from a chain drag survey for the mile marker 32.95 (Highway 63) bridge.	86
7.11	2-D plot representing deterioration areas determined from a chain drag survey for the mile marker 14.41 (Highway 43) bridge.	87
7.12	2-D plot representing deterioration areas determined from a chain drag survey for the mile marker 14.60 (Highway 43) bridge.	88
7.13	2-D plot representing deterioration areas of the mile marker 14.41 (Highway 43) bridge according to the 400 MHz data. The bottom figure is the ground truth data and is provided for reference.	91
7.14	2-D plot representing deterioration areas of the mile marker 14.41 (Highway 43) bridge according to the 900 MHz data. The bottom figure is the ground truth data and is provided for reference.	92
7.15	2-D plot representing deterioration areas common to both the 400 and 900 MHz data for the bridge at mile marker 14.41 (Highway 43). The bottom figure is the ground truth data and is provided for reference.	93

7.16	2-D plot representing deterioration areas of the mile marker 14.60 (Highway 43) bridge according to the 400 MHz data. The bottom figure is the ground truth data and is provided for reference.	94
7.17	2-D plot representing deterioration areas of the mile marker 14.60 (Highway 43) bridge according to the 900 MHz data. The bottom figure is the ground truth data and is provided for reference.	95
7.18	2-D plot representing deterioration areas common to both the 400 and 900 MHz data for the bridge at mile marker 14.60 (Highway 43). The bottom figure is the ground truth data and is provided for reference.	96
7.19	2-D plot representing deterioration areas of the mile marker 33.50 (Highway 63) bridge according to the 400 MHz data. The bottom figure is the ground truth data and is provided for reference.	97
7.20	2-D plot representing deterioration areas of the mile marker 33.50 (Highway 63) bridge according to the 900 MHz data. The bottom figure is the ground truth data and is provided for reference.	98
7.21	2-D plot representing deterioration areas common to both the 400 and 900 MHz data for the bridge at mile marker 33.50 (Highway 63). The bottom figure is the ground truth data and is provided for reference.	99
7.22	2-D plot representing deterioration areas common to both the 400 MHz and ground truth data for the bridge located at mile marker 14.41 (Highway 43).	102
7.23	2-D plot representing deterioration areas common to both the 400 MHz and ground truth data for the bridge located at mile marker 14.60 (Highway 43).	103
7.24	2-D plot representing deterioration areas common to both the 400 MHz and ground truth data for the bridge located at mile marker 33.50 (Highway 63).	104
7.25	2-D plot representing deterioration areas common to both the 900 MHz and ground truth data for the bridge located at mile marker 14.41 (Highway 43).	105

7.26	2-D plot representing deterioration areas common to both the 900 MHz and ground truth data for the bridge located at mile marker 14.60 (Highway 43).	106
7.27	2-D plot representing deterioration areas common to both the 900 MHz and ground truth data for the bridge located at mile marker 33.50 (Highway 63).	107
7.28	2-D plot representing deterioration areas common to all three data sets for the bridge located at mile marker 14.41 (Highway 43).	109
7.29	2-D plot representing deterioration areas common to all three data sets for the bridge located at mile marker 14.60 (Highway 43).	110
7.30	2-D plot representing deterioration areas common to all three data sets for the bridge located at mile marker 33.50 (Highway 63).	111
7.31	2-D plot representing deterioration areas of the mile marker 14.41 (Highway 43) bridge according to the 400 MHz data (using VTL method). The bottom figure is the ground truth data and is provided for reference.	117
7.32	2-D plot representing deterioration areas of the mile marker 14.41 (Highway 43) bridge according to the 900 MHz data (using VTL method). The bottom figure is the ground truth data and is provided for reference.	118
7.33	2-D plot representing deterioration areas common to both the 400 and 900 MHz data for the bridge at mile marker 14.41 (Highway 43) (using VTL method). The bottom figure is the ground truth data and is provided for reference.	119
7.34	2-D plot representing deterioration areas of the mile marker 14.60 (Highway 43) bridge according to the 400 MHz data (using VTL method). The bottom figure is the ground truth data and is provided for reference.	120
7.35	2-D plot representing deterioration areas of the mile marker 14.60 (Highway 43) bridge according to the 900 MHz data (using VTL method). The bottom figure is the ground truth data and is provided for reference.	121

7.36	2-D plot representing deterioration areas common to both the 400 and 900 MHz data for the bridge at mile marker 14.60 (Highway 43) (using VTL method). The bottom figure is the ground truth data and is provided for reference.	122
7.37	2-D plot representing deterioration areas of the mile marker 33.50 (Highway 63) bridge according to the 400 MHz data (using VTL method). The bottom figure is the ground truth data and is provided for reference.	123
7.38	2-D plot representing deterioration areas of the mile marker 33.50 (Highway 63) bridge according to the 900 MHz data (using VTL method). The bottom figure is the ground truth data and is provided for reference.	124
7.39	2-D plot representing deterioration areas common to both the 400 and 900 MHz data for the bridge at mile marker 33.50 (Highway 63) (using VTL method). The bottom figure is the ground truth data and is provided for reference.	125

7.8	Comparison of Experimental 400 and 900 MHz Data (VTL Method)	115
7.9	Comparison of Experimental 400 MHz Data With Ground Truth (GT) Data (VTL Method)	115
7.10	Comparison of Experimental 900 MHz Data With Ground Truth (GT) Data (VTL Method)	116
7.11	Comparison of Experimental 400 and 900 MHz Data With Ground Truth (GT) Data (VTL Method)	116

List of Tables

3.1	Typical ϵ_r Values of Common Materials [<i>Conyers and Goodman, 1997</i>] . . .	19
3.2	Loaded Frequencies for GSSI Antennas When Coupled with Asphalt and Concrete	23
5.1	MF-10B Mainframe Specifications [<i>GSSI, 1996</i>]	50
5.2	CD-10A Control/Display Specifications [<i>GSSI, 1996</i>]	52
5.3	GS-608P Printer/Plotter Specifications [<i>GSSI, 1996</i>]	53
5.4	400 MHz Antenna Specifications [<i>Delea, 1996</i>]	55
5.5	900 MHz Antenna Specifications [<i>Delea, 1996</i>]	55
5.6	Pullcart Specifications	63
6.1	Radar Setup Parameters Used for Collecting Data	65
6.2	Bridges Studied	68
7.1	Variance Ratios Calculated From 1-D Computer Simulations	74
7.2	Threshold Levels Determined From Studies of the Model Bridge Deck . . .	78
7.3	Experimental Data Analysis Results	90
7.4	Comparison of Experimental 400 MHz Data With Ground Truth (GT) Data	101
7.5	Comparison of Experimental 900 MHz Data With Ground Truth (GT) Data	101
7.6	Comparison of Experimental 400 and 900 MHz Data With Ground Truth (GT) Data	108
7.7	Threshold Levels Necessary to Match Ground Truth Data	114

Chapter 1

Introduction

Thousands of bridges throughout the United States are experiencing deterioration due to heavy traffic and varying weather conditions, especially in locations where deicing agents are used [Warhus *et al.*, 1994]. In most bridges, particularly ones lacking an asphalt overlay, delamination tends to be the most prevalent type of deterioration [Chung *et al.*, 1992]. Delamination occurs as a result of the corrosion of the embedded steel reinforcement, or rebars. As two consecutive rebars corrode, the concrete around them weakens. Fracture planes (cracks) are formed between the rebars parallel to the top surface when weight is applied from vehicles passing over the area. Moisture and chloride ions become trapped in these cracks, causing the upper layer of the bridge deck to deteriorate at an accelerated rate. Maintenance required to retard or fix the problem is costing tax payers millions of dollars each year.

Traditionally, the chain drag survey has been the method of choice for determining the locations of delaminations in bridge decks [Chen *et al.*, 1994]. When using this method, a trained technician listens for differences in pitch as a chain is dragged across the bridge deck. Good concrete will emit high-pitched tones, while deteriorated concrete will emit low-pitched, dull tones. The areas determined to be delaminated are then highlighted on a two-dimensional plot representing a top view of the bridge deck. Although this method is fairly accurate, the technician conducting the survey must have extensive experience in deciphering these tones.

During the past few years, testing has shown that ground-penetrating, pulsed radar can be a viable tool for detecting and locating delaminations and other deterioration areas. The radar system transmits a pulse of very short duration (on the order of 1 nanosecond) into the ground and records the reflected waveform. Stable concrete and delaminated concrete each have their own unique reflected waveform, or "signature." Comparison of these signatures to theoretical simulations can lead to insight as to the locations of delaminations as well as the extent of the deterioration. The goal of the research described in this thesis is to further investigate the use of pulsed radar for such testing. The SIR System-10B, manufactured by Geophysical Survey Systems, Inc. in North Salem, NH, is the radar system used for recording the bridge deck data. Both 400 MHz and 900 MHz monostatic antennas are used to simultaneously collect data. The 900 MHz antenna, being at a higher frequency, provides better resolution than the 400 MHz antenna but does not penetrate as far into the ground.

A technique is used which involves calculating the variance, σ^2 , of each return signal to locate corroded rebars, and therefore deterioration areas, in the bridge deck. Intuitively, rebars with little or no corrosion will exhibit high reflectance and therefore high variance return signals. Rebars with a high level of corrosion should produce return signals with variances lower than that of non-corroded rebars. If no rebar is present, the return signal will not contain a return pulse from the rebar level and should exhibit the lowest variance of all three cases. The hope is that there will be agreement between the data sets taken with each antenna as to which areas of a bridge deck are deteriorated. The project is being partially funded by Mid-America Transportation Center (MATC) and the Center for Electro-Optics (CEO) at the University of Nebraska - Lincoln and is being done in conjunction with the Nebraska Department of Roads.

Chapter 2

Literature Review

2.1 History

Radar is an acronym for “*radio detection and ranging*.” Historically, the use of electromagnetic energy to detect remote metal objects was first accomplished by Hülsmeyer in 1904. However, it was not until 1910 that Leimbach and Löwy patented a technique for using electromagnetics to locate buried objects, particularly ore located at potential mining sites in Germany [Daniels, 1996]. An initial technique involved burying an array of dipole antennas in vertical boreholes and measuring the magnitude of the signal between a pair of transmit and receive antennas. In this way, an image could be formed of the area within the array. Eventually, the technique evolved into using separate transmit and receive antennas on the surface of the ground to record continuous-wave (CW) reflections from an interface or object below the surface.

In 1926, Hülsenbeck was the first to use pulsed techniques to determine the location and structure of subsurface features [Daniels, 1996]. Hülsenbeck noted that interfaces formed by materials with differing dielectric properties produced electromagnetic reflections. He also noted that electromagnetic techniques were more advantageous than traditional seismic techniques since electromagnetic energy could be directionally focused.

Work in the pulsed method gained momentum in the 1930’s with interest in investigating features beneath ice and rocks and even through water [Daniels, 1996]. Finally, in the late

1960's and early 1970's, ground-penetrating radar (GPR) established a foothold in the civil engineering field where nondestructive investigation of structural features became attractive. Interest was also taken in GPR techniques in the early 1970's to investigate lunar features [Daniels, 1996].

The range of applications in which GPR is used has grown steadily. Since the 1970's, GPR has seen use in the engineering field for structural and road analysis, void detection, and utility mapping. Environmental applications include locating underground storage tanks (UST's) and buried waste drums as well as assessing landfill sites. GPR has also proven extremely useful in geotechnical and mining areas for mapping regions of geological interest and locating ore at potential mine sites. In the archaeology field, GPR has been used to map ancient, buried structures. GPR has also been utilized by law enforcement agencies to locate clandestine graves and underground, man-made structures.

2.2 Bridge Deck Monitoring

As of 1994, there were approximately 578,000 highway bridges in the United States, 40% of which were either unsound structurally or functionally deficient [Warhus *et al.*, 1994]. If these bridges are not monitored and maintained properly, the probability for disaster can increase dramatically, with physical harm to users being the worst-case scenario.

Deterioration of a bridge occurs primarily in the upper part of the deck, just below the surface. Bridge decks can suffer from various forms of deterioration. Reinforced concrete bridge decks suffer primarily from delamination, while asphalt-covered bridge decks can also be susceptible to scaling and debonding [Chung *et al.*, 1992]. A *delamination* begins when the reinforcing rebars, located under approximately 5 cm of concrete cover and possibly up to 10 cm of asphalt pavement, begin to corrode due to prolonged exposure to chloride ions and moisture that intrude into the concrete [Warhus *et al.*, 1997]. The rebars are generally spaced at distances of 15.24 cm (6 in), 20.32 cm (8 in), or 30.48 cm (12 in) center-to-center

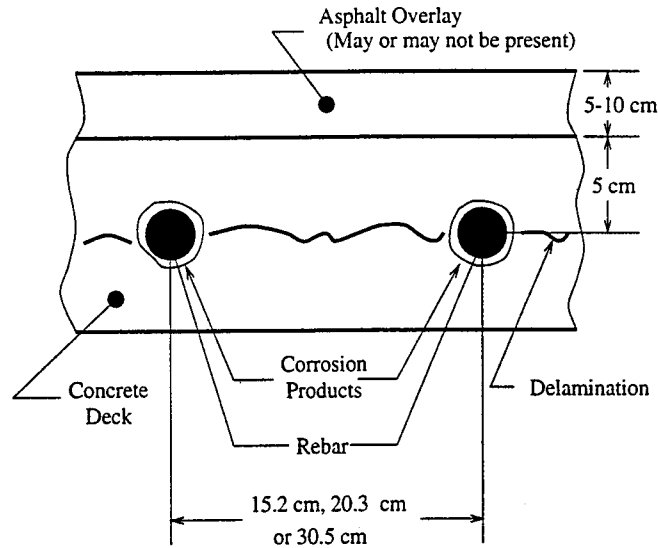


Figure 2.1: Delamination of a concrete bridge deck due to corrosion of the reinforcing rebar [Warhus *et al.*, 1997].

and are 1.3 cm (0.50 in) or 1.9 cm (0.75 in) in diameter [Hall, 1997]. A second layer of rebars is usually present approximately 30 cm above the bottom of the deck, but corrosion at this layer is virtually nonexistent [Hall, 1997]. As depicted in Figure 2.1 [Warhus *et al.*, 1997], the corrosion products weaken the concrete immediately surrounding the rebars, eventually causing a thin crack to form between adjacent rebars. This crack effectively *delaminates* the upper layer of the concrete from the remaining structure beneath. When a delamination occurs, the reinforcing function of the rebar members is effectively nullified, resulting in structural weakening and accelerated deterioration of the top surface.

When an asphalt overlay is present, scaling and debonding can also take place. *Scaling* is the reduction of concrete to a gravel-like texture due to the process of repeated freezing and thawing [Chung *et al.*, 1992]. Scaling occurs only at the asphalt-concrete interface. *Debonding* is the detachment of the asphalt overlay from the concrete, producing a small gap which can entrap air or moisture [Chung *et al.*, 1992]. Debonding differs from scaling only in the sense that there is no gravel-like concrete present in the debonded area. The majority of bridges in the United States are not overlaid with asphalt. Therefore, this research project focuses on determining areas of delamination.

2.2.1 Traditional Monitoring Methods

Traditionally, bridge deck assessment has been done by two main methods: the chain drag survey and chloride-ion content measurement [Chen *et al.*, 1994]. When conducting a chain drag survey, a trained technician listens for differences in pitch as a collection of chains is dragged across the bridge deck [Manning and Holt, 1983]. Good concrete will emit high-pitched tones, while deteriorated concrete will emit dull, low-pitched tones. Although this method can be fairly accurate, the technician conducting the survey must have extensive experience in deciphering these tones. The chain drag survey is usually limited to bridge decks with no asphalt overlay, since sonic reflections are excessively dampened by the asphalt.

The chloride-ion content measurement consists of physically drilling into the bridge deck to obtain cylindrical cores of the concrete. The cores are segmented horizontally and the amount of chloride per unit volume of concrete is measured. A high chloride-ion content is detrimental to concrete, expediting deterioration [Hall, 1997]. Not only is this method time-consuming and labor-intensive, obtaining core samples inflicts physical damage to the bridge deck.

2.2.2 Pulsed Ground-Penetrating Radar Techniques

Previous experiments using GPR techniques to evaluate the level of deterioration in bridge decks have been promising. The majority of experiments utilize pulsed radar systems, in which an extremely short pulse, on the order of 0.4 to 1.0 ns, is transmitted into the bridge deck. The pulse is transmitted at a pulse repetition frequency (PRF) of 25 kHz to 5 MHz. The reflected waveform is then received and analyzed for a given time window, generally from 0 to 10 ns for bridge deck evaluation. The depth to which a pulse will penetrate during this time window is dependent upon the material properties of the bridge deck.

Experiments done by Chung have shown good, consistent results [Chung *et al.*, 1992]. In his experiments, Chung employs an impulse radar system with a transmit pulse length

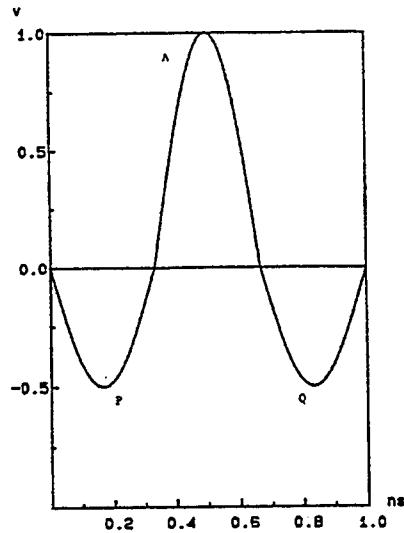


Figure 2.2: Differentiated monocycle waveform transmitted by the radar system used in experiments by Chung et al. [1992].

of 1 ns and 5 MHz PRF. A monostatic horn antenna, mounted on the front of a van, is used to couple the signal into the ground. The van is driven across the bridge deck in straight lines, commonly known as *survey lines*. The return signal is recorded during times when the antenna is not transmitting.

The form of the transmitted pulse used by Chung is a differentiated monocycle waveform, shown in Figure 2.2 [Chung et al., 1992]. The problem of calculating the return signal is solved in the same fashion as the traditional electromagnetic boundary-value problem. The expected signal return from an undamaged, reinforced concrete bridge deck with asphalt overlay is shown in Figure 2.3 [Chung et al., 1992]. The theory used to solve this problem is reserved for Chapter 3. The assumption is made that concrete is a more dense medium than asphalt. If not, the return from the concrete-asphalt interface would be 180° out of phase from the reflection shown in Figure 2.3.

Note the three peaks at A, C, and D resulting from the surface, concrete-asphalt interface, and rebars, respectively. Also note the W-shaped waveform between points C and D. Chung refers to this as the *characteristic W*. Although the distance between the two

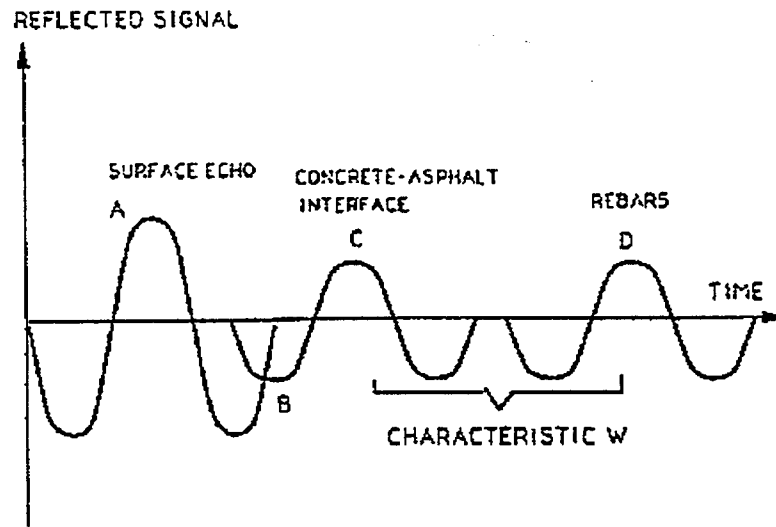


Figure 2.3: Expected return signal from an undamaged, reinforced concrete bridge deck with asphalt overlay [Chung *et al.*, 1992].

“wings” of the *W* will vary with the thickness of concrete over the rebar, other reflections should not occur between the two portions if the area is free of faults. The presence or lack of these *characteristic W* signatures in the experimental return waveforms are used by Chung to determine if an area of the deck is good or delaminated.

The delamination can contain dry air, water, or any moisture level in between. If the delamination contains air, the anticipated return signal will take the form shown in Figure 2.4 [Chung *et al.*, 1992]. Note the absence of the *characteristic W* found in the signature of a good deck. This is due to the 180° phase shift of the return signal from the less dense air-filled delamination. Figure 2.5 shows the signature of a delamination filled with water [Chung *et al.*, 1992]. Water is much more dense than concrete, causing the reflection to add “in-phase” with the *characteristic W*. This explains the highly accentuated *characteristic W* seen in the figure.

Determining the presence of the *characteristic W* in each return signal by inspection is not only cumbersome and time-consuming, but the results can vary depending on the person doing the evaluation. A simple procedure has been developed by Chung to automatically

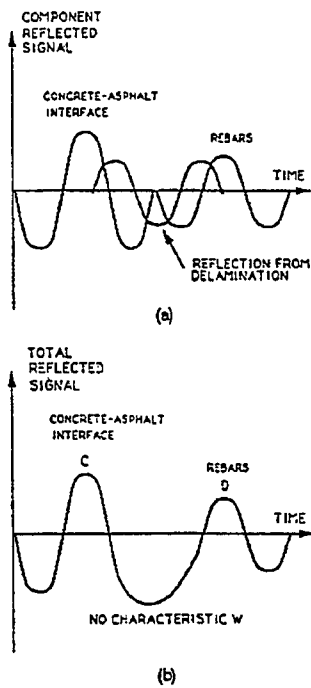


Figure 2.4: Expected return signal from a bridge deck with an air-filled delamination. (a) Component waveforms. (b) Total reflected waveform [Chung *et al.*, 1992].

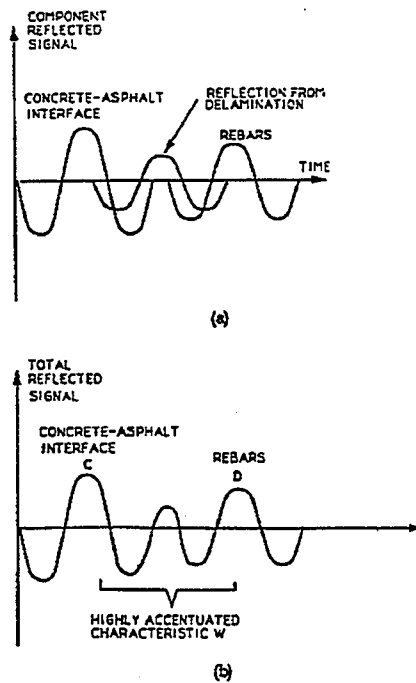


Figure 2.5: Expected return signal from a bridge deck with a water-filled delamination. (a) Component waveforms. (b) Total reflected waveform [Chung *et al.*, 1992].

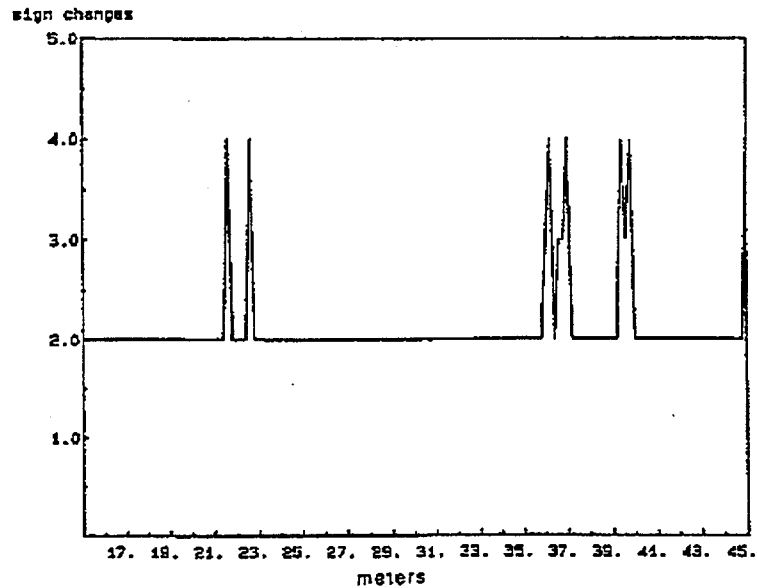


Figure 2.6: Plot of sign changes between points C and D (see previous figures) versus distance for data collected by Chung [Chung *et al.*, 1992].

determine whether or not the *characteristic W* exists. A computer program counts the number of sign changes that occur between points C and D. A good deck will exhibit more than two sign changes, provided that the amplitude of the center peak of the W is not excessive, which would indicate a water-filled delamination. Figure 2.6 shows a plot of sign changes versus distance for waveforms obtained by Chung for an asphalt-covered bridge deck [Chung *et al.*, 1992].

2.2.3 Frequency-Modulated, Continuous-Wave (FMCW) Ground-Penetrating Radar Techniques

Frequency-modulated, continuous-wave (FMCW) signals have been utilized for ground-penetrating radar systems, but their use has not been as widespread as pulsed signals [Daniels, 1996]. Compared to a pulsed radar system which is observed in the time domain, an FMCW system is observed in the frequency domain. The system transmits a carrier frequency which is continually changing in a linear fashion over a certain frequency range.

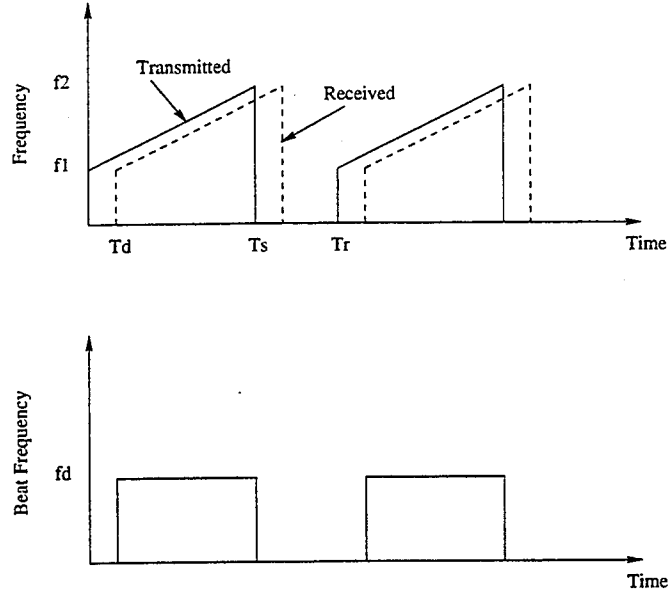


Figure 2.7: Transmitted, received, and beat waveforms for an FMCW radar system [Olver and Cuthbert, 1988].

This frequency “sweep” is continuously repeated at a certain rate, similar to the pulse repetition frequency (PRF) associated with pulsed systems. An intermediate frequency (IF) is produced by mixing the return signal with the transmitted signal. The difference frequency component of the IF is often referred to as the beat frequency (see Figure 2.7). Assuming only one target is present, the range is found by the relation

$$R = \frac{\nu T_d}{2} \quad (2.1)$$

where

R = range to target (m)

ν = velocity of propagation of the signal in the medium(m/s)

T_d = time delay between transmit and receive signals (s)

The beat frequency signal is manipulated in the frequency spectrum by taking the Fourier transform. This gives a spectrum related to the $\sin(x)/x$ (sinc) function with a

peak signal located at $\omega_d = 2(\omega_2 - \omega_1)T_d/T_s$, where ω_2 and ω_1 represent the highest and lowest frequencies of the sweep, respectively. Therefore, assuming the transmitted signal is transmitted for a time T_s , the beat frequency is [Olver and Cuthbert, 1988]

$$f_d = \frac{2(f_2 - f_1)R}{\nu T_s} \quad (2.2)$$

Note that f_d is directly proportional to the range R .

FMCW systems are sensitive to various parameters [Daniels, 1996]. If the frequency sweep is not highly linear with respect to time, the IF spectrum widens and degrades system resolution. The output frequency must also remain stable over time to allow comparison of measurements recorded at different times. Also, signal processing using the fast Fourier transform (FFT) is often insufficient. Therefore, alternative techniques are usually employed.

FMCW radar has been successful in certain applications, such as detecting buried pipes [Olver and Cuthbert, 1988] and detecting buried objects in wet snowpack [Yamaguchi et al., 1991]. Although the technique has not been widely used to evaluate bridge decks, doing so looks promising. A typical FMCW radar return signal is shown in Figure 2.8.

2.2.4 Stepped-Frequency Ground-Penetrating Radar Techniques

Stepped-frequency signals are considered continuous sinusoidal signals with sequentially changing frequency [Kong and By, 1995]. The signal is expressed as [Kong and By, 1995]

$$f(t) = Ae^{j2\pi(f_1 + n\Delta F)t} \quad (2.3)$$

for

$$(n-1)T/N \leq t < nT/N \quad \text{and} \quad 0 \leq n \leq N-1$$

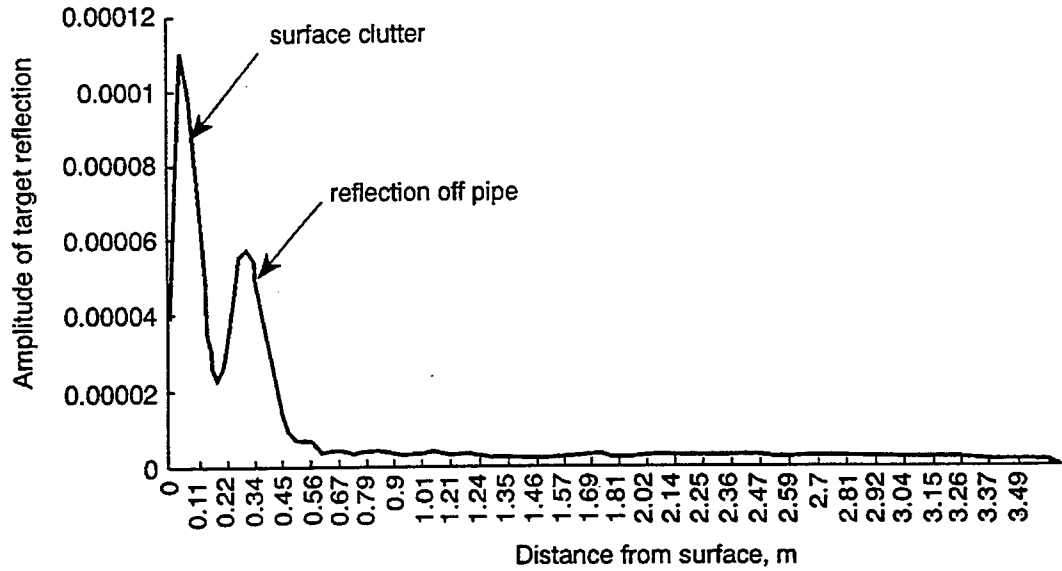


Figure 2.8: Typical FMCW radar return signal versus distance [*Daniels, 1996*].

where A is the signal amplitude, T is the signal period, N is the number of frequency steps (usually a power of 2 for processing purposes), f_1 is the frequency of the first step, ΔF is the frequency step size, and n is an integer.

These signals can be used as radar transmit signals. The radar transmits the sequence of N frequencies, usually by means of a network analyzer. The amplitude and phase of the received signal is recorded after downconversion. Like the FMCW radar system, received signals are operated upon in the frequency domain. An algorithm such as an inverse fast Fourier transform (IFFT) is used to convert the frequency-domain signal into a time-domain signal. Targets at the ambiguous range and greater are recorded, where the ambiguous range is given by [*Daniels, 1996*]

$$R_{amb} = N\Delta R \quad (2.4)$$

and ΔR is the range resolution, given by [*Daniels, 1996*]

$$\Delta R = \frac{v}{2N\Delta F} \quad (2.5)$$

ν , as before, is the velocity of propagation through the medium.

The *detection figure of merit*, D , of a GPR system is defined as the ratio of the maximum target detection distance to the distance resolution. Assuming that R_{amb} is equal to the maximum detection distance, D for a pulsed system is given as [Kong and By, 1995]

$$D = \frac{1}{2}TB = \frac{B}{2f_r} \quad (2.6)$$

where T is the pulse period, $f_r = 1/T$ is the pulse repetition frequency (PRF), and B is the signal bandwidth. Note that D is inversely proportional to the PRF.

For a stepped-frequency system, D is found by [Kong and By, 1995]

$$D = \frac{B}{2\Delta F} = \frac{1}{2}N \quad (2.7)$$

where B , ΔF , and N are as before. Therefore, D is dependent only upon the number of frequency steps, which can be varied when using a network analyzer. D is usually set to match the ground conditions [Kong and By, 1995]. Kong and By [1995] have been successful in using stepped-frequency techniques to obtain subsurface data. Figure 2.9 shows a radar profile of a rock surface beneath sandy soil recorded using a stepped-frequency system [Kong and By, 1995].

2.2.5 Other Pulsed Radar Signal Processing Techniques

Experiments using other signal processing techniques have yielded good success. A project sponsored by the Strategic Highway Research Program (SHRP) involved training a neural network to recognize various anomalies and faults in the pavement of highways and bridges [Smith and Scullion, 1993]. The neural network was trained using modeled data and tested using real data. Since results varied between different sections of pavement, training the neural network to recognize certain features was often difficult.

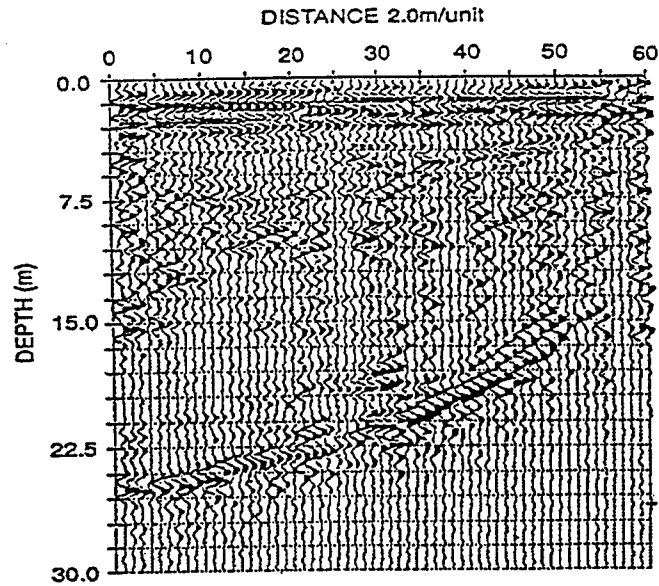


Figure 2.9: Stepped-frequency radar profile of a rock surface 15 to 25 m beneath sandy soil [Kong and By, 1995].

Recently, work has been done using short-time Fourier transforms (STFT) and wavelet transforms (WT) to develop target recognition schemes from data collected by ground-penetrating radar systems [Daniels, 1996]. STFT theory utilizes the traditional Fourier transform to sequentially analyze small segments, or “windows,” of the total signal. Wavelet analysis takes the STFT one step further by allowing for variable window sizes. Research methods using these techniques are still in their infancy.

Chapter 3

Ground Penetrating Radar Theory

Before developing or evaluating any technique to solve a particular problem, it is helpful to gain some insight as to the outcome that may be expected from the application of the technique. In other words, one should have a theoretical model to which experimental results can be compared.

The following chapter gives a brief discussion of basic ground-penetrating radar theory. The theory is put to use in Chapter 4 to generate a computer simulation which models electromagnetic returns from the top layer of a bridge deck.

3.1 Basic Electromagnetic Theory

The propagation of an electromagnetic plane wave, assuming a time-harmonic dependence and traveling in the positive z -direction, is governed by the equation [Johnk, 1988]

$$\vec{E}(z, t) = \hat{a}_t E_m^+ e^{-\alpha z} \cos(\omega t - \beta z + \phi^+) \quad (3.1)$$

where

\vec{E} = electric field vector

\hat{a}_t = unit vector in transverse (i.e. x - y) plane

E_m^+ = amplitude of the electric field

α = attenuation constant

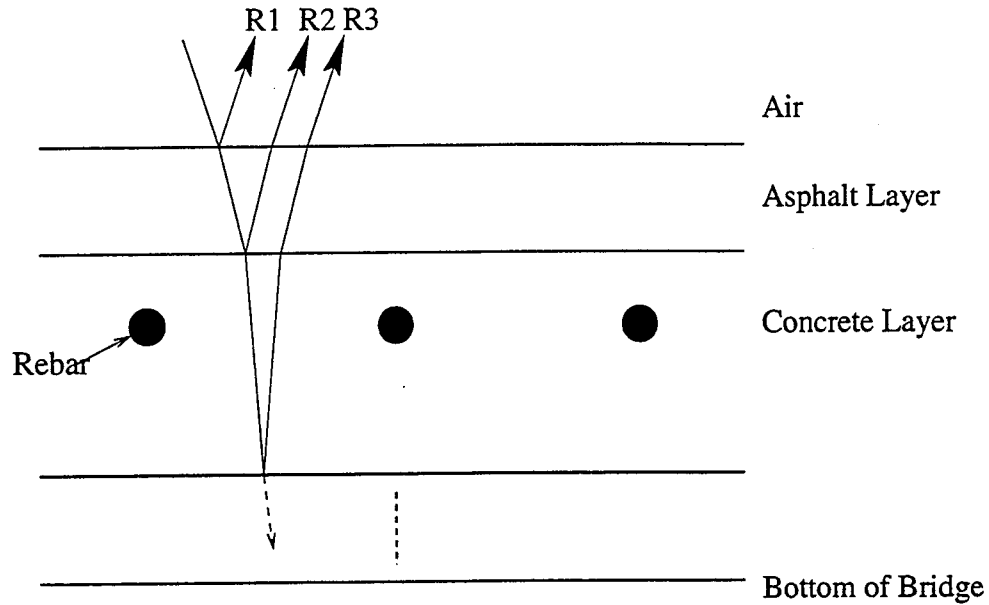


Figure 3.1: Layers comprising the upper layer of a bridge deck.

β = phase constant

ϕ^+ = phase

ω = wave frequency

For low loss dielectrics, α is usually considered negligible and $\beta = \omega\sqrt{\mu_o\epsilon_o\epsilon_r}$. The permeability of free space, μ_o , is $4\pi \times 10^{-7}$ H/m, the permittivity of free space, ϵ_o , is 8.8545×10^{-12} F/m, and ϵ_r is the relative dielectric constant of the dielectric.

3.1.1 Reflection Coefficient, Transmission Coefficient, and Relative Dielectric Constant

The subsurface of a bridge deck can be considered a multi-layer structure, with each layer having unique electrical properties, as shown in Figure 3.1.

An interface is formed between layers of contrasting electrical properties. Due to this contrast, a portion of a signal's energy incident upon the interface will be transmitted through the interface, continuing on to the next interface. The remaining energy is reflected back. The amount of energy reflected from or transmitted through an interface, relative

to the total energy incident upon it, is dependent upon the extent of the contrast. These values can be quantified by the *reflection and transmission coefficients* at the interface. For nonconducting materials such as dry asphalt and concrete, the reflection and transmission coefficients are given by, respectively [Chen et al., 1994]

$$\Gamma = \frac{\sqrt{\epsilon_{r1}} - \sqrt{\epsilon_{r2}}}{\sqrt{\epsilon_{r1}} + \sqrt{\epsilon_{r2}}} \quad (3.2)$$

and

$$T = \frac{2\sqrt{\epsilon_{r1}}}{\sqrt{\epsilon_{r1}} + \sqrt{\epsilon_{r2}}} \quad (3.3)$$

where

Γ = reflection coefficient

T = transmission coefficient

ϵ_{r1} = relative dielectric constant of overlying material

ϵ_{r2} = relative dielectric constant of underlying material

Although the conductivity, σ , of some materials can greatly affect the response of an electromagnetic wave, it is generally very small for materials dealt with in this thesis and will be neglected. However, the reflection coefficient of a *purely conducting* material, such as the reinforcing steel bars found in bridge decks, is taken to be approximately -1 [Johnk, 1988].

The relative dielectric constant is the ratio of a material's electrical permittivity to the electrical permittivity of free space, or $\epsilon_o = 8.854 \times 10^{-12} \text{ farads/m}$ [Johnk, 1988]. Note that $\epsilon_r = 1$ for free space. The relative dielectric constant of a given material is dependent upon many features of the material, including moisture content, temperature, and density, and is generally difficult to accurately measure in the field. Table 3.1 gives typical values of ϵ_r for a variety of common geological materials [Conyers and Goodman, 1997].

Table 3.1: Typical ϵ_r Values of Common Materials [*Conyers and Goodman, 1997*]

Air	1
Freshwater	80
Seawater	81-88
Ice	3-4
Dry Sand	3-5
Saturated Sand	20-30
Coal	4-5
Clay	5-40
Average Surface Soil	12
Concrete	6-8
Asphalt	3-5

Note that if ϵ_r is greater in the latter layer than in the former layer ($\epsilon_{r1} < \epsilon_{r2}$), the reflection coefficient will be negative. The result is a reflected wave which is 180° out-of-phase with respect to the incident wave [*Daniels, 1996*].

3.1.2 Antenna Radiation Pattern

The radiation pattern of antennas used in ground-penetrating radar work generally takes the form of an elliptical cone with the apex located at the center of the transmitting antenna. Figure 3.2 shows a visual representation of this pattern [*Conyers and Goodman, 1997*]. Most of the reflected energy is concentrated in the center portion of the cone. This area is called the *first Fresnel zone*. In order to minimize signal returns from either side of a survey line, the antenna is aligned so that the major axis of the footprint is in the direction of travel (with the survey line). The radius of the major axis of the first Fresnel zone is given by [*GSSI, 1995*]

$$A = \sqrt{\lambda \left(D + \frac{\lambda}{4} \right)} \quad (3.4)$$

where

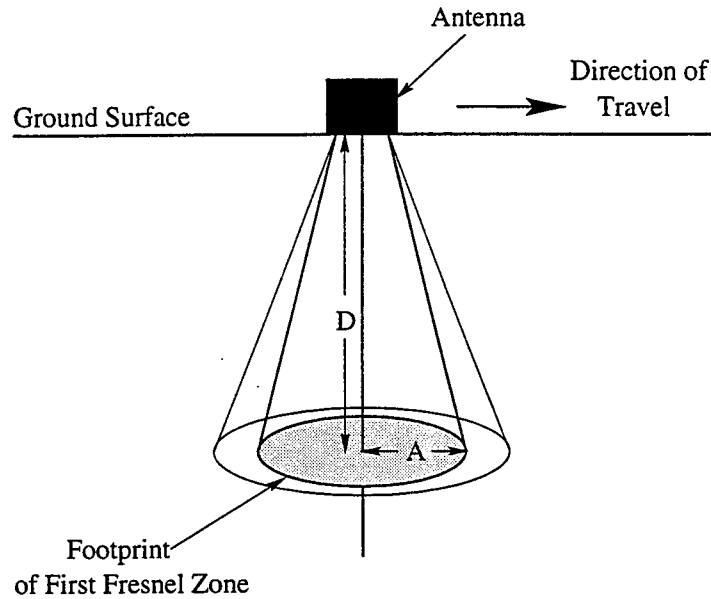


Figure 3.2: Elliptical cone formed by the antenna radiation pattern in the ground [Conyers and Goodman, 1997].

A = major axis radius of first Fresnel zone

λ = wavelength of center frequency

D = distance from antenna to footprint (perpendicular to footprint)

For the 400 MHz and 900 MHz antennas used in this research project, the 3 dB beamwidth, in air, is 90° along the direction of travel and 60° perpendicular to the direction of travel. When the antenna is coupled with a dielectric medium, however, the cone becomes more or less focused depending on ϵ_r of the medium. The effect on footprint size due to focusing/dispersion is taken into account in Equation (3.4). Figure 3.3 illustrates the focusing and dispersion effects on the illumination cone as the dielectric constant increases (focusing) and decreases (dispersion) through a sequence of layers [Conyers and Goodman, 1997]. The amount of focusing or dispersion from layer to layer is a function of Snell's Law.

Due to the radiation pattern of the antenna, a point target will start to be detected when the front edge of the pattern reaches it. The travel time of the signal to and from the target is greatest at the edges of the beam pattern and shortest when the antenna is directly

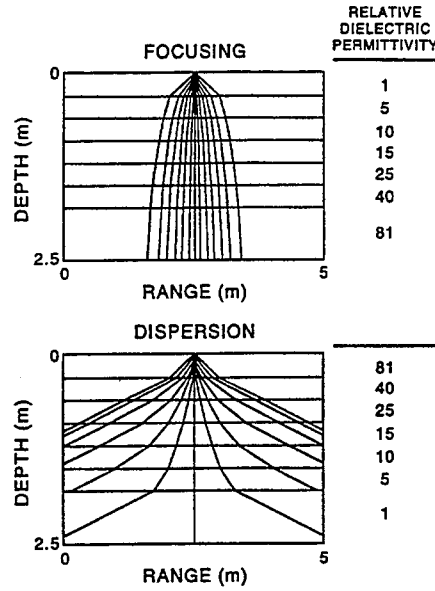


Figure 3.3: Focusing and dispersion effects caused by increasing/decreasing the relative dielectric constant [Conyers and Goodman, 1997].

it. As the antenna moves over the target, a hyperbola is formed on the wiggle plot. The hyperbola can be thought of as the result of convolving the point target with the antenna radiation pattern. An illustration is shown in Figure 3.4 [Daniels, 1996].

3.1.3 Effects of Dielectric Constant on Velocity and Frequency

The velocity of a radar wave in a dielectric medium can be estimated by [Daniels, 1996]

$$\nu = \frac{c}{\sqrt{\epsilon_r}} \quad (3.5)$$

where ν is the velocity of propagation in m/s and c is the speed of light (3×10^8 m/s).

The time taken for a wave to traverse from one interface, reflect off a second interface, and travel back to the first interface is known as the *round-trip*, or *two-way*, travel time for a wave within the medium bounded by the two interfaces. This is computed by [Daniels, 1996]

$$t_r = \frac{2d}{\nu} = \frac{2d\sqrt{\epsilon_r}}{c} \quad (3.6)$$

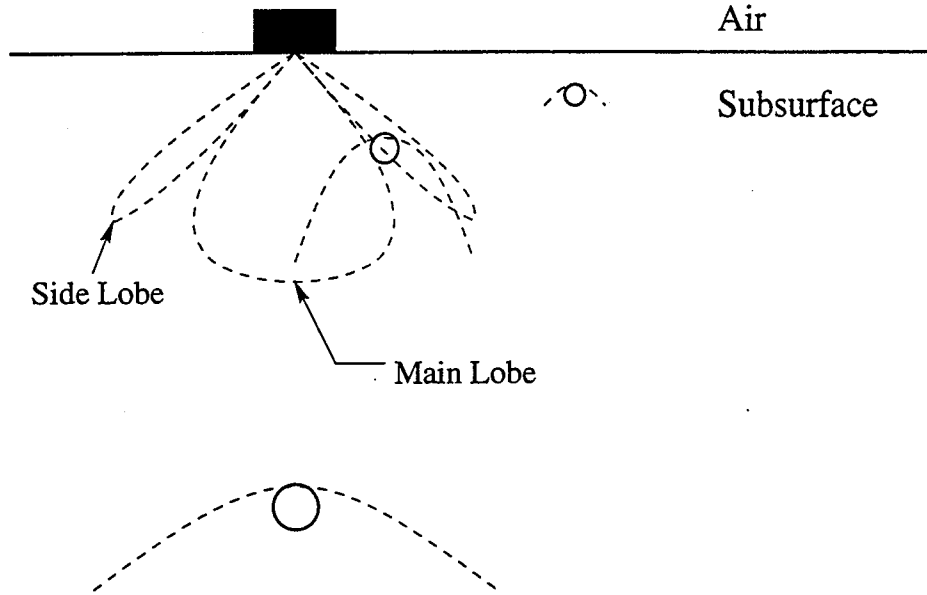


Figure 3.4: The convolution of the antenna radiation pattern with a point target creates a hyperbola in a wiggle plot [Daniels, 1996].

where

t_r = round-trip travel time (s)

d = distance from interface 1 to interface 2 (m)

and ν and ϵ_r are as above. Calculation of the round-trip travel time in each layer is necessary for computing the total reflected wave at the source.

From the discussion above, it would make sense that the frequency of the signal within a medium is calculated by

$$f_{medium} = \frac{f_o}{\sqrt{\epsilon_r}} \quad (3.7)$$

where f_o is the center frequency of the signal in air. However, to maximize the amount of energy being coupled into the ground, a dipole antenna should be placed as close to the ground as possible, no more than one wavelength away [GSSI, 1996]. When coupled with the ground, which has a higher dielectric constant than air, the effective center frequency

Table 3.2: Loaded Frequencies for GSSI Antennas When Coupled with Asphalt and Concrete

GSSI Model No.	f_o Air (MHz) $\epsilon_r = 1$	f_L Asphalt (MHz) $\epsilon_r = 5$	f_L Concrete (MHz) $\epsilon_r = 7$
5103	400	310	302
3101D	900	697	680

decreases. The loading of the antenna by the ground is a phenomenon known as *frequency loading*. When coupled with a medium whose dielectric constant is $1 \leq \epsilon_r \leq 15$, the loaded frequency, f_L , caused by the medium is given by [Delea, 1996]

$$f_L = \frac{f_o}{\sqrt{\frac{2}{1+\frac{1}{\epsilon_r}}}} \quad (3.8)$$

The effects of frequency loading should be accounted for when calculating the frequency within a medium. Table 3.2 gives the values of loaded frequencies for two GSSI antennas when coupled with asphalt and concrete.

3.2 Radar Range Equation

When designing a ground-penetrating radar system, designers start with the classical radar range equation. The reflected power received from a target below the subsurface, using a monostatic antenna (a single antenna which transmits as well as receives), can be found by the radar range equation, given by [Hamran et al., 1995]

$$P_R = \frac{P_T G^2 \lambda^2 \sigma e^{-2\alpha R}}{(4\pi)^3 R^4} \quad (3.9)$$

where

P_R = received power

P_T = transmitted power

G = gain of the monostatic antenna

λ = wavelength in the subsurface medium

σ = radar scattering cross section of target

α = attenuation coefficient of subsurface medium

R = range to target

The signal-to-noise ratio of the a radar system is then found by [Hamran *et al.*, 1995]

$$\left(\frac{S}{N}\right) = \left(\frac{E_T C_M G^2}{k_B T_o F_N}\right) \left(\frac{\lambda^2 \sigma e^{-2\alpha R}}{(4\pi)^3 R^4}\right) \quad (3.10)$$

where

E_T = transmitted energy

C_M = receiver matching coefficient

k_B = Boltzman's constant (1.38×10^{-23} J/K)

T_o = system temperature (290 K)

F_N = system noise factor

E_T is found by integrating the transmitted power over the pulse duration. For a pulsed system using sequential sampling theory (to be discussed later), $C_M = 1/n_p$, where n_p is the number of samples needed to digitally reconstruct one received trace.

Finally, the dynamic range (DR) of the system is found. The dynamic range is the main parameter which characterizes the amount of penetration a system will have, and is expressed as [Hamran *et al.*, 1995]

$$DR = \frac{P_{T,avg} \tau_i C_M G^2}{k_B T_o F_N} \quad (3.11)$$

$P_{T,avg}$ is the average power transmitted over a time period τ_i (usually one second). When designing a GPR system, maximizing the dynamic range is critical to system performance. Hamran *et al.* [1995] discuss the dynamic range of various GPR systems in more detail.

3.3 Ground-Penetrating Radar System Operation

3.3.1 Choice of Transmitting Frequency

The range resolution in air for a radar system is approximately [Skolnik, 1980]

$$\Delta R \cong \frac{c\tau}{2} \quad (3.12)$$

where c is the speed of light and τ is the transmitted pulse width. Modifying this equation for a medium with dielectric constant ϵ_r gives the range resolution for a pulsed GPR system, which is

$$\Delta R \cong \frac{c\tau}{2\sqrt{\epsilon_r}} \quad (3.13)$$

The range resolution, ΔR , is the minimum distance that a pulse of duration τ can resolve. It should be noted that for pulsed GPR systems, the transmitted pulse is a single bipolar pulse. This is unlike conventional pulsed radar in which the transmitted pulse is actually the envelope of multiple cycles of a waveform. In GPR work, the pulse length must be chosen so that ΔR is less than the thickness of the thinnest layer of interest. In other words, for closely spaced subsurface layers, a short pulse length (high frequency) must be used. The consequence of using a higher frequency, however, is a decrease in the depth of signal penetration. Choosing the correct pulse frequency becomes very important, with desired range resolution and depth of penetration being the dominant factors. It should be noted that antenna size also increases with decreasing frequency.

3.3.2 Acquisition of Radar Data

Before acquiring GPR data, certain basic parameters must be set within the radar system. These parameters are dependent upon the application and environmental conditions. Correctly setting system parameters ensures that sound data is recorded in proper fashion. The

basic parameters are the time window, samples per scan, pulse repetition frequency (PRF), scans per second, and scan stacking.

The *time window* is generally the first parameter decided upon. It is the amount of time that the system will receive and record reflected energy [Conyers and Goodman, 1997]. When using a monostatic antenna, the time window is turned on just after the radar pulse is transmitted. The minimum length of the time window can be estimated using Equation (3.6) if the approximate material properties (ϵ_r) and depth to the furthest features of interest are known. The length of the time window should always be slightly overestimated so that data is not missed if material properties change or if subsurface features dip dramatically. A time window of 10 to 20 ns was found to be a good choice for bridge deck investigation.

After setting the time window, the number of *samples per scan* must be chosen. A GPR system digitally samples the reflected waveform using an A/D converter. The samples per scan is the total number of samples used to reconstruct the original reflected waveform. The more samples used, the better the approximation. For GSSI systems, the number of samples per scan is specified as a power of two: 128, 256, 512, 1024, or 2048. A setting of 256 samples per scan was used when collecting data for this research project.

The resolution (time between samples), ΔT_n , can be found by dividing the time window by the number of samples per scan, or

$$\Delta T_n = \frac{\text{Length of time window}}{\text{Samples per scan}} \quad (3.14)$$

For example, if 256 samples are used to digitally represent a signal within a 10 ns time window, the resolution would be $10 \text{ ns} / 256 \text{ samples} = 39 \text{ ps/sample}$. The Nyquist theorem states that the sampling rate must be twice the frequency of the highest frequency present in the signal. The 3 dB bandwidth for GSSI antennas is approximately equal to the center frequency [GSSI, 1995]. Therefore, a pulse transmitted at a 900 MHz center frequency will

have a 3 dB bandwidth extending from 450 MHz to 1,350 MHz. The minimum sampling frequency must be at least $2 \times 1,350 \text{ MHz} = 2,700 \text{ MHz}$ according to the Nyquist theorem. The fastest sample-and-hold circuitry commercially available has a sampling rate of approximately 3,000 MHz (3 GHz), but is extremely expensive and could not be used when transmitting with higher-frequency antennas such as 2.5 GHz [Delea, 1997]. To overcome this problem, a technique known as *sequential sampling* or *time-domain repetitive sampling* is used [Conyers and Goodman, 1997; Hamran et al., 1995]. This technique is utilized in digital oscilloscope technology. A composite radar scan is formed by recording a single sample from each transmitted pulse in a series of pulses. Figure 3.5 illustrates this concept. If 256 samples per scan is specified, then a series of 256 transmitted pulses is required to form one radar scan.

The rate at which a pulsed radar system transmits pulses is known as the *pulse repetition frequency* (PRF). The PRF for commercially available systems ranges from a few thousand hertz to approximately one megahertz. The maximum PRF for the GSSI SIR-10B radar system is 100 kHz. The transmit rate must be set properly to ensure good horizontal resolution, which is determined by the speed at which the antenna moves along the ground as well as the number of *scan per second* recorded by the system. The number of scans per second is dependent upon both the number of samples per scan and the PRF. It is found by

$$\text{Scans/Sec} = \frac{\text{PRF}}{\text{Samples per scan}} \quad (3.15)$$

Therefore, the PRF is adjusted to meet the desired samples per scan and scans per second. Consider an example in which it is desired to record 50 scans per second using 256 samples per scan. The minimum PRF must be $50 \text{ scans/sec} \times 256 \text{ samples/scan} = 12.8 \text{ kHz}$. If the PRF is set to four times this frequency, or 51.2 kHz, every fourth return trace will be sampled.

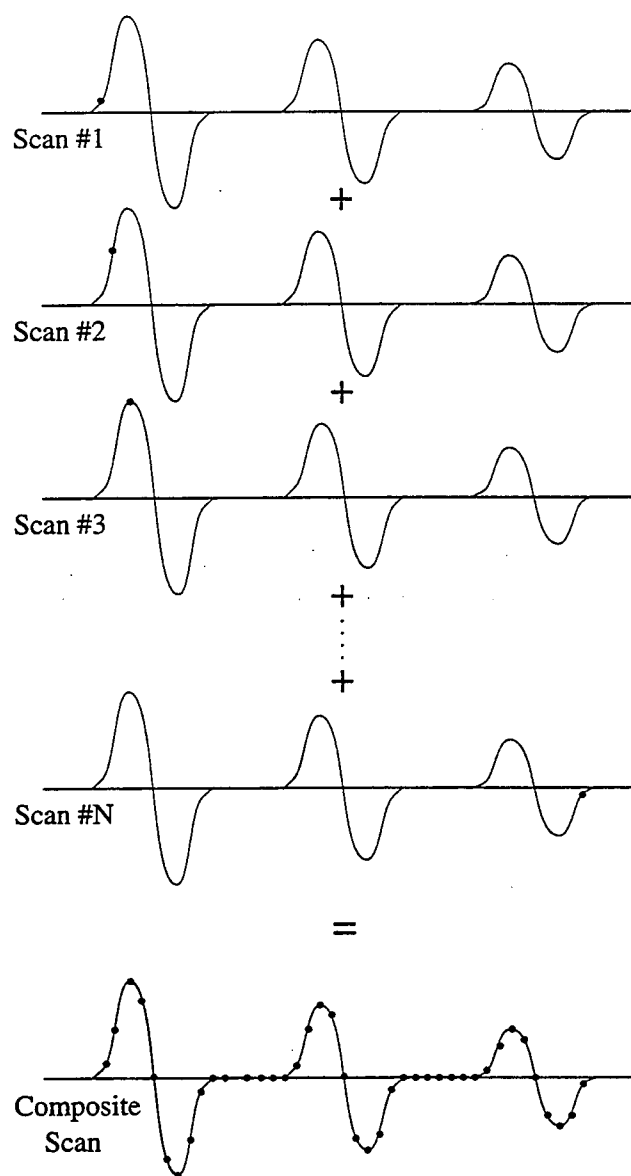


Figure 3.5: Sequential sampling technique utilized by most commercially available GPR systems, including GSST's SIR System models.

There may be times when a single return signal exhibits “glitches” due to noise or other forms of interference. It is often desirable to reduce these random variations of the return signal. This can be done by *scan stacking* [Conyers and Goodman, 1997]. Any random noise present from scan-to-scan can be reduced by simply averaging a successive number of scans to form one scan. However, the antenna must be moved at a slower rate to maintain the same horizontal resolution achieved before stacking.

Even if all parameters are set correctly, one problem still exists: the antenna must be pulled at a constant velocity if a uniform horizontal resolution between scans is desired (equal spacing between scans). Although not always necessary and in some cases impossible, keeping a uniform horizontal resolution can make data analysis easier. GSSI has designed a device, called a survey wheel, to overcome this problem. Instead of specifying the number of scans per second desired, the number of scans per *unit distance* is specified. The survey wheel is calibrated by pulling it along a survey line of known distance. The number of revolutions per unit distance is calculated, and from this the number of scans per revolution is found. If the survey wheel rotates twice per meter and 50 scans per meter is desired, the survey wheel will instruct the radar system to record a scan every 1/25th of a revolution. In this way, the velocity can be pulled at a greatly varying speed and uniform horizontal resolution will be maintained.

The SIR-10B system manufactured by GSSI is capable of recording data from two antennas simultaneously. In this case, transmit and receive functions are time-multiplexed between each antenna. This effectively reduces the PRF, and hence the scans per second, of each antenna. For example, if a PRF of 50 kHz is specified for the system, the effective PRF for each antenna is 25 kHz. The effective number scans per second is also halved.

3.3.3 Other GPR System Parameters

Many GPR systems also require that additional parameters be specified before data collection commences [Conyers and Goodman, 1997]. The GSSI SIR-10B system requires that

the signal position, range gains, and appropriate filters be set prior to data collection.

The *signal position* is the position of the return signal within the specified time window. A general rule-of-thumb is to place the first reflected pulse at the beginning of the window [GSSI, 1996]. The GSSI SIR-10B system will automatically attempt to position the first zero crossing at the beginning of the time window. The user can then manually adjust the position to his or her liking.

Equations (3.2) and (3.3) imply that the ratio of reflected energy to total energy is less for targets located in layers of greater depth. Attenuation and dispersion of the signal can further reduce this ratio. Many GPR systems attempt to compensate for this by applying *range gains* to the data in order to amplify the weaker reflections from deeper features. The GSSI SIR-10B allows the time window to be divided into ranges, with linear gain applied within each range. Once set, these gains should not be changed until the entire survey is completed.

Filters can be used during data collection to rid the data of system noise, environmental noise, and other unwanted signals. However, setting these filters can also slow down the system, and various parameters, such as the PRF, may need to be readjusted [Conyers and Goodman, 1997]. If post-processing software is available, it is generally better to record the data in its raw form and apply filters during post-processing rather than in the field. There may be certain circumstances when setting filters in the field is unavoidable.

Chapter 4

Computer Simulations

In this chapter, the theory discussed in Chapter 3 is used to synthesize theoretical return waveforms from four bridge decks of various composition. A one-dimensional representation of a single radar scan is simulated first, followed by a two-dimensional simulation. The 2-D simulation takes into account the return from every angle within the first Fresnel zone and the motion of the antenna along the ground to form a picture of sequential radar scans which compose an entire survey line. This 2-D representation is the electrical engineering equivalent of the *wiggle plot* used in seismic studies. The intent of the simulations is to provide a rough idea of what should be expected from actual experimental data.

4.1 Transmitted Waveform

The composition of the return signal directly depends on the transmitted pulse, which can take many forms, depending on the type of antenna used. The 400 MHz and 900 MHz antennas manufactured by GSSI are dipole antennas.

Many commercially available GPR systems use a squared, half-wave sinusoid or Gaussian current pulse (Figure 4.1) to excite a dipole antenna [Arcone, 1995]. The dipole response is approximately the *negative* differentiation of the pulse, as shown in Figure 4.2. The negative and positive half-cycles are formed by the excitation pulse's large acceleration and deceleration of current, respectively. An in-depth analysis of the dipole response is given in Arcone [1995].

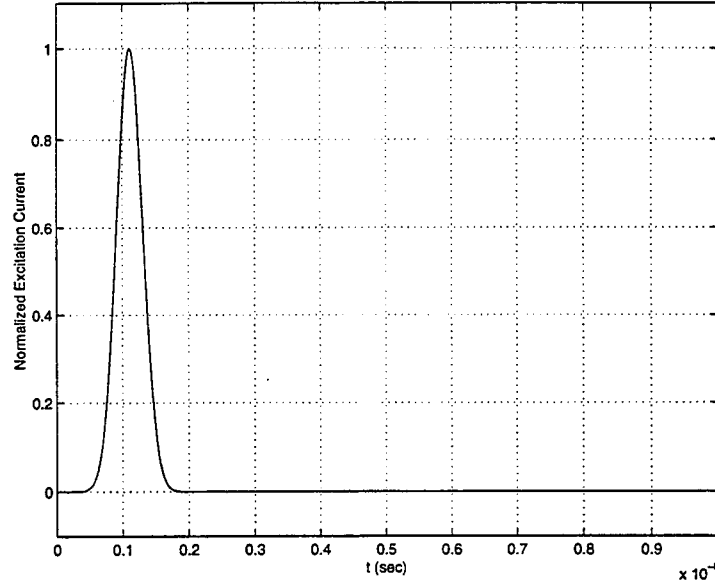


Figure 4.1: Gaussian current pulse used to excite a 900 MHz GPR dipole antenna.

A Gaussian excitation current pulse can be expressed mathematically as

$$g(t) = ae^{-\frac{(t-\tau)^2}{t_o^2}} \quad (4.1)$$

The variable a is an amplitude scaling factor, t_o is the time between the two points that are a $1/e$ factor down from the peak, and τ is a time-shift factor ($\tau = kt_o$ where k is any number). The transmit pulse is then found by taking the negative derivative of $g(t)$:

$$s(t) = -g'(t) = 2a \left(\frac{t-\tau}{t_o^2} \right) e^{-\frac{(t-\tau)^2}{t_o^2}} \quad (4.2)$$

The two normalized waveforms, $g(t)$ and $s(t)$, are shown in Figures 4.1 and 4.2, respectively. Values are given for a 900 MHz transmit pulse.

The following four bridge deck cases will be considered (Figure 4.3):

1. Without asphalt overlay and without rebar corrosion.
2. Without asphalt overlay and with rebar corrosion.

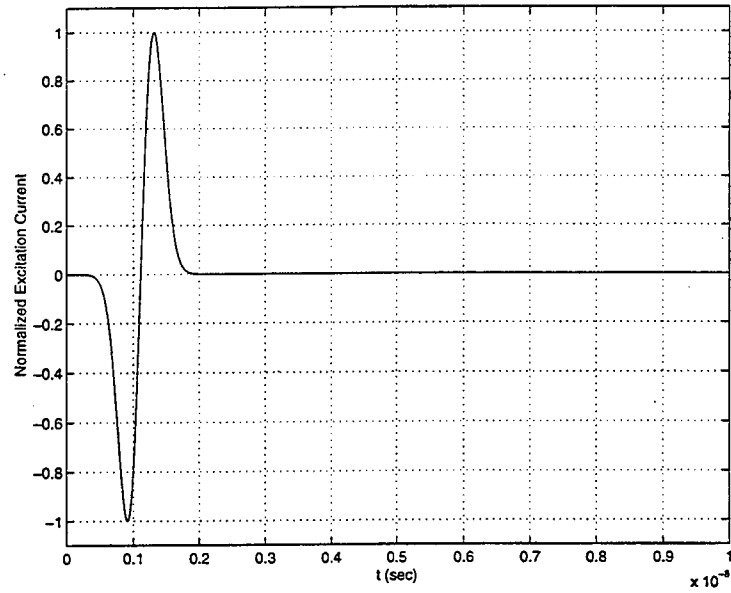


Figure 4.2: Theoretical response of a 900 MHz antenna to the Gaussian current excitation shown in the previous figure.

3. With asphalt overlay and without rebar corrosion.
4. With asphalt overlay and with rebar corrosion.

Note that both good and corroded rebar can occur within the same bridge deck, i.e. cases 1 and 2 or cases 3 and 4 can occur simultaneously. It should be also noted that cases 3 and 4 are considered although the number of bridge decks with an asphalt overlay is very small [Hall, 1997].

The following parameters are assumed:

1. For all cases, the signal incident upon the bridge deck is of the form given in Equation (4.2).
2. For all cases, the height of the antenna above the ground is 5.0 cm.
3. For all cases, ϵ_r for concrete is considered to be 7.
4. Reflection coefficients are calculated using Equation (3.2). The reflection coefficient is assumed to be -1.0 for a good rebar and -0.35 for a corroded rebar. The value of

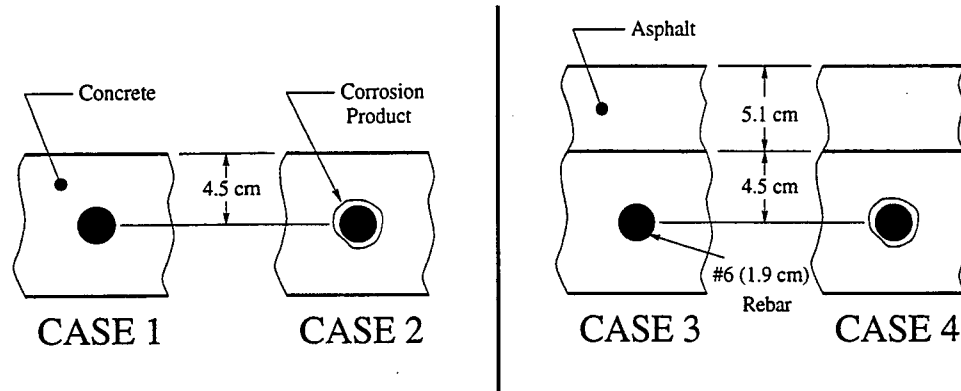


Figure 4.3: Illustration of the four bridge deck cases considered for simulation.

-0.35 for the corroded rebar was used since this value ensured a good match between the variance ratio obtained from simulations and controlled laboratory measurements on a model bridge deck (See Chapter 7).

5. Two-way travel times are calculated using Equation (3.6).
6. For cases 1 and 2, the amount of concrete cover over the rebars is 4.5 cm.
7. For cases 3 and 4, the asphalt overlay is 5.1 cm thick and has an ϵ_r value of 5. The amount of concrete cover over the rebars is 4.5 cm.

The amount of concrete cover over the rebars varies from 4.5 cm to 5.1 cm, and the thickness of asphalt covering the concrete (when present) ranges from 5.1 cm to 10.2 cm [Hall, 1997]. Also, ϵ_r generally falls in the range from 6 to 7 for concrete and 3 to 5 for asphalt [Conyers and Goodman, 1997]. Since the possibility of pulse-overlap increases with decreasing layer thickness, worst-case scenarios are simulated by making the layers as thin as possible. Other parameters were chosen arbitrarily from given ranges.

4.2 Theoretical 1-D Return Waveform Analysis

As stated at the beginning of the chapter, a bridge deck can be considered a multi-layer structure. The return waveform can then be found by solving the multiple region, boundary-

value problem. Each return waveform is known as a *trace* or *A-scan* [Daniels, 1996]. Matlab 5.1 is used for all one-dimensional simulations.

4.2.1 Theoretical Radar Signature: Cases 1 and 2

Cases 1 and 2 involve bridge decks which do not have an asphalt overlay. The time-domain equation representing the reflected signal voltage from the bridge deck is given by

$$r(t) = \Gamma_{air,con} s(t - t_{r,air}) + \Gamma_r (1 - \Gamma_{air,con}^2) s(t - t_{r,air} - t_{r,con}) \quad (4.3)$$

where

$s(t)$ = incident signal voltage

$\Gamma_{air,con}$ = reflection coefficient from air to concrete

Γ_r = reflection coefficient due to a rebar (either good or corroded)

$t_{r,air}$ = two-way travel time in air

$t_{r,con}$ = two-way travel time in concrete

The reflected waveforms resulting from 400 MHz and 900 MHz incident pulses are shown in Figures 4.4 and 4.5 for good and corroded rebars, respectively. The same information for a 400 MHz incident pulse is shown in Figures 4.6 and 4.7. It is seen that corrosion reduces the amount of reflection from the rebar. The effects of frequency loading, which are more realistic cases, are represented as dashed lines.

Although difficult to see in Figures 4.4 and 4.5, the reflection from the rebar overlaps the reflection from the concrete surface. This implies that a shorter pulse is needed if no overlap is to occur (a greater space between the rebar and the surface would also prevent pulse overlap, but is impractical). The overlap is very noticeable in Figures 4.6 and 4.7 for the 400 MHz case. The problem is further compounded if frequency loading is taken into account. These are the only two antennas available for this research project. Therefore, special data analysis techniques will have to be used to extract any useful data.

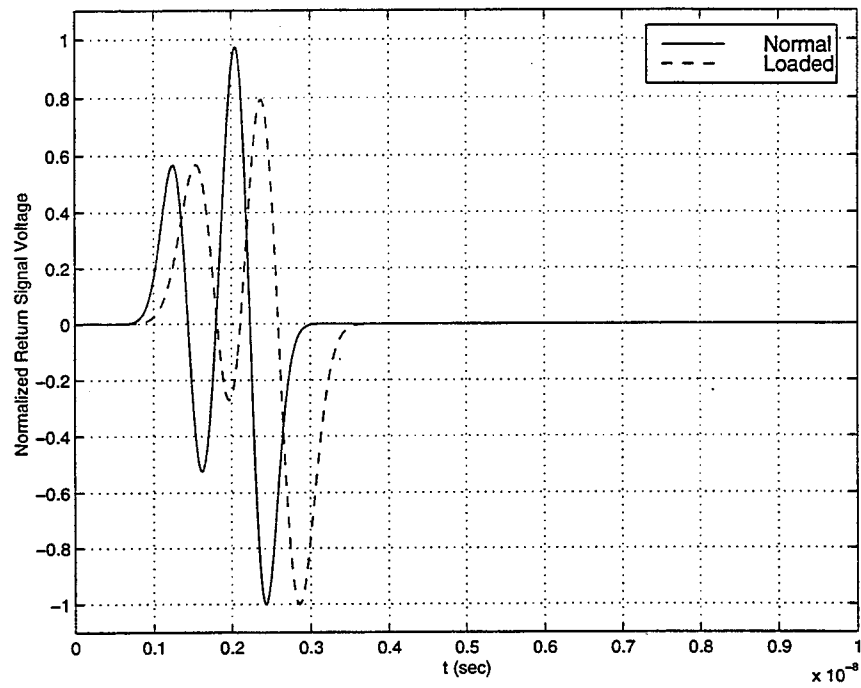


Figure 4.4: Return waveforms from a Case 1 bridge deck. The incident signal is a 900 MHz pulse.

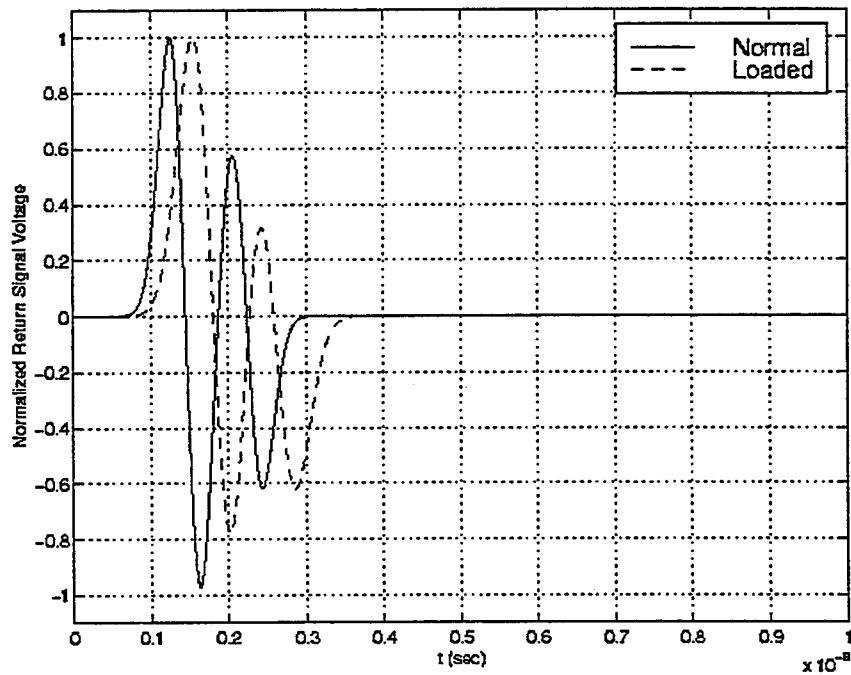


Figure 4.5: Return waveform from a Case 2 bridge deck. The incident signal is a 900 MHz pulse.

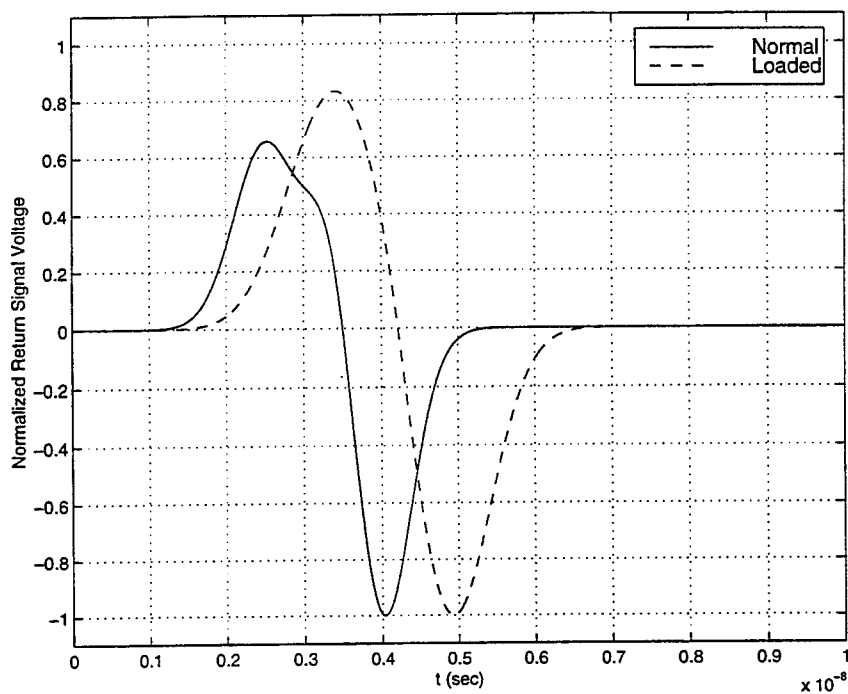


Figure 4.6: Return waveform from a Case 1 bridge deck. The incident signal is a 400 MHz pulse.

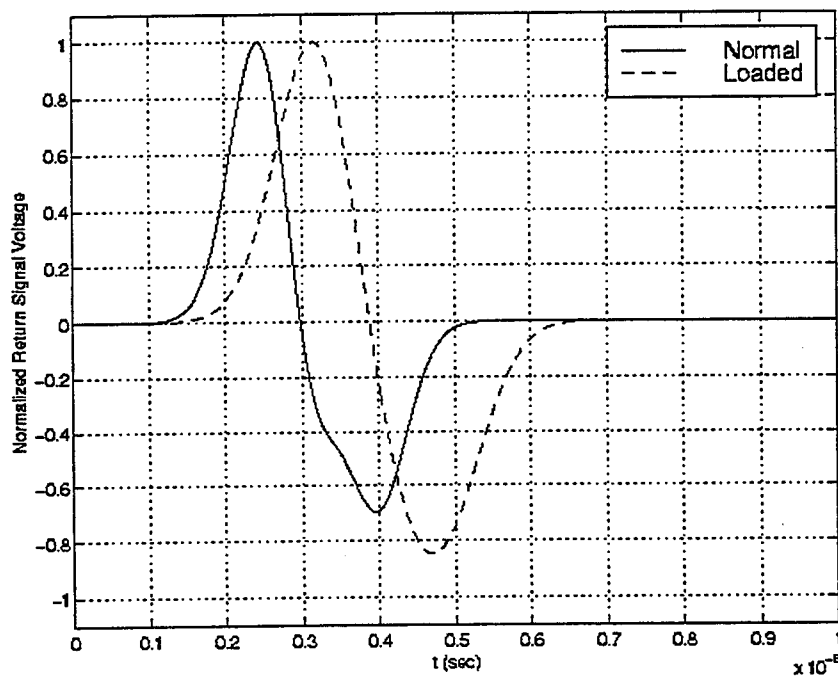


Figure 4.7: Return waveform from a Case 2 bridge deck. The incident signal is a 400 MHz pulse.

4.2.2 Theoretical Radar Signature: Cases 3 and 4

A bridge deck with a 5.1 cm asphalt overlay is now examined (refer to Figure 4.3). The analysis is similar to Cases 1 and 2 except an additional layer (asphalt) is added. The time-domain equation representing the reflected signal voltage from an asphalt-covered bridge deck is given by

$$r(t) = \Gamma_{air,asp} s(t - t_{r,air}) + \Gamma_{asp,con} (1 - \Gamma_{air,asp}^2) s(t - t_{r,air} - t_{r,asp}) + \Gamma_r (1 - \Gamma_{air,asp}^2) (1 - \Gamma_{air,asp}^2) s(t - t_{r,air} - t_{r,asp} - t_{r,con}) \quad (4.4)$$

where

$\Gamma_{air,asp}$ = reflection coefficient from air to asphalt

$t_{r,asp}$ = two-way travel time in asphalt

The reflected waveforms resulting from a 900 MHz incident pulse are shown in Figures 4.8 and 4.9 for good and corroded rebars, respectively. Reflected waveforms for a 400 MHz incident pulse are shown in Figures 4.10 and 4.11. Again it is seen that corrosion reduces the amount of reflection from the rebar. As before, the effects of frequency loading are represented as dashed lines.

For Cases 3 and 4 another reflection, known as a *second-time-around* reflection, can interfere with the three primary reflections [Carter et al., 1986]. As seen in Figure 4.12, the second-time-around reflection occurring in the asphalt layer can interfere with the reflection from a rebar. This is the only second-time-around reflection occurring within the time interval of interest.

The severity of interference can be quantified by the ratio of the second-time-around reflection to the rebar reflection, which is [Carter et al., 1986]

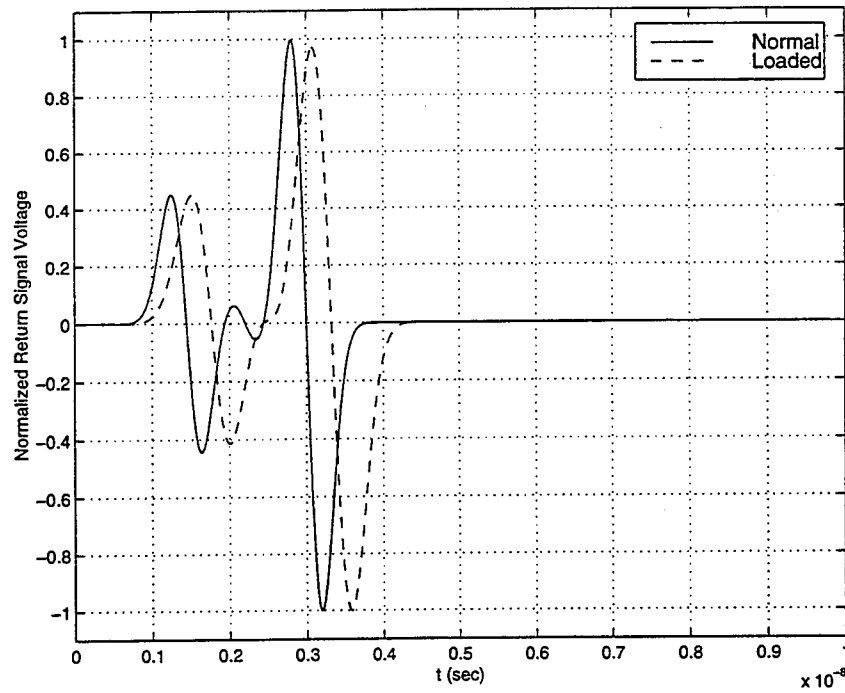


Figure 4.8: Return waveform from a Case 3 bridge deck. The incident signal is a 900 MHz pulse.

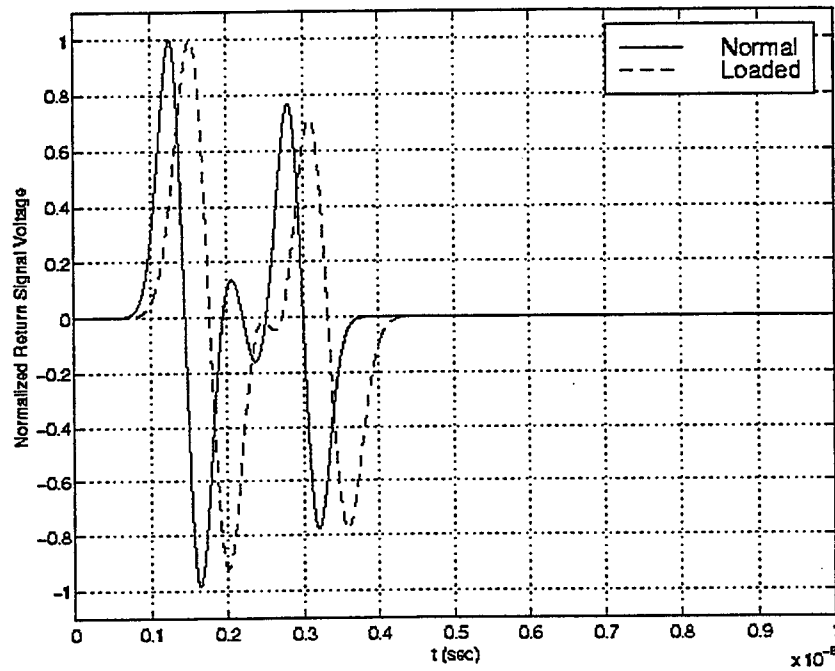


Figure 4.9: Return waveform from a Case 4 bridge deck. The incident signal is a 900 MHz pulse.

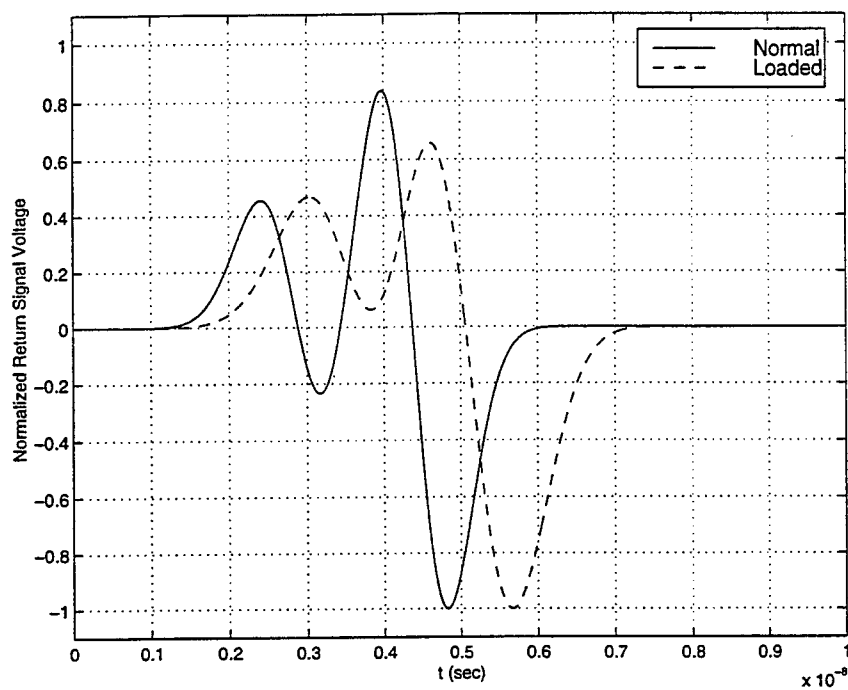


Figure 4.10: Return waveform from a Case 3 bridge deck. The incident signal is a 400 MHz pulse.

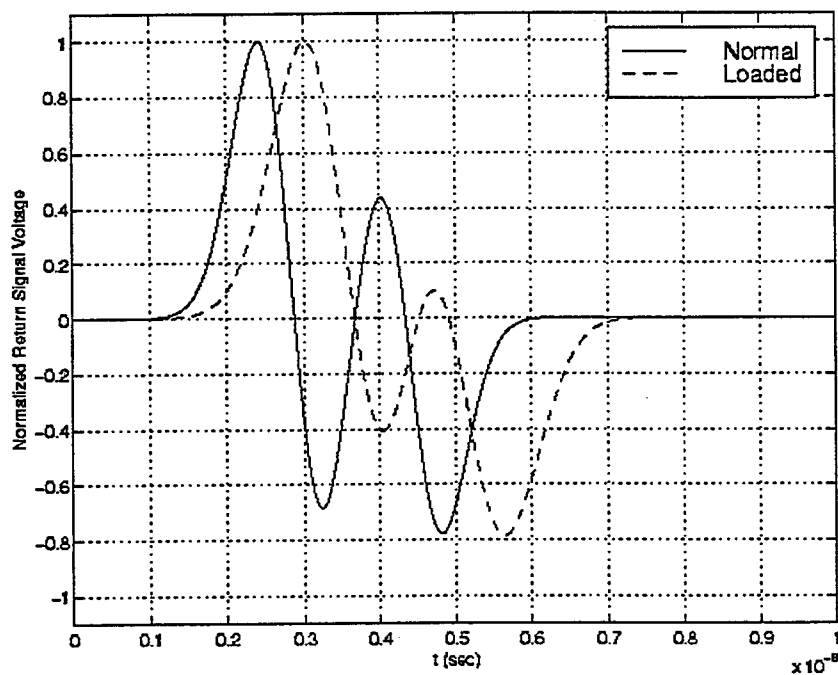


Figure 4.11: Return waveform from a Case 4 bridge deck. The incident signal is a 400 MHz pulse.

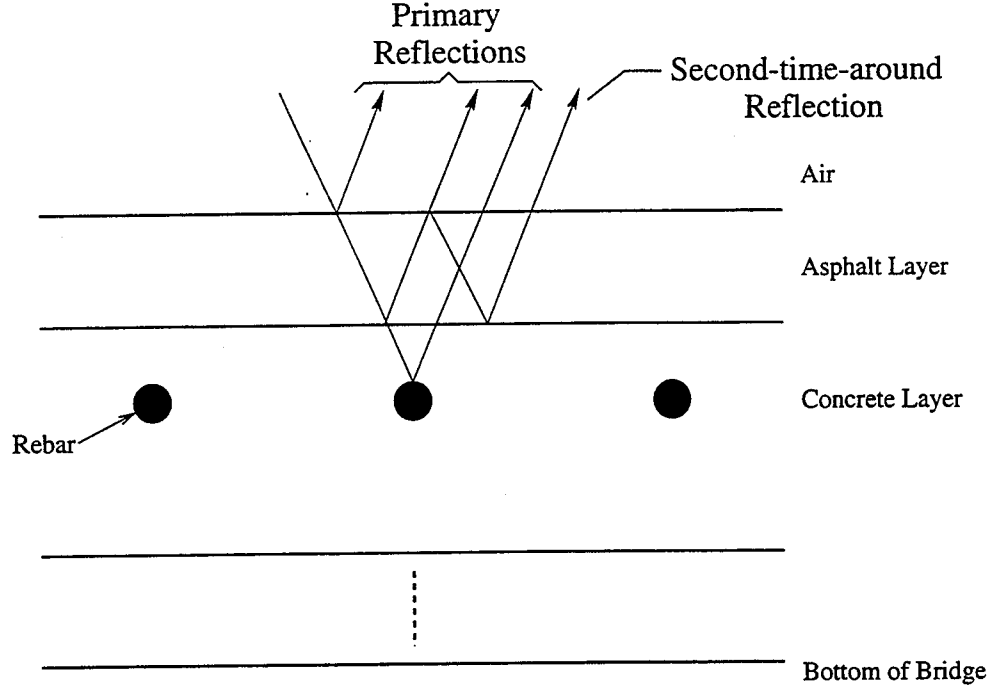


Figure 4.12: Three primary reflections from a bridge deck with an asphalt overlay (Cases 3 and 4). A second-time-around reflection within the asphalt layer can interfere with the reflection from a rebar [Carter et al., 1986].

$$I = \left| \frac{-\Gamma_{air,asp}\Gamma_{asp,con} (1 - \Gamma_{air,asp}^2)}{\Gamma_r (1 - \Gamma_{asp,con}^2) (1 - \Gamma_{air,asp}^2)} \right| \quad (4.5)$$

Keeping with the assumptions that ϵ_r values are 5 and 7 for dry asphalt and concrete, respectively, $I = 0.27\%$ for good rebar ($\Gamma_r = -1.0$) and $I = 0.90\%$ for corroded rebar ($\Gamma_r = -0.3$). Therefore, the contribution of the second-time-around reflection is negligible and can be ignored.

4.3 Theoretical 2-D Return Waveform Analysis

The one-dimensional simulations provide the foundation for the two-dimensional simulations. The movement of the antenna along the ground, the front-to-back radiation pattern of the antenna, and the use of actual radar parameters make the two-dimensional simulation more complicated. A model bridge deck is assumed to contain six equally-spaced rebars,

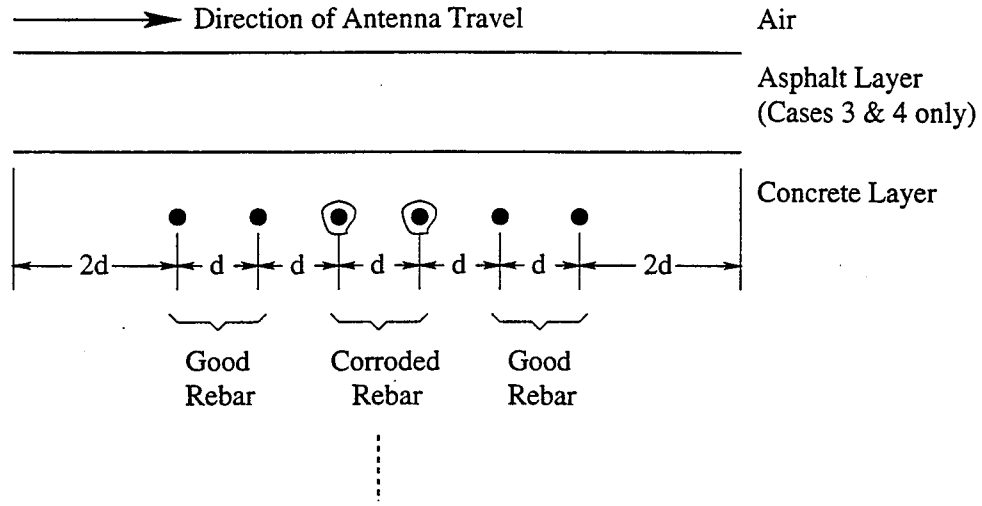


Figure 4.13: Layout of the model bridge deck considered for the two-dimensional simulations.

four good and two corroded, as shown in Figure 4.13. A composite trace is recorded by the radar system at certain distance intervals determined by the choice of radar parameters. All traces (A-scans) are then compiled into a two-dimensional picture known in the seismic field as a *wiggle plot* or *B-scan* [Daniels, 1996]. Each trace is plotted vertically (time-depth) corresponding to the position along the ground where the trace was recorded.

A C program was written to perform the two-dimensional simulation. The following radar parameters were assumed: 256 samples per scan, 50 scans per second, and a PRF of 52 kHz. A constant antenna speed of 0.5 m/s is also assumed, as well as rebar spacing of 20.3 cm. All parameters can be adjusted in the program. A simple $\cos^2\theta$ ($-\pi/4 \leq \theta \leq \pi/4$) radiation pattern was chosen for the antenna. All other parameters assumed for the one-dimensional simulations, such as concrete thickness, ϵ_r values, etc., apply to the two-dimensional simulations as well.

Cases 1 and 2 are considered simultaneously, as are cases 3 and 4, since both good and corroded rebar can be seen in a single B-scan.

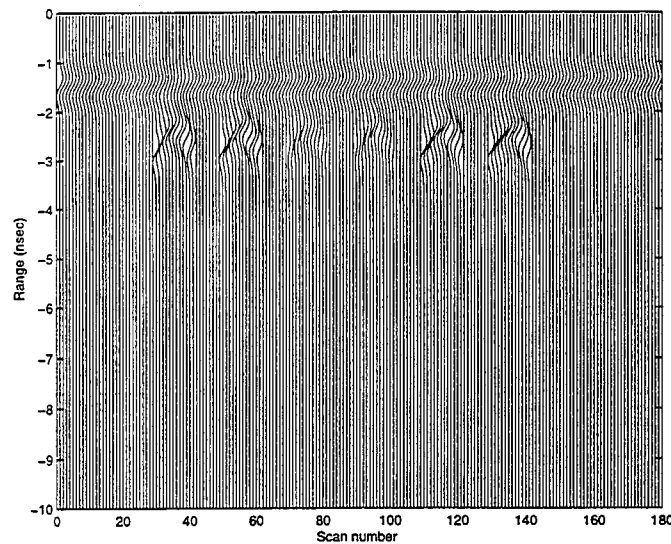


Figure 4.14: Theoretical B-scan for a Case 1-2 bridge deck. The incident signal is a 900 MHz pulse.

4.3.1 Theoretical B-Scan: Cases 1 and 2

The B-scan resulting from the assumed parameters and a center frequency of 900 MHz is illustrated in Figure 4.14. The 400 MHz B-scan is shown in Figure 4.16. As anticipated from the discussion in Chapter 3, the rebars form hyperbolas due to the radiation pattern and movement of the antenna. The two corroded rebars in the center are easily distinguished by their faint reflections. The effects of frequency loading are represented by the B-scans in Figures 4.15 and 4.17 for 900 MHz and 400 MHz, respectively. Note the fairly extreme pulse overlap in both 400 MHz B-scans.

4.3.2 Theoretical B-Scan: Cases 3 and 4

Adding an asphalt overlay results in the B-scans shown in Figures 4.18 (900 MHz) and 4.20 (400 MHz). Since the rebars are located further from the antenna due to the asphalt overlay, the hyperbolas formed by the rebars will overlap. The effects of frequency loading are represented by the B-scans in Figures 4.19 and 4.21 for 900 MHz and 400 MHz, respectively.

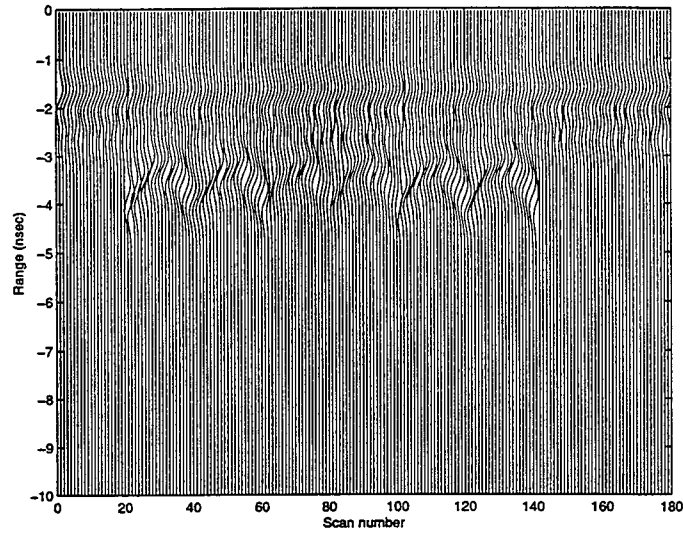


Figure 4.15: Theoretical B-scan for a Case 1-2 bridge deck with frequency loading considered. The incident signal is a 900 MHz pulse loaded down to 680 MHz.

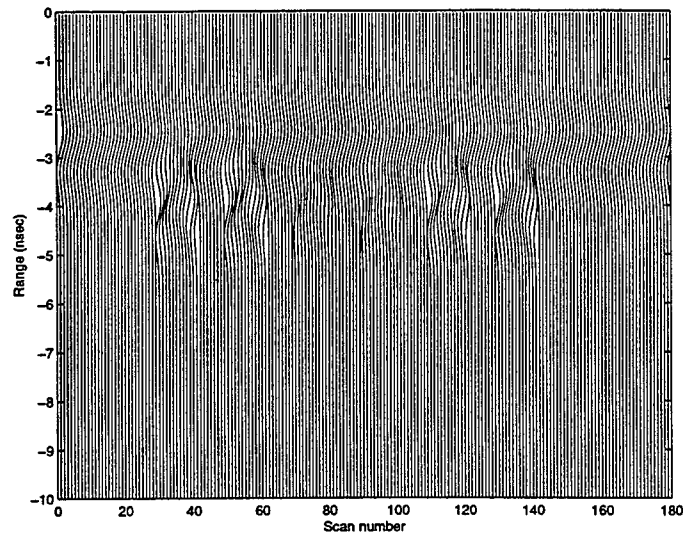


Figure 4.16: Theoretical B-scan for a Case 1-2 bridge deck. The incident signal is a 400 MHz pulse.

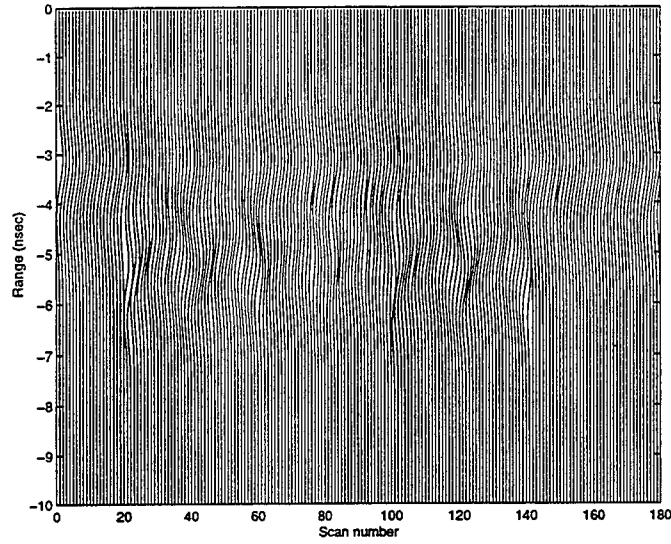


Figure 4.17: Theoretical B-scan for a Case 1-2 bridge deck with frequency loading considered. The incident signal is a 400 MHz pulse loaded down to 302 MHz.

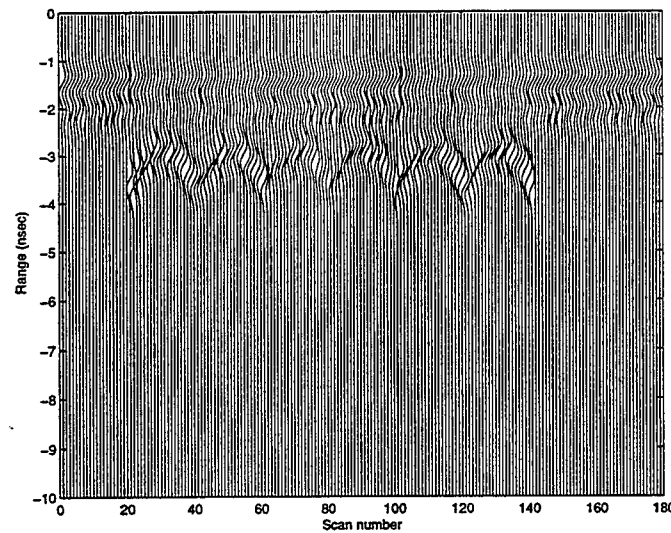


Figure 4.18: Theoretical B-scan for a Case 3-4 bridge deck. The incident signal is a 900 MHz pulse.

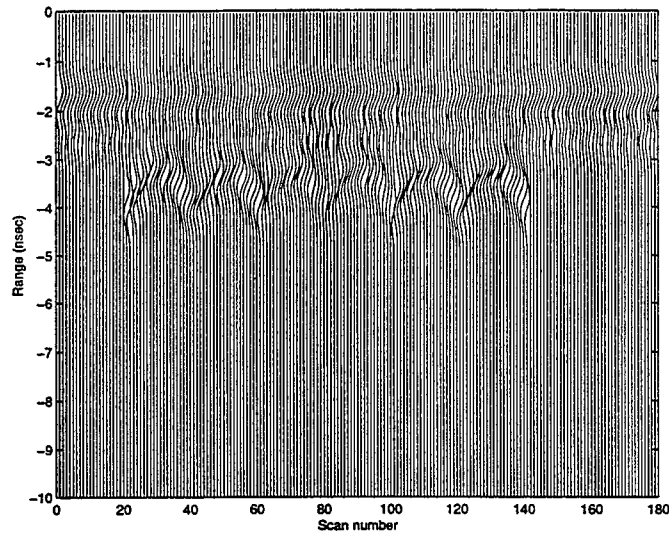


Figure 4.19: Theoretical B-scan for a Case 3-4 bridge deck with frequency loading considered. The incident signal is a 900 MHz pulse loaded down to 697 MHz.

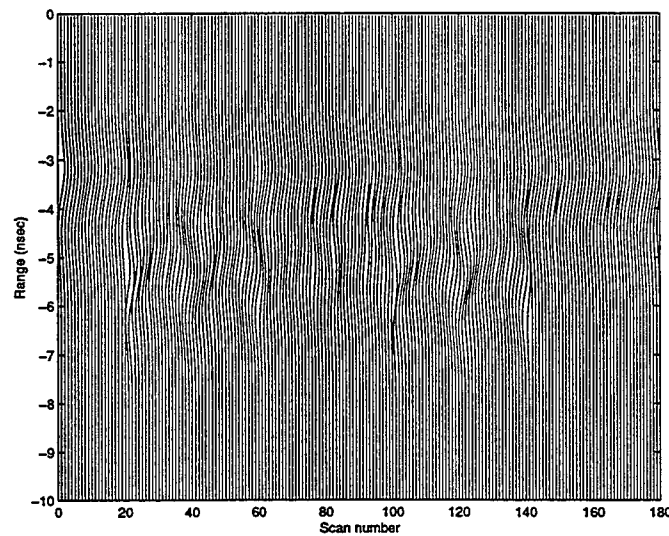


Figure 4.20: Theoretical B-scan for a Case 3-4 bridge deck. The incident signal is a 400 MHz pulse.

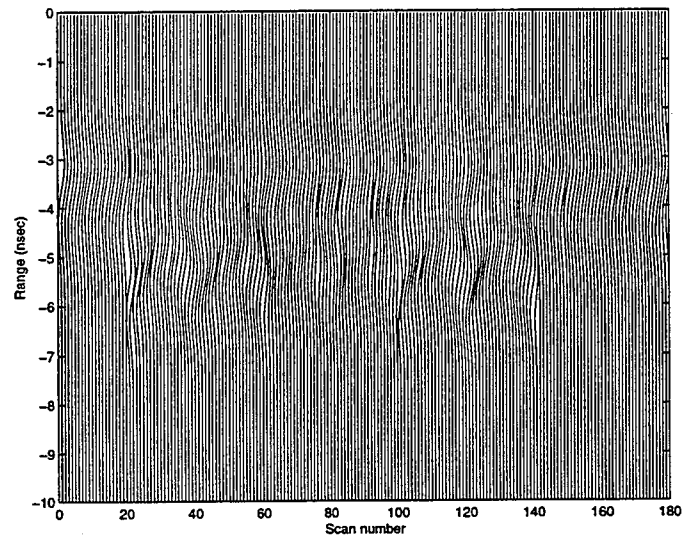


Figure 4.21: Theoretical B-scan for a Case 3-4 bridge deck with frequency loading considered. The incident signal is a 400 MHz pulse loaded down to 310 MHz.

Chapter 5

Equipment Description

The SIR System-10B Ground-Penetrating Radar System, manufactured by Geophysical Survey Systems, Inc. of North Salem, NH, was the radar system used for collecting bridge deck data. A simple block diagram of the system is shown in Figure 5.1. The SIR-10B is a pulsed radar system. Two monostatic antennas, which transmit and receive pulses at frequencies of 400 MHz and 900 MHz, were used simultaneously to collect data. An A/D converter and Motorola DSP-56001 Radar Processor convert the received data into data scans, which are then ran through an image processing algorithm for real-time output on a monitor or plotter. The data can be further manipulated using a post-processing software package called *RADAN*, also a product of GSSI.

All components of the radar system are housed in portable, rugged cases for use in the field. The following chapter discusses the complete system in more detail, including the mainframe and display units, thermal plotter, antennas, data collection software, and post-processing software.

5.1 SIR System-10B

The SIR System-10B (SIR-10B) is a digital, multi-channel Subsurface Interface Radar (SIR) system that is used to record, process, and display profiles of subsurface features in four formats: color linescan, grayscale linescan, wiggle trace, and oscilloscope trace [GSSI, 1996].

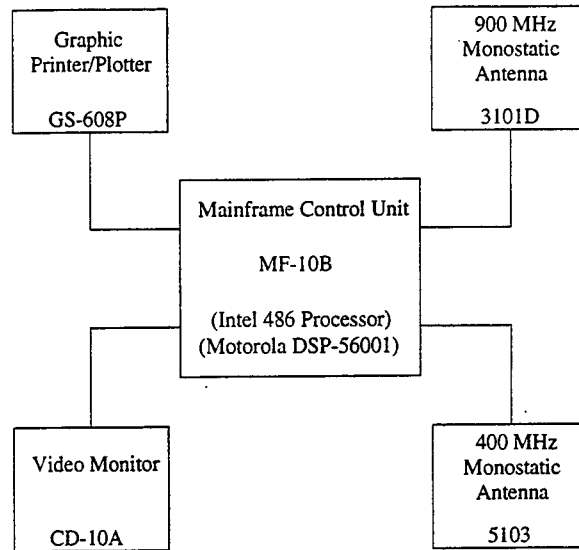


Figure 5.1: Simple block diagram of the SIR-10B radar system.

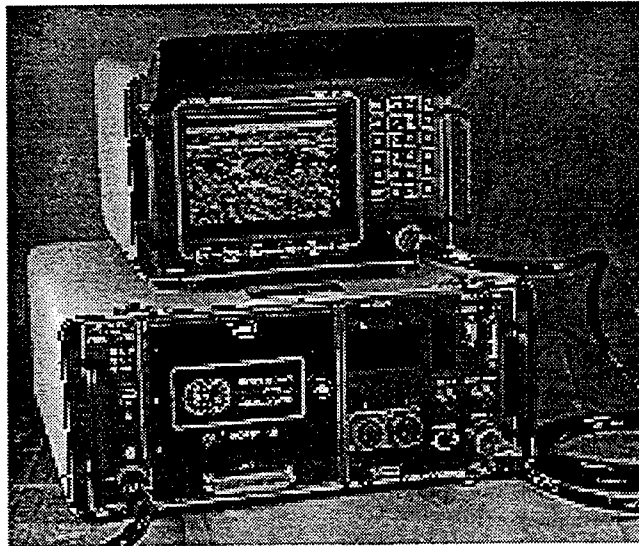


Figure 5.2: The SIR-10B ground-penetrating radar system (courtesy GSSI).

The system is designed to be fairly user-friendly, and consists of two units, the Model MF-10B Mainframe and the Model CD-10B control/display unit. The system components are shown in Figure 5.2.

5.1.1 MF-10B Mainframe Unit

The mainframe unit, illustrated in Figure 5.3, allows for two antenna interface modules, data collection, signal processing hardware and software, data storage, and connectors for connection to external devices such as the monitor, plotter, power source, etc. The heart of the system is a 486 SLC CPU with a math co-processor. A Motorola DSP-56001 Radar Processor performs the bulk of the signal processing. Specifications for the MF-10B are given in Table 5.1 [GSSI, 1996].

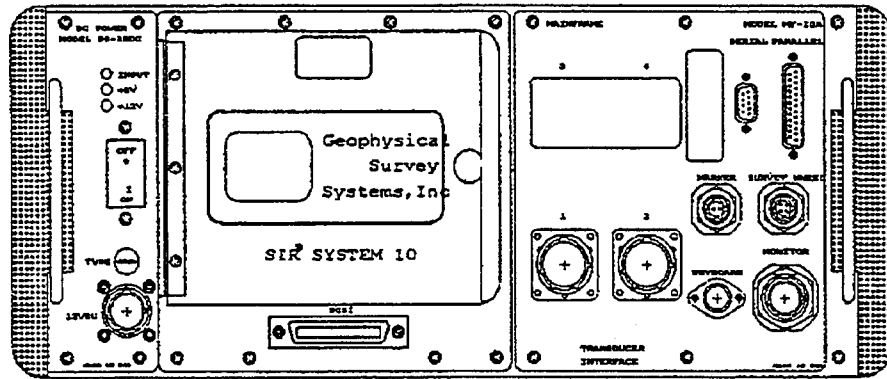


Figure 5.3: Sketch of the MF-10B mainframe unit [GSSI, 1996].

Table 5.1: MF-10B Mainframe Specifications [GSSI, 1996]

Size	44.1 cm x 38.1 cm x 17.8 cm
Weight	18.0 kg
Operating Temperature	-10° C to 40° C external
Relative Humidity	less than 90%, non-condensing
Input Power	12 VDC nominal, 200 W
Computer Board	486SLC processor with math co-processor
Radar Processor	Motorola DSP-56001, 20 MHz
RAM Memory	16 MB
Hard Drive	1.3 GB
Floppy Drive	8.9 cm (3.5 in), 1.44 MB

The power supply module, which consists of the power connector, power switch, power indicator LEDs, and 25 amp DC fuse, is located on the far left panel of the mainframe unit.

Although an AC module is available, the unit is equipped with a 12-volt DC module designed to operate with a standard 12-volt automobile battery. This is practical for operation in the field. When using two antennas, the system draws approximately 7 to 11 amps. The maximum power consumption is 280 watts, which occurs during startup.

The data storage unit comprises the central portion of the mainframe unit. It consists of a 3.5-inch (1.44 MB) floppy disk drive, 1.3 GB hard disk drive, and a SCSI connector which can be used to connect an external SCSI hard drive or tape drive.

The right portion of the mainframe unit consists of the connector panel. Two transducer interface connectors are provided for use with either one or two antennas. Serial and parallel port connectors are located on the panel to allow for data transfer between the unit and a PC. When collecting data, it is often desirable to place fiduciary marks on the data profile to gauge horizontal distance. This can be done with a marker button or survey wheel. For convenience, connectors for each device are made available on both the connector panel and the antennas. Connections for interfacing with the CD-10A display unit and a keyboard are also provided.

5.1.2 CD-10A Control/Display Unit

Figure 5.4 shows the CD-10A, a combination video monitor and keypad that provides an interface with the mainframe unit. The monitor is a VGA-compatible 19 cm video display. The keypad consists of twenty-four keys which enable the user to interface with a menu-driven data collection program residing on the MF-10B mainframe hard drive. In addition, six function keys are located beneath the video screen. Using the keypad can often be slow and awkward. Therefore, a connector has been provided on the mainframe unit for attaching an external PC-style 101-key keyboard. The connector interfaces the monitor to the mainframe unit via 19-pin video cable. Table 5.2 gives the specifications for the CD-10A [GSSI, 1996].

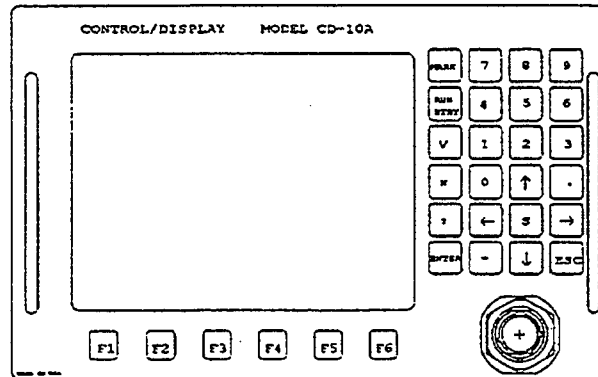


Figure 5.4: Sketch of the CD-10A control/display unit [GSSI, 1996].

Table 5.2: CD-10A Control/Display Specifications [GSSI, 1996]

Size	30.5 cm x 29.2 cm x 21.6 cm
Weight	10.5 kg
Operating Temperature	-10° C to 40° C external
Relative Humidity	less than 90%, non-condensing
Input Power	12 VDC nominal, 200 W
Monitor	19 cm color VGA, 640 x 480 pixels, 32 kHz non-interlaced
Keypad	24 keys, 6 function keys

5.2 GS-608P Thermal Plotter/Printer

The GS-608P Thermal Plotter/Printer (Figure 5.5) is designed for use in the field. It can operate in both plotter (raster) mode and printer (character) mode. Information is placed on thermal-sensitive paper which moves beneath a fixed thermal printhead, and is displayed in a gray scale consisting of sixteen switchable levels. Plots or printouts can be done in real-time as data is being taken or done at a later time. The GS-608P is useful when on-sight hardcopies are desirable. One drawback, however, is a decrease in the data acquisition rate when plotting during real-time collection. Specifications for the GS-608P are given in Table 5.3 [GSSI, 1996].

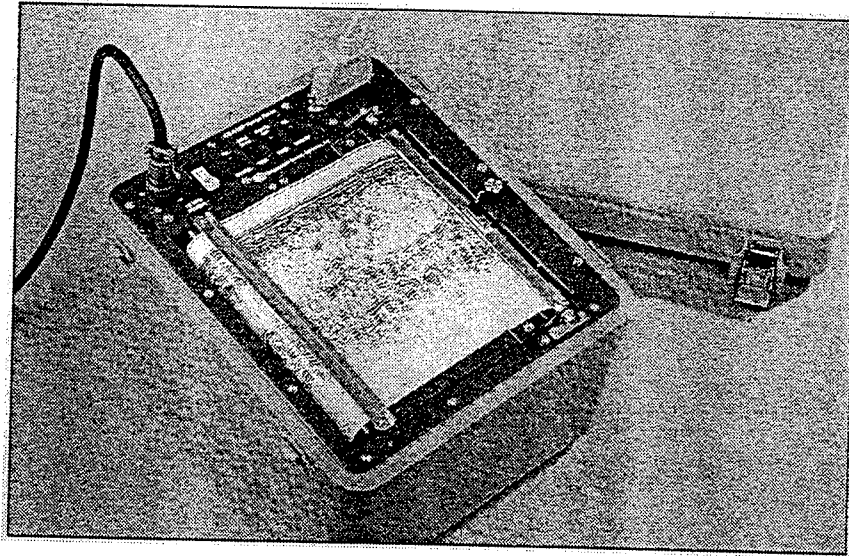


Figure 5.5: Picture of the GS-608P thermal plotter/printer (courtesy GSSI).

Table 5.3: GS-608P Printer/Plotter Specifications [GSSI, 1996]

Size	36.6 cm x 30.5 cm x 19.0 cm
Weight	11.5 kg
Operating Temperature	0° C to 50° C external
Relative Humidity	5% to 95%, non-condensing
Input Power	12 VDC nominal; 35 W idle, 150 W printing
Media Type	Direct Thermal roll paper, 21.6 cm (8.5 in) width
Thermal Printhead	Linear array
Dots Per Scan	1680
Resolution	203 dpi
Plot Rate	0.635 cm/sec max
Print Rate	4.17 character lines/sec

5.3 Antennas

Two monostatic, dipole antennas were used simultaneously to acquire the bridge deck data: the GSSI Model 5103, which has a center frequency of 400 MHz, and the GSSI Model 3101D, with a 900 MHz center frequency. Since the 900 MHz antenna has an approximate depth range of only 75 cm in concrete, it was used to provide a high-resolution profile of the bridge deck's upper layer. The 400 MHz antenna, which has an approximate depth range

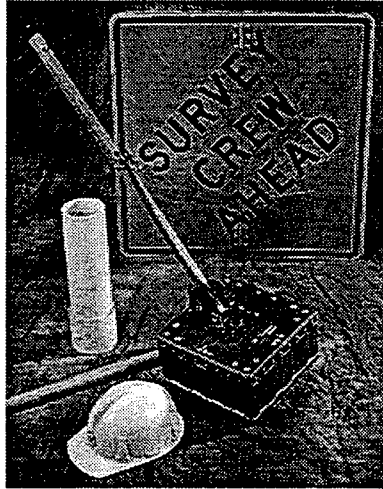


Figure 5.6: Picture of the Model 5103 400 MHz antenna (courtesy GSSI).

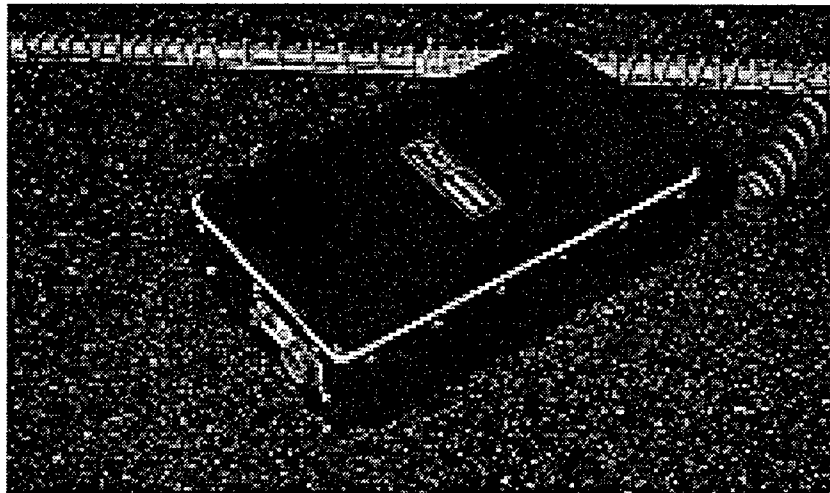


Figure 5.7: Picture of the Model 3101D 900 MHz antenna (courtesy GSSI).

of 4.5 m in concrete, collected data at greater depths where resolution was not critical. The antennas are made from 3.8 cm diameter, nickel-plated, powder-coated, aluminum tubes.

The antennas are designed to be towed on the ground along the line to be surveyed. This is done to provide for better coupling of the transmitted signals into the ground. The antennas are encased in rugged, plastic casings to withstand the wear and tear that occurs in the field when being dragged along the ground. They are also shielded to reduce interference from other signal sources such as power lines. Figure 5.6 shows the 400 MHz antenna; the 900 MHz antenna is depicted in Figure 5.7. The antennas are connected to

Table 5.4: 400 MHz Antenna Specifications [Delea, 1996]

GSSI Model Number	5103
Center Frequency	400 MHz
Approximate Pulse Duration	2.5 ns
Beam Width	90° front-to-back, 60° side-to-side
Antenna Configuration	Monostatic Dipole
Antenna Impedance	240 ohms
Pulse to Antenna	100 V
Radiation Efficiency	20%
Applied Peak Power	41.7 W
Applied Average Power (at 50 kHz PRF)	4.2 mW
Radiated Peak Power	8.3 W
Radiated Average Power (at 50 kHz PRF)	0.84 mW
Size	30 cm x 30 cm x 17 cm
Weight	5 kg

Table 5.5: 900 MHz Antenna Specifications [Delea, 1996]

GSSI Model Number	3101D
Center Frequency	900 MHz
Approximate Pulse Duration	1.1 ns
Beam Width	90° front-to-back, 60° side-to-side
Antenna Configuration	Monostatic Dipole
Antenna Impedance	240 ohms
Pulse to Antenna	50 V
Radiation Efficiency	20%
Applied Peak Power	10.4 W
Applied Average Power (at 50 kHz PRF)	0.57 mW
Radiated Peak Power	2.1 W
Radiated Average Power (at 50 kHz PRF)	0.11 mW
Size	8 cm x 18 cm x 33 cm
Weight	2.3 kg

the mainframe unit using 11-pin transducer cables. The cables are 30 m in length to allow for antenna operation a significant distance away from the mainframe unit. Tables 5.4 and 5.5 give GSSI's specifications for the 400 MHz and 900 MHz antennas, respectively [Delea, 1996].

As mentioned earlier, inputs for both a marker button and a survey wheel are located on each antenna. The marker button serves two functions: to start and stop data collection and to place fiduciary marks on the radar profile, providing a horizontal reference for the data. This is also known as "gridding" the data [Daniels, 1996]. The survey wheel simplifies the process of gridding a site by automatically placing fiduciary marks on the data profile. The use of the survey wheel also eliminates any error that may occur when antennas are pulled at an uneven rate by recording data at user-selectable distance increments. Using a survey wheel, however, limits the rate at which the antennas can be pulled.

5.4 Data Collection Software

Powered by a Motorola DSP-56001 radar processor operating at 20 MHz, the SIR System-10B utilizes a user-friendly, menu-driven program to rapidly collect and process the data in 8 or 16-bit format. The program provides flexibility in changing data-acquisition parameters such as gain, sampling, scanning, filtering, and transmit rate. It also allows for automatic or manual setting of some parameters, creating a wide variety of control suited to satisfy both novice and experienced users. The program allows for control of up to four antennas, although only two antenna interfaces are available on the SIR-10B system. In multi-antenna mode, each antenna is totally independent of all other antennas. Thus, antennas of different frequencies, gain levels, ranges, etc. can be used to simultaneously collect data. The menu tree shown in Figure 5.8 gives the structural layout of the menus [GSSI, 1996].

The program allows for the storage of data in RAM, on the hard drive, on floppy disk, or on tape using an external SCSI tape drive. Data can also be transferred to a PC via serial or parallel ports.

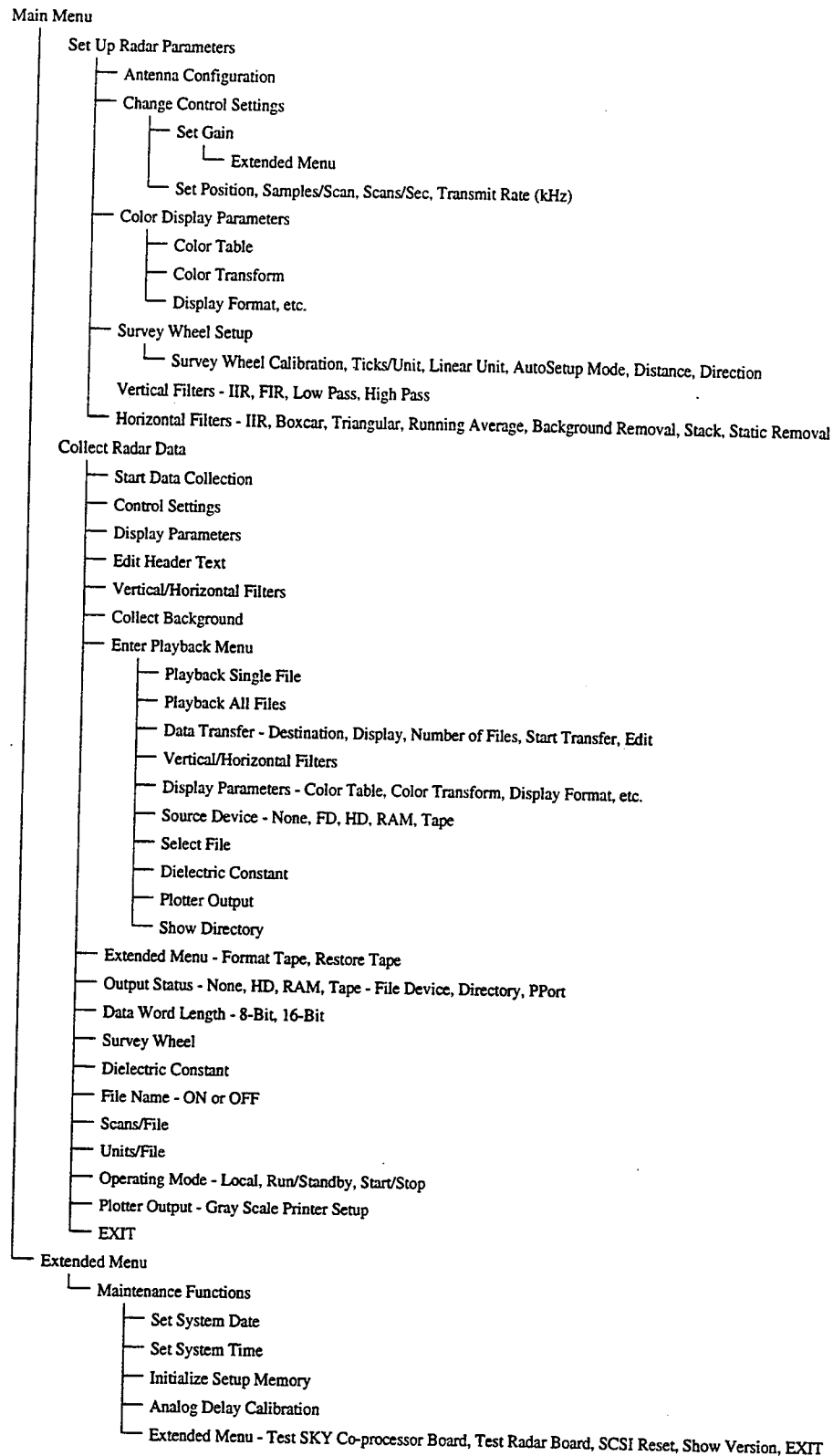


Figure 5.8: Menu structure of the data-collection software utilized by the SIR-10B radar system [GSSI, 1996].

5.5 *RADAN* Post-Processing Software

After data have been collected, the next step is analyzing the data. Often it is necessary to manipulate the data into a more usable form. GSSI's *RADAN* post-processing software was used to analyze the bridge data. The program runs in a Windows 95 environment, utilizing point-and-click menus and toolbars. The software is set up in an add-on modular format, allowing for software expansion in the event that advanced processing techniques are needed. The WINRAD-PPS and RADPRINT add-on modules were used for this project to automatically process multiple data sets simultaneously and to print the data on a standard printer. 3-D and velocity analysis modules are also available.

RADAN can display multiple data profiles in any of four formats: color linescan, grayscale linescan, wiggle plot, and oscilloscope trace. In linescan format (both color and grayscale), multiple transforms are available, including linear, logarithmic, exponential, and custom set-ups. The wiggle plot displays data in the traditional seismic layout. The oscilloscope trace format shows an actual oscilloscope trace of one scan of radar data. A color linescan image, wiggle plot, and oscilloscope trace are shown in Figures 5.9, 5.10, and 5.11, respectively.

Data can be processed using a number of various signal processing functions listed below.

- *Infinite Impulse Response (IIR) Filters*

Both vertical (frequency) and horizontal (spatial) high and low pass filters are available. Since IIR filters are not necessarily symmetrical, care must be taken when using them since slight phase shifts in the data can take place.

- *Finite Impulse Response (FIR) Filters*

As with the IIR filters, both vertical and horizontal filters are available. Unlike IIR filters, FIR filters will produce symmetrical results, so phase shifts will not occur. The user can also select between boxcar or triangular filters.

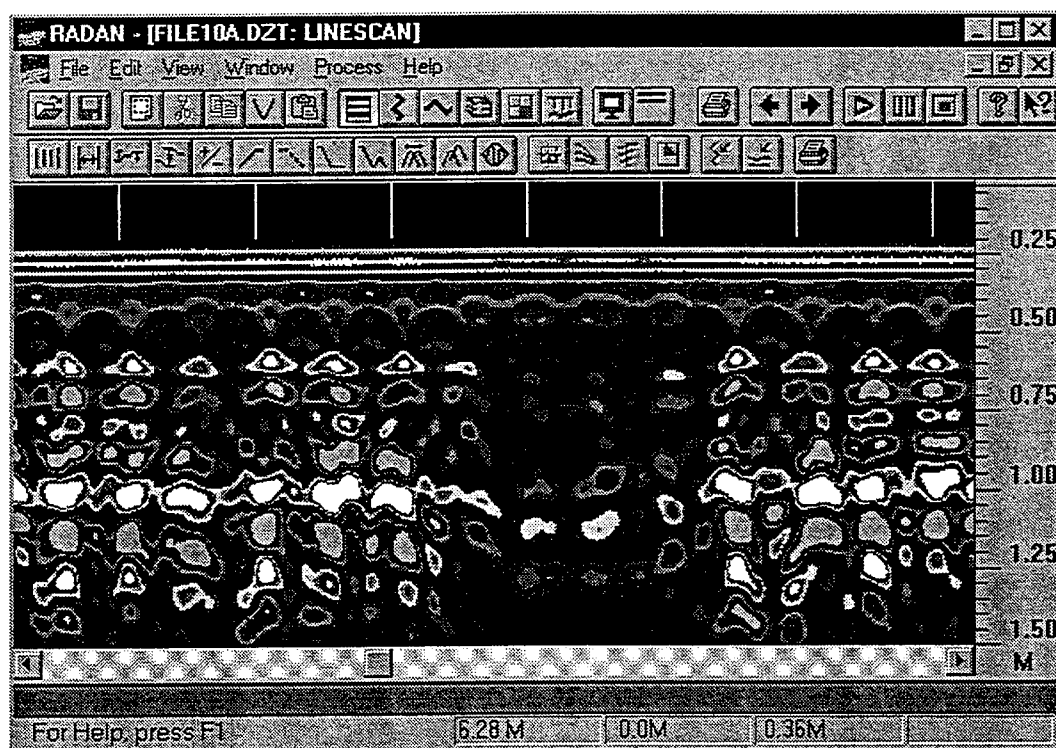


Figure 5.9: Example of a *RADAN* color linescan image.

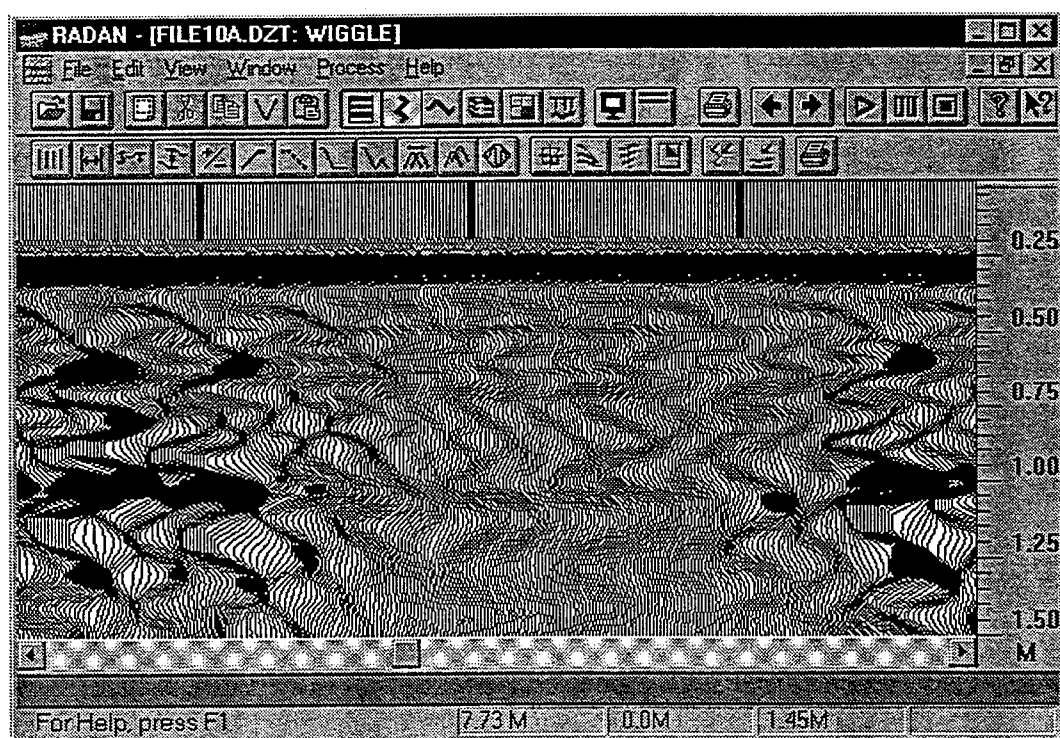


Figure 5.10: Example of a *RADAN* wiggle plot image.

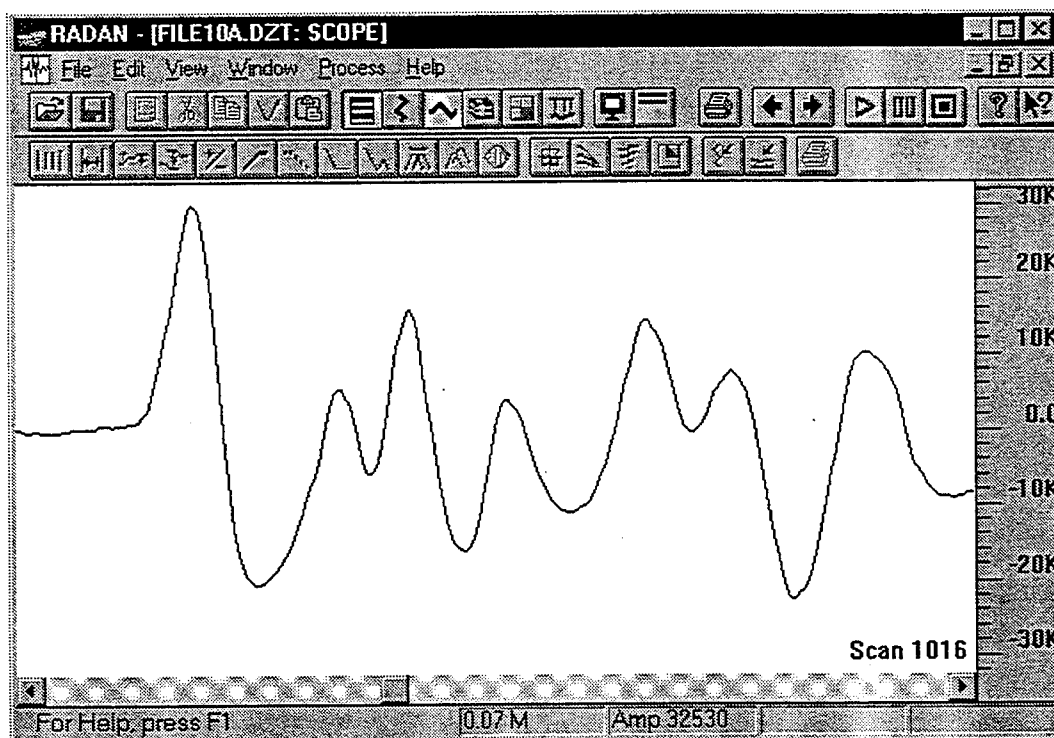


Figure 5.11: Example of a *RADAN* oscilloscope trace.

- *Restore Gain and Range Gain Functions*

Any gain applied to the data during acquisition can be removed if so desired using the *Restore Gain* function. The *Range Gain* function allows the user to automatically or manually add or remove gain to the data.

- *Hilbert Transform*

The *Hilbert Transform* feature will decompose the radar signal, which is represented as a time series, into its magnitude, instantaneous phase, or instantaneous frequency components. This is useful when trying to detect subtle features in the data, since phase information is sometimes more sensitive to dielectric changes than amplitude.

- *Deconvolution*

Multiple reflections, better known as “ringing,” can occur when the radar signal bounces back and forth between an object and the antenna. This can obscure information at the lower depths. The *Deconvolution* function is a filtering method used to remove any ringing phenomenon.

- *Migration*

Because the radar antenna radiates energy with a wide beamwidth pattern, objects of finite dimensions may appear as hyperbolic reflectors on the radar profile. Steeply dipping surfaces will also cause diffracted reflections of the radar signal. *Migration* is a technique that collapses hyperbolic diffractions into their approximate true shapes and moves dipping reflectors to their true positions.

- *Arithmetic Functions*

It may be desired to perform simple arithmetic functions on the data. The functions allowed are negation, absolute value, differentiation, integration, squaring, square root, natural log, and exponent.

In addition to signal processing, *RADAN* allows for data corrections and conversions. Static, horizontal scaling, distance normalization, and topographic corrections can be performed on data. Static correction compensates for variations in elevation, phase shifts, and high frequency noise observed in the horizontal (spatial) direction without affecting the vertical frequency. Distance normalization is a very useful function which puts equal horizontal spacing between scans and is used when the use of a survey wheel is not available. Data can be converted into SEG-Y, ASCII, or database (Microsoft Access) formats.

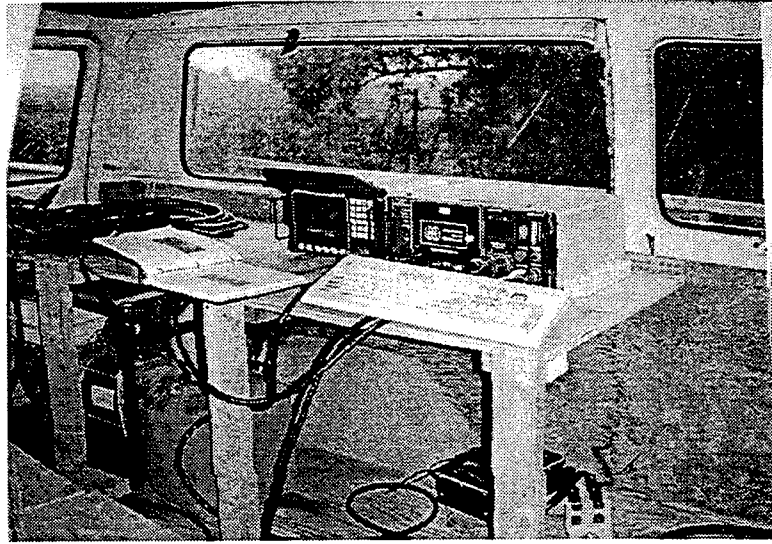


Figure 5.12: View of the internal van set-up.

5.6 Van and Antenna Pullcart

A university van provided a portable “homebase” for the equipment when taking bridge data. The inside of the van was modified to meet the needs of the equipment and research team (Figure 5.12). A table was constructed, as well as wooden boxes which served the dual purpose of storage and seating. Power lines were run from the battery to the interior of the van to provide a 12 VDC power source for the radar system. A hitch ball was attached to the rear bumper to provide an attachment for a pullcart on which the antennas were mounted.

A simple pullcart was constructed as a mount for the antennas. The pullcart was constructed using 5 cm (2 in) x 10 cm (4 in) pinewood, wood screws, lawn mower wheels, nuts, bolts, and a hitch. A picture of the pullcart, with the antennas mounted, is shown in Figure 5.13. The cart allows for the mounting of one 400 MHz antenna, up to three 900 MHz antennas, and up to two 100 MHz antennas (not used in this research project). Ideally, the antennas should be in direct contact with the ground to provide for good coupling of the signal into the ground. However, since the antennas were going to be mounted on

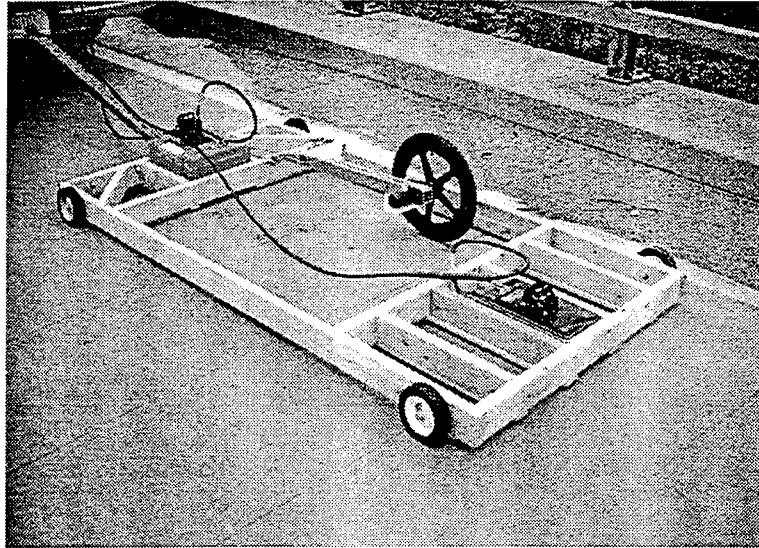


Figure 5.13: Picture of the pullcart designed for towing the antennas.

the pullcart, some space had to be allowed between the antennas and the ground. After consultation with GSSI, it was decided that the antennas should be no more than one-eighth of a wavelength of the highest frequency antenna above the ground. For the 900 MHz antenna, one-eighth of a wavelength is approximately 4 cm. Therefore, the cart was designed to allow for 2.5 cm clearance between the bottom of the antennas and the ground. The cart was also made small enough to fit in the van for transportation to and from the bridge site, eliminating the need for lights and licensing. Cart specifications are listed in Table 5.6.

Table 5.6: Pullcart Specifications

Material	5 cm x 10 cm pinewood
Dimensions	9 cm x 107 cm x 204 cm
Ground Clearance	2.5 cm

Chapter 6

Experimental Setup

6.1 Control Data Collection Setup

6.1.1 Construction of Bridge Deck Model

A concrete slab containing four rebars was constructed in an attempt to model a section of a bridge deck. Its purpose was to provide a means for collecting data in a controlled, laboratory environment and for determining a threshold level used for deciphering between good and deteriorated sections. Figure 6.1 illustrates the layout of the model. The model was constructed using 272 kg of pre-mixed Portland cement obtained at a local hardware store. The dimensions of the model are 15.2 cm (6 in) x 61.0 cm (24 in) x 152.0 cm (60 in). Two good rebars and two corroded rebars measuring 3.1 cm (0.5 in) in diameter were placed in the center of the model with a 20.3 cm (8 in) spacing and 5.1 cm (2 in) of concrete cover. Concrete-only sections of 45.7 cm (18 in) were allowed on both ends to prevent the intermixing of signal returns from the edges of the slab with returns from the rebars. The concrete was allowed to cure for three weeks.

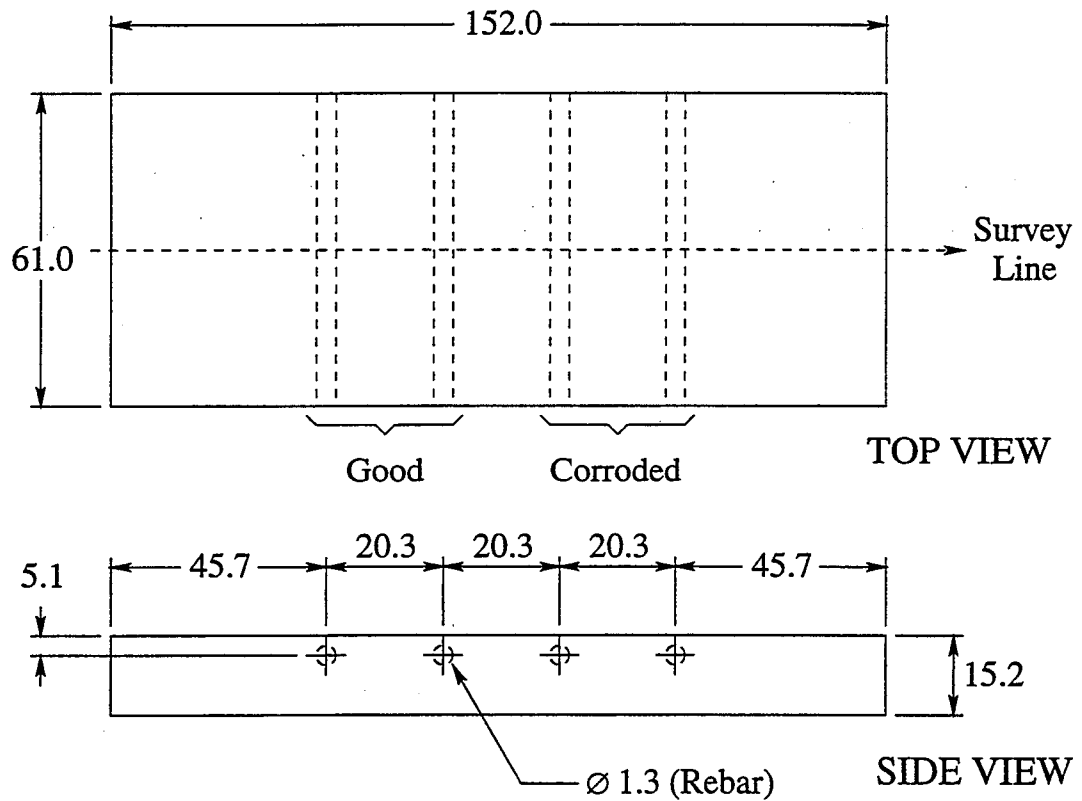
When collecting control data, radar parameters were set to approximately match the set up that would be used in the field. The parameters are given in Table 6.1.

6.1.2 Calibration

After setting the length of the time window at 10 ns for the 900 MHz antenna and 20 ns for the 400 MHz antenna, the signal is positioned by placing the first (surface) reflection at

Table 6.1: Radar Setup Parameters Used for Collecting Data

PRF (kHz)	52
Scans / Sec	50
Samples / Scan	256
Time Window (ns)	10
Number of Gain Points	5



All Dimension in cm

Figure 6.1: Layout of the bridge deck model constructed in the laboratory. The slab was constructed using pre-mixed Portland cement and contains a total of four rebars, two good and two corroded.

the beginning of the time window. An automatic range control initially attempts to place the second zero crossing at the beginning of the window. The signal can then be manually moved to place the full surface reflection near the beginning of the window.

Initial calibration of the radar gains is accomplished using the automatic gain control (AGC) feature of the radar. The antenna is placed at a random position in the middle of the slab, and the “Auto Gain Servo” selection is chosen. The oscilloscope window is partitioned into four areas, corresponding to five range gain points. The radar automatically attempts to adjust the gain at each point so that the entire signal falls within approximately 70% of the window along the amplitude axis. The automatic gain is then disabled, and the antenna is pulled across the slab. The signal is observed in the oscilloscope window using the data collection software. If no clipping occurs, the gains are locked and all gain setting controls are disabled. If clipping occurs, the gains at each point are manually adjusted until the signal falls within 70% of the window. At this point the gains are locked and remain constant for the duration of the data collection campaign.

Filters must be set when necessary. If using post-processing software, most filtering can remain off during data acquisition to avoid attenuating significant events. However, there are cases when filters need to be utilized in the field. Of greatest concern is the removal of unwanted, low frequency noise, also known as *tilt*. If the data appears to “tilt” downward within the oscilloscope window, the vertical IIR high-pass filter should be set to remove the low frequency noise.

The above calibrations were performed in accordance with the recommended procedures given in the GSSI SIR-10B User’s Manual [GSSI, 1996].

6.1.3 Collection of Control Data

Control data were collected by pulling the antenna at a fairly constant speed lengthwise down the center of the cement slab model. The procedure was repeated many times for

varying speeds and two different users. All data were stored on the system's hard drive and later transferred to a personal computer for post-processing.

6.2 Experimental Bridge Deck Data Collection Setup

6.2.1 Bridges Studied

Data were collected for ten different bridges. Table 6.2 lists each bridge surveyed as well as other relevant information pertaining to each bridge and the survey. With the exception of the first bridge listed, all bridges were chosen by Dave Hall, Unit Supervisor of the Materials and Test Division of the Nebraska Department of Roads. The bridge near Louisville contains an asphalt overlay and was included in an attempt to study the effects of asphalt on radar data. Six of the bridges had existing records of delamination data taken using traditional methods, providing "ground truth" data for comparison with the radar data. Records were not available for the North 38th Street (East Campus), Adams Street, DuBois, or Louisville bridges; data had never been taken for the North 38th Street bridge, and the Nebraska Department of Roads reports for the Adams Street and DuBois bridges were still in progress at the time this thesis was written. A report was available for the Louisville bridge, but lacked delamination data since the asphalt overlay prevented delamination detection through conventional sounding methods. Because of its ease of access and low traffic, the North 38th Street bridge, located on the East Campus of the University of Nebraska - Lincoln, was chosen for the primary purpose of familiarizing the researchers with the radar system. The dates and times of all other data collection campaigns, as well as arrangements for traffic control, were coordinated through Dave Hall.

6.2.2 Calibration

Calibration of the radar system in the field was done in the same manner as in the laboratory using the parameters given in Table 6.1.

Table 6.2: Bridges Studied

Bridge Information				Survey Information			
Highway/Street Nearest Town	Mile Marker	Year Built	Asphalt Overlay	Survey Date	Local Time	Temp. ° C (° F)	Relative Humidity %
N. 38th St. (EC) Lincoln, NE	N/A	1986	No	06/12/97	1930	22 (71)	79
Adams St. Lincoln, NE	N/A	1961	No	06/17/97	1130	30 (86)	28
HW 63 Ithaca, NE	33.50	1958	No	07/28/97	1030	23 (74)	92
HW 63 Ithaca, NE	34.87	1958	No	07/28/97	1130	25 (77)	85
HW 63 Ithaca, NE	37.20	1958	No	07/30/97	0830	19 (67)	65
HW 63 Ithaca, NE	32.95	1958	No	07/30/97	0950	21 (70)	58
HW 8 DuBois, NE	126.72	1959	No	08/04/97	1000	22 (71)	56
HW 43 Bennet, NE	14.41	1961	No	08/06/97	0800	18 (64)	68
HW 43 Bennet, NE	14.60	1961	No	08/06/97	0915	18 (65)	61
HW 50 Louisville, NE	79.70	1951	Yes	08/13/97	0930	18 (65)	64

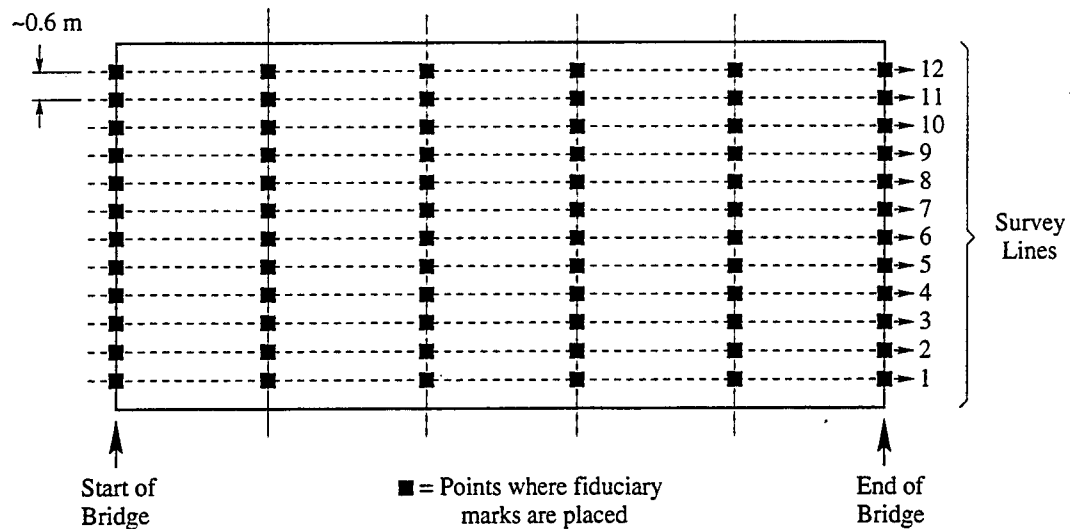


Figure 6.2: Illustration of how a bridge is gridded prior to data collection (top view). The filled squares indicate points where chalk marks are placed on the bridge deck and where fiduciary marks are placed on the data record.

6.2.3 Gridding the Bridge Deck

After calibration, the bridge was gridded using chalk. Figure 6.2 illustrates how a bridge is gridded prior to data collection. The filled squares indicate points where chalk marks are placed on the bridge deck and where fiduciary marks are placed on the data record. Survey lines were separated by a distance of 60 cm (24 in) except for the Adams Street bridge which were separated by 90 cm (36 in). One of the two white shoulder lines served as the first survey line. The Louisville bridge, however, had an extremely wide shoulder, so the first survey line was taken 120 cm from the east edge of the bridge.

6.2.4 Log Sheet

Before collecting bridge deck data, information pertaining to the site and survey were recorded on a log sheet. The information included the approximate location relative to the nearest town, the highway or street on which the bridge was located, mile marker number, time, date, temperature, relative humidity, and the name of the directory under which the bridge data would be stored on the hard disk. A rough sketch of the bridge geometry

and gridding information (survey line direction, name of the file for each survey line, and fiduciary mark location) were also included. An example of a completed log sheet is shown in Figure 6.3.

6.2.5 Collection of Bridge Deck Data

Traffic control was provided by Nebraska Department of Roads personnel. In order to keep the disruption of traffic to a minimum, one lane was kept open while data was collected on the other lane. Data was collected as the van and radar system were driven along each survey line, keeping the rate of travel as constant as possible. After collecting data on the first couple of bridges, and since all of the bridges surveyed were fairly short in length, it was found that backing the van up after completing each survey line was much easier than turning it around due to the poor turning ability of the cart.

Although the survey wheel discussed in Chapter 5 was available, it was not used due to difficulties encountered with it in the field. The calibration of the survey wheel was completed and the procedures for its use were followed as given in the user's manual. GSSI was consulted, and their initial statement was that although the survey wheel could be used with the SIR-10B system, the rate of travel must be extremely slow in order to collect data properly. Months later, GSSI claimed that their user's manual contained many errors, including how to properly set the radar settings for survey wheel use. GSSI plans to release a revised manual in the near future. Although the survey wheel was not used, the lengths of all survey line data records were approximately equal. Distance normalization was performed on all data during post-processing to make each survey line of a bridge the same length.

6.2.6 Data Transfer and Back-Up

After a data collection campaign, all data were copied to a PC via a parallel link. The data were also copied to 8 mm data cartridges using an external tape drive.

Location BENNET, NE

Highway # 43 Year Constructed 1961

Mile Marker # 14.60 Asphalt? Yes / (No)

Date 8/6/97 Time 0915

Temperature 18°C (65°F) Relative Humidity 61%

Data Directory Name 08-06-97.001

N
W —+— E
S

WHITE LINE →

0.6m

START

③ ④ ⑤ ⑥ ⑦ ⑧ ⑨ ⑩ ⑪ ⑫ ⑬ ⑭

4.9m

4.9m

4.9m

4.9m

(FIDUCIARY MARKS EVERY 4.9m)

FILE ① : TEST

② : BAD

Figure 6.3: Example of a log sheet completed in the field prior to collecting bridge deck data.

Chapter 7

Experimental Results

Before analyzing the data, the data had to be processed into a form suitable for analysis. GSSI's *RADAN* post-processing software was used to accomplish this. Following post-processing, the data were analyzed using two methods, termed the Constant Threshold Level (CTL) and Varying Threshold Level (VTL) methods. The Constant Threshold Level method involved setting a universal threshold level to separate the good areas from the deteriorated areas, and is treated in depth. The Varying Threshold Level method, discussed briefly, involved the same data analysis techniques as the Constant Threshold Level method with the exception that the threshold level was varied from bridge to bridge until the percentage of deterioration matched that of the ground truth data. The purpose of using both methods was to investigate whether a universal threshold holds for all bridges or depends on the individual bridge under examination.

7.1 Post-Processing

The first post-processing step involved reversing the order of certain survey line files so that all of the survey lines ran the same direction. This is accomplished in *RADAN* by simply choosing the File|Save As|Reverse option. Reversal was required only for the Adams Street bridge and the Ithaca bridge located at mile marker 33.50.

Since a survey wheel was not used, the next step involved normalizing the horizontal distances of each survey line using the *Data Normalization* function in *RADAN*. This ensured that all survey lines for a bridge were the same length. This was a very lengthy and

cumbersome process since all survey line files for each frequency had to be individually normalized. For the ten bridges surveyed, a total of 198 survey line files were distance normalized, each averaging five to ten minutes to complete. Also, some of the bridges were skewed at each end, giving the bridges a parallelogram shape. Since transverse rebars are not located within the skewed ends, they were excluded from analysis.

After all files were distance normalized, the data were filtered if necessary. None of the 400 MHz data files required filtering. Both high pass and low pass filtering were required for about half of the 900 MHz data files. The low pass filter was used to eliminate any high frequency noise present in the data, while the high pass filter was used to rid the data of low frequency tilt. This step was fairly rapid since *RADAN* allowed multiple files to be processed at the same time.

Finally, each survey line file had to be converted to ASCII format for analysis using Matlab 5.1. This was done using GSSI's *RADAN to ASCII Conversion Utility*. Again, this step proved to be very time consuming since only one file could be converted at a time. The ASCII files were also very large. The *RADAN* data files averaged approximately 1 to 3 MB in length, while the ASCII files averaged 5 to 9 MB.

7.2 Data Analysis Procedure

As discussed in Chapter 5, the *RADAN* software package allows the user to view the radar return data via very sophisticated images. Recognizing which rebars within a bridge deck are corroded, however, becomes a matter of the opinion of the observer. A more automated process is desired which makes a decision of "good" or "bad" based on certain parameters.

The type of return signal from a bridge deck can fall into one of three categories: return from a good rebar (little or no corrosion), return from a bad rebar (somewhat corroded to highly corroded), or return from an area without a rebar. A parameter which should theoretically be different in all three cases is the *variance* of the return signal, provided the

Table 7.1: Variance Ratios Calculated From 1-D Computer Simulations

Ratio	400 MHz	900 MHz	400 MHz (Loaded)	900 MHz (Loaded)
Case 1:Case 2	3.15:1	3.20:1	3.23:1	3.16:1
Case 3:Case 4	4.56:1	4.18:1	4.35:1	4.42:1

surface and rebar reflection overlap is not extreme. Calculating the variance of each return signal, in addition to taking advantage of the symmetry and repetitive nature of the rebar layout within a bridge deck, formed the basis for analyzing all data.

All data were analyzed using algorithms written for Matlab 5.1 which calculated the variance, σ^2 , of each individual return scan. Intuitively, rebars with little or no corrosion will exhibit high reflectance and therefore high variance return signals. Rebars with a high level of corrosion should produce return signals with variances lower than that of non-corroded rebars since the energy reflected from the corroded rebars will be lower. If no rebar is present, the return signal will not contain a return pulse from the rebar level and should exhibit the lowest variance of all three cases. To prove this, the variance ratios of good to corroded rebars were calculated for the one-dimensional computer simulations of Chapter 4. As seen in Table 7.1, the variances of the return signals from good rebars are three to four times higher than that of corroded rebars. The variance of a set of N samples x_1, x_2, \dots, x_n with mean μ_s is given by

$$\sigma^2 = \frac{1}{N} \sum_{i=1}^N (x_i - \mu_s)^2 \quad (7.1)$$

Only the first portion of the signal which contains the surface and rebar reflections is of interest, since everything beyond can greatly influence the variance. After observing the wiggle plot representations of the bridge decks using *RADAN*, it was decided that the cut-off point should be just after the point where two consecutive hyperbolas overlapped.

If the rebar were spaced far enough apart so that no overlap took place, the cut-off point was chosen so that the entire “tails” of each hyperbola were included.

The variance can differ greatly from one scan to the next, mainly depending on how quickly the hyperbolas fall off and whether or not they overlap, and can appear very “noisy” when plotted versus scan number. An illustration of the variance plotted versus scan number for one survey line is given in Figure 7.1. To smooth the variance data set, a sliding average technique is used in which a finite number of points is averaged into one point. The averaging is done for each survey line with the number of points averaged chosen to be equal to the number of scans between two consecutive rebars. Consider an example in which the survey line files of a bridge deck exhibit 50 scans between rebars. If 50 points are averaged into one point, the first point would be the average of the first 50 points, the second point would be the average of the second through fifty-first point, etc., continuing to the end of the survey line data set. Consequently, there will be 50 less points in the averaged data set than in the original data set. Since the rebars within a bridge deck are all equally spaced and at approximately the same depth, the averaged values should remain fairly constant from rebar to rebar if all rebars are in the same physical condition and environment. If a rebar with higher corrosion than the surrounding rebars is encountered, the average will drop due to the lower variances of the return signals in that area.

After all variances were calculated and averaged, the results were normalized in a fashion to be discussed later. This was done to reference all data sets to the same scale. The variance data of Figure 7.1, after averaging and normalization, are shown in Figure 7.2.

7.3 Constant Threshold Level (CTL) Method

The Constant Threshold Level method investigated here involves finding a universal threshold level (one for each frequency) to be used for all bridges. Any variance values which fell below this level were considered “bad” and anything above were considered “good.” The

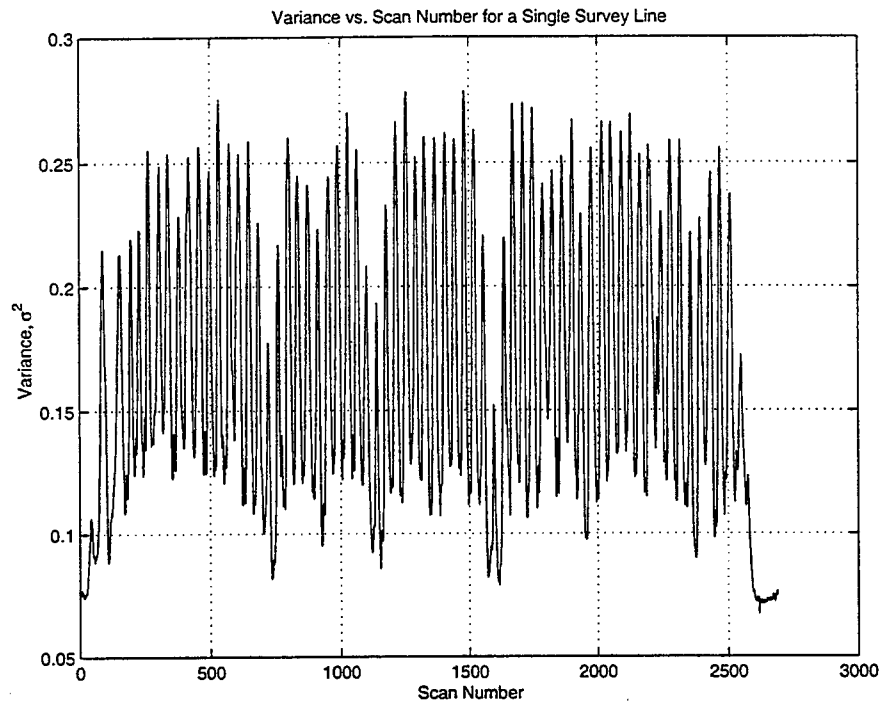


Figure 7.1: Example of variance plotted against scan number for a single survey line. Note that the plot appears “noisy.”

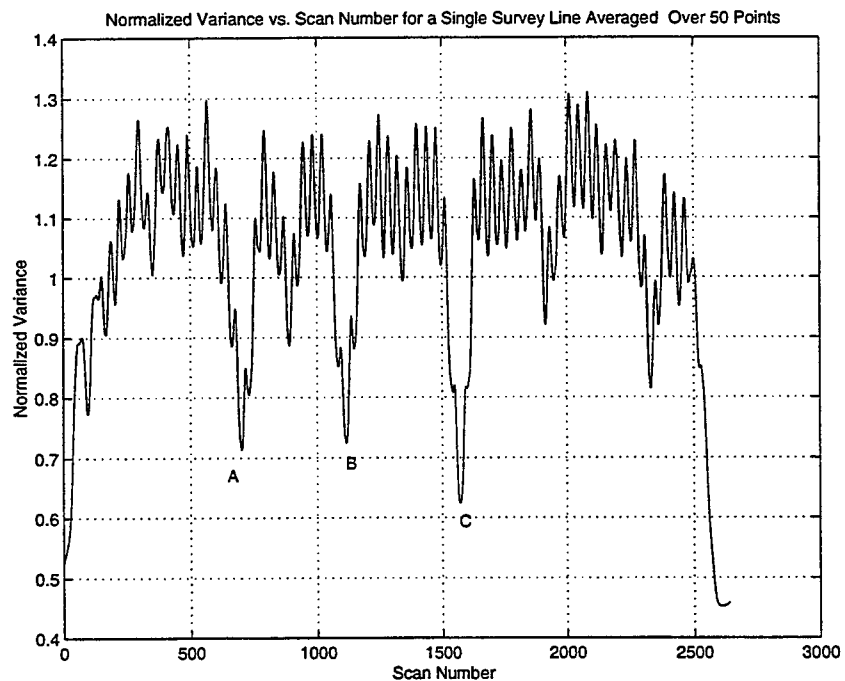


Figure 7.2: Data of the previous figure after averaging over 50 scans, which is the number of scans between two consecutive rebars. The bad sections of this particular survey line are easily seen at points A, B, and C.

areas which fell below this threshold level were highlighted on a two-dimensional plot which represented the top view of the bridge deck. A grayscale format was utilized to indicate the degree to which an area falls below the threshold level. The grayscale ranged from black, representing the minimum variance value, to white, representing variance values which are above the threshold level.

7.3.1 Model Bridge Deck Data Analysis Results

The threshold levels were determined from the control data collected on the model bridge deck. After collecting the data and viewing them in *RADAN*, it was seen that the distance between the surface and the first noncorroded, “good” rebar was half that of the other three rebars. This could have been due to the rebar floating upward during the pouring of the concrete. The overlap of the surface and rebar pulses was very extreme; therefore, this rebar was excluded in all data analysis.

Data for one survey line, which ran down the middle of the slab, were collected three different times for each antenna. After post-processing, the data were analyzed using the Matlab 5.1 algorithms. The variance values of all scans were normalized to the average variance of the scans in the range $[-0.5 \times \text{rebar spacing}, +0.5 \times \text{rebar spacing}]$ centered around the good rebar. In this case, the area was ± 0.10 m around the good rebar. Since two of the three rebars exhibit corrosion, the amount of deterioration should ideally be 66.67%. The algorithms were executed numerous times for both the 400 MHz and 900 MHz data sets for varying threshold levels until the percentage of deterioration was equal to this ideal value. The threshold levels (one for the 400 MHz data and another for the 900 MHz data) for all bridges surveyed were then set at those values, listed in Table 7.2. Figures 7.4 and 7.5 represent 2-D plots of deterioration areas found from the 400 MHz and 900 MHz data, respectively. Figure 7.6 shows the areas of agreement between both the 400 MHz and 900 MHz data sets. The three survey lines are shown parallel to one another.

Table 7.2: Threshold Levels Determined From Studies of the Model Bridge Deck

Data Set	Threshold Level	Deterioration % of Total Deck	Comparison to Ideal (66.67%) % Match
400 MHz	0.8230	66.67	100.00
900 MHz	0.8100	66.67	100.00
400 and 900 MHz	—	65.84	98.78

Since it is not known *a priori* which rebars within a bridge deck are good or bad, it was decided to use the mean variance of the n consecutive rebars exhibiting the highest variance of all survey lines, where n is 10% of the total number of rebars within the bridge deck, for the normalization.

The variance simulations also allow us to determine the reflectivity of the corroded rebar. In Chapter 4, the reflectivity of the corroded rebar was assumed to be equal to -0.35 in the simulations. Simulations were performed of the model bridge deck geometry for various values of corroded rebar reflectivity, and it was found that a value of -0.35 yielded a threshold of 0.81 for the variance ratio, which matched the measured data. Figure 7.3 shows the variance of the simulation (for a corroded rebar reflectivity of -0.35) plotted against scan number, in which the dotted line indicate the threshold level obtained from the measured data.

7.3.2 Ground Truth Data

The ground truth (or chain drag) data for six bridges, located at mile markers 14.41, 14.60, 32.95, 33.50, 34.87, and 37.20, were obtained from the Nebraska Department of Roads. A CAD program was used to plot the areas determined to be delaminated. In order to compare the ground truth data to the experimental data, linear interpolation was used to put the data into matrices which matched the sizes of the experimental data matrices.

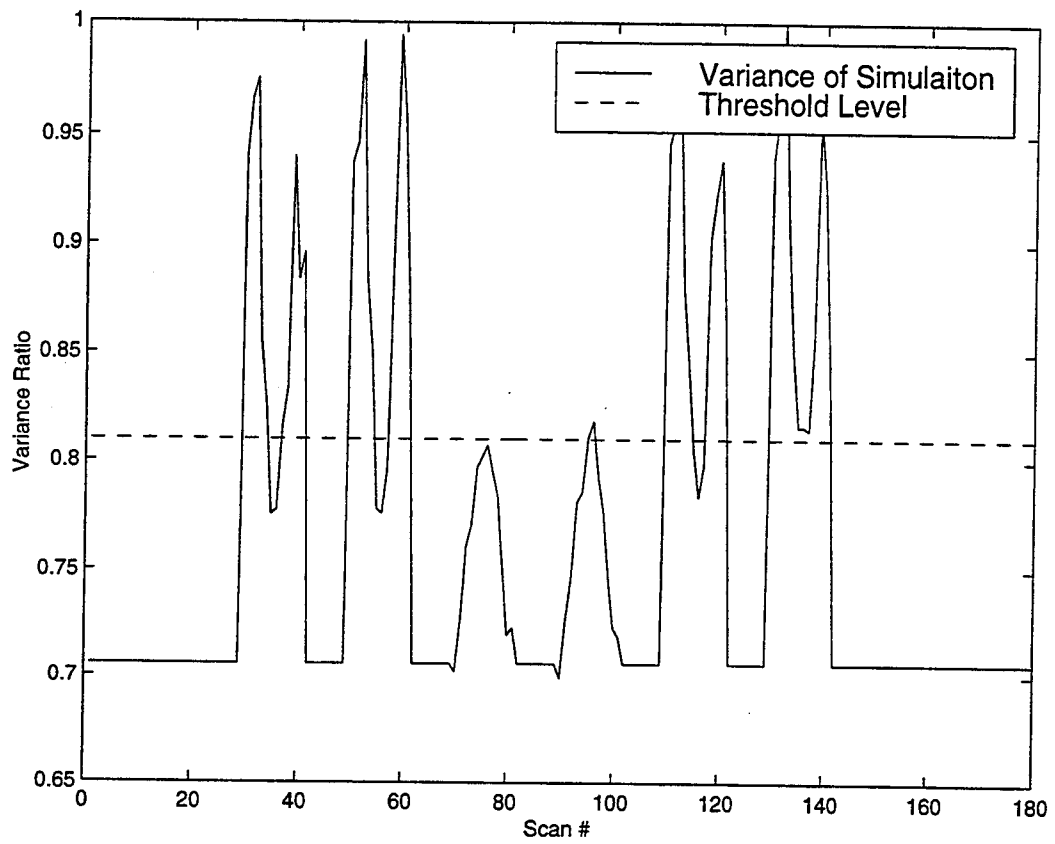


Figure 7.3: Variance plotted against scan number for model bridge deck simulations assuming corroded rebar reflectivity of -0.35.

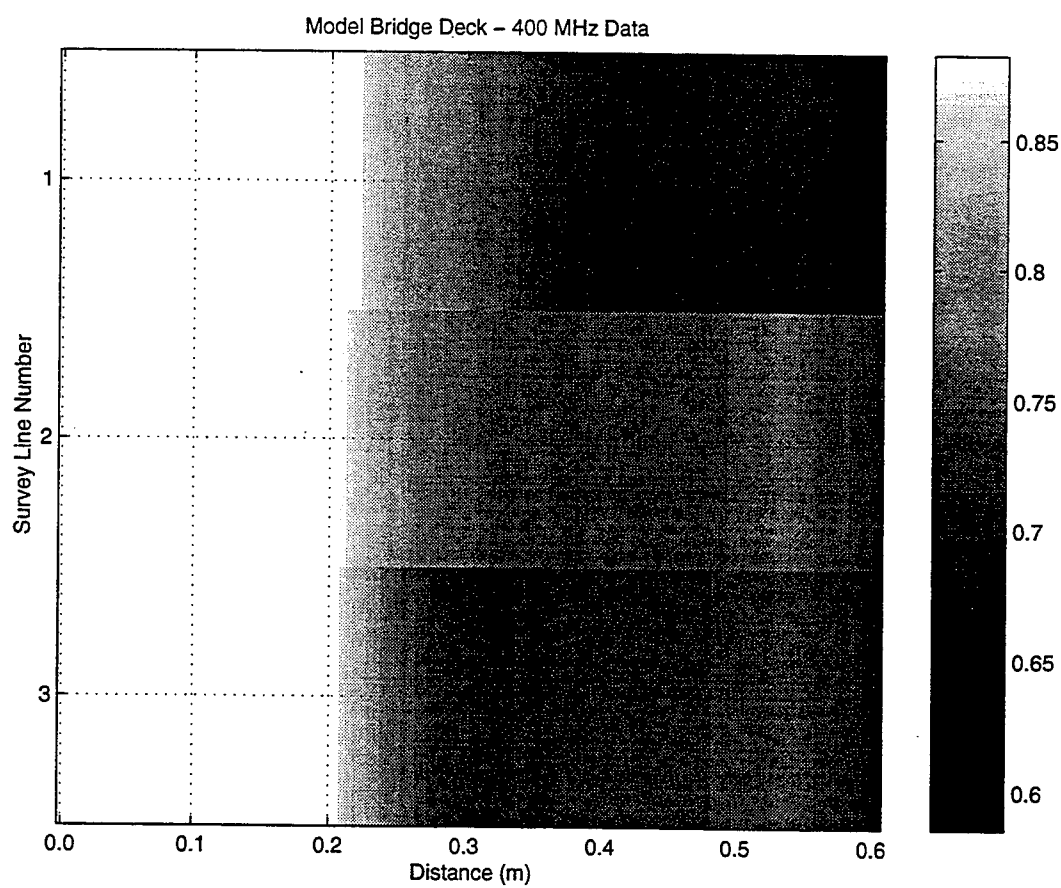


Figure 7.4: 2-D plot representing deterioration areas of the model bridge deck according to the 400 MHz data.

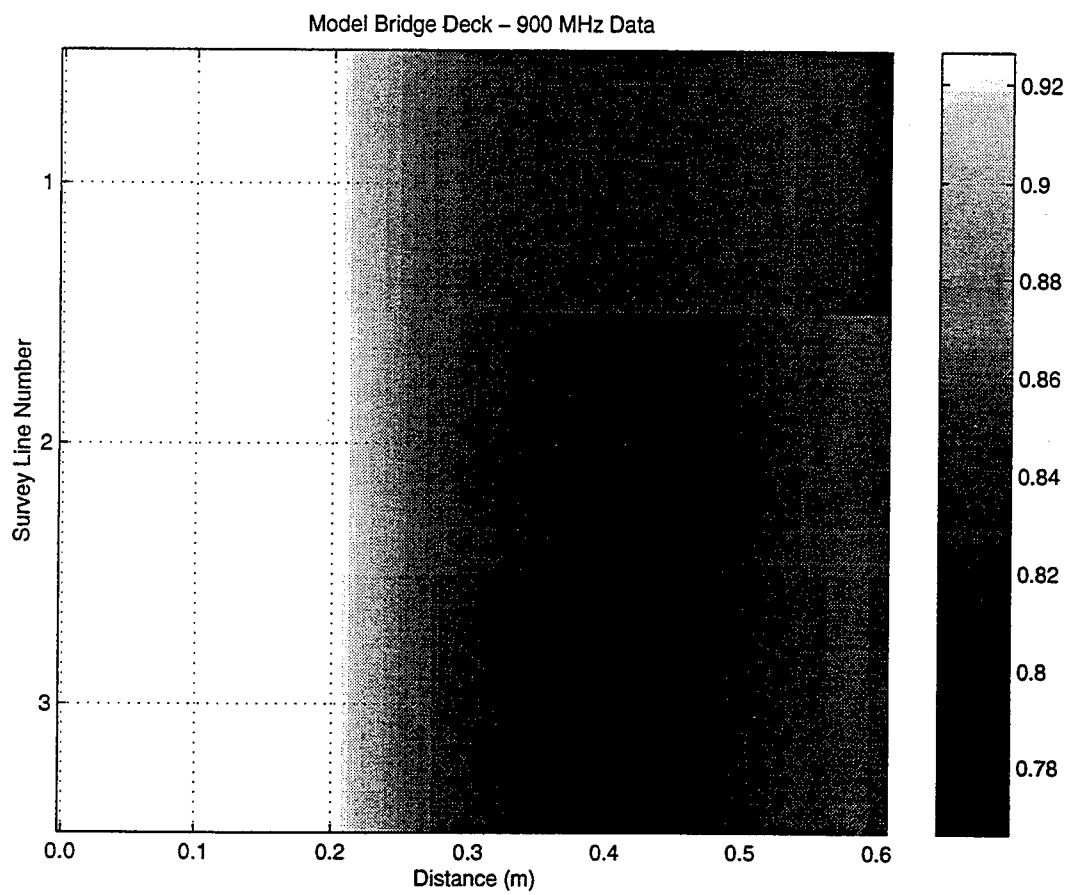


Figure 7.5: 2-D plot representing deterioration areas of the model bridge deck according to the 900 MHz data.

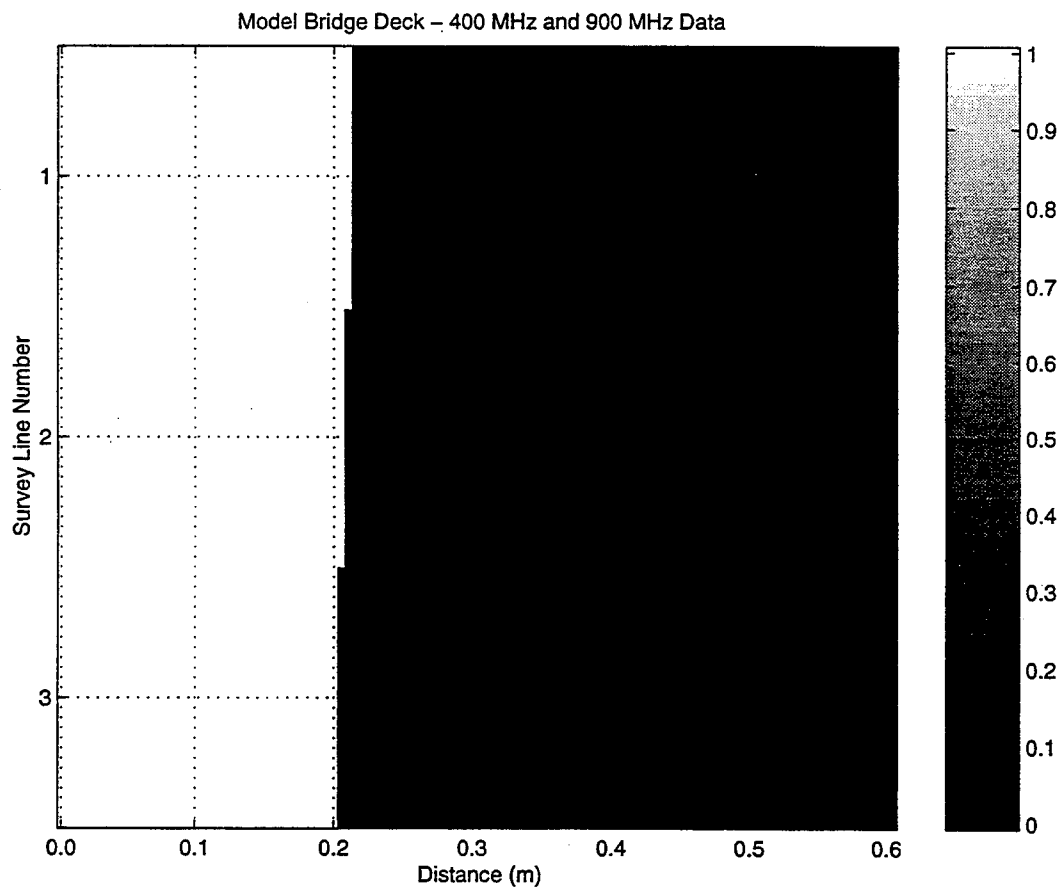


Figure 7.6: 2-D plot representing deterioration areas of the model bridge deck agreed upon by both the 400 MHz and 900 MHz data sets.

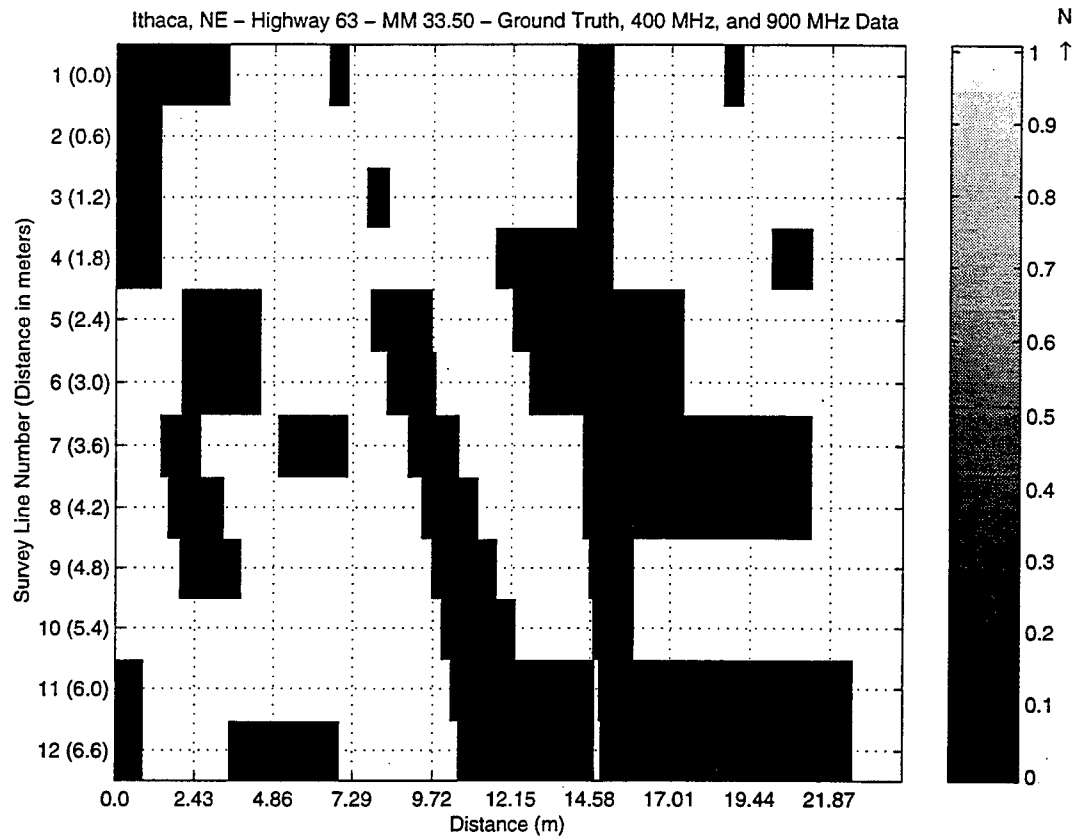


Figure 7.7: 2-D plot representing deterioration areas determined from a chain drag survey for the mile marker 33.50 (Highway 63) bridge.

The resulting ground truth data plots are given in Figures 7.7 through 7.12. According to the ground truth data, the best bridges were the mile marker 14.41 bridge with 1.49% deterioration and the mile marker 14.60 bridge with 6.06% deterioration. The worst bridge, being 33.43% deteriorated, is located at mile marker 33.50. Although ground truth plots for all bridges are shown, only the ones pertaining to these three bridges are given in the discussion of the results to conserve space.

7.3.3 Experimental Data Analysis Results

The results of the experimental data, given in terms of the percentage of bridge deck determined to be deteriorated, are given in Table 7.3. With the exception of the 400 MHz data for the bridge at mile marker 33.50, the percentage of deterioration given for all data sets

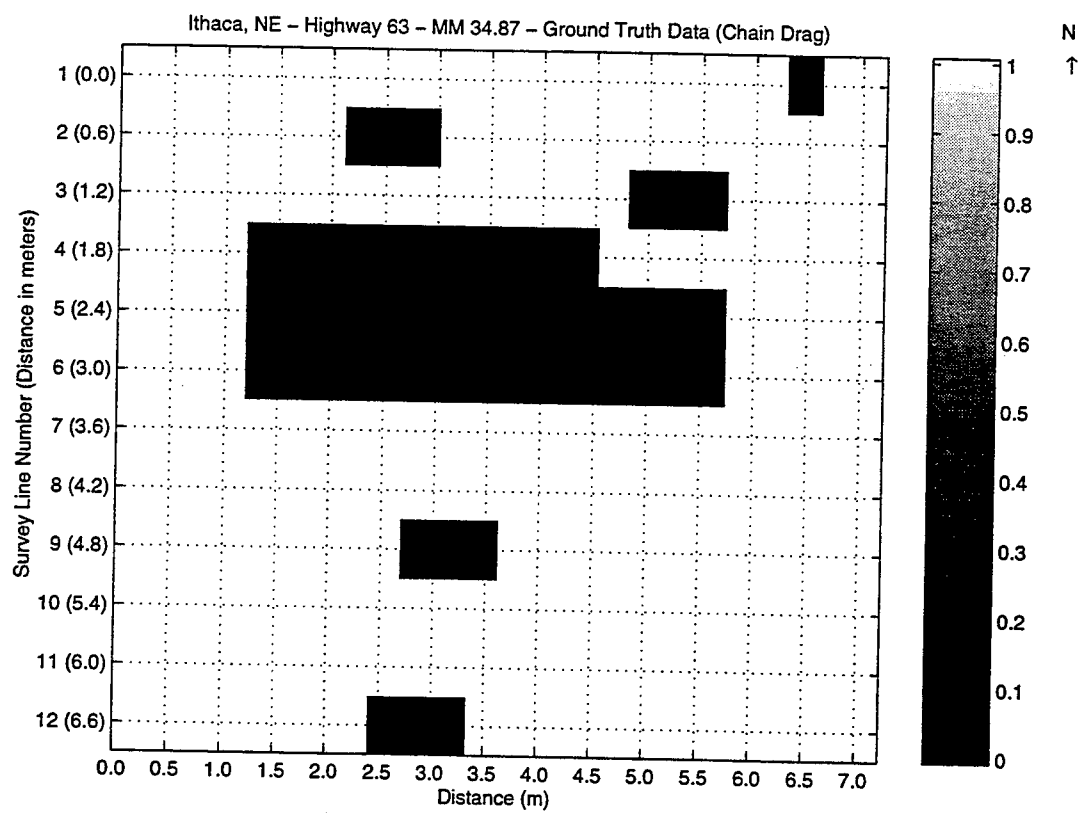


Figure 7.8: 2-D plot representing deterioration areas determined from a chain drag survey for the mile marker 34.87 (Highway 63) bridge.

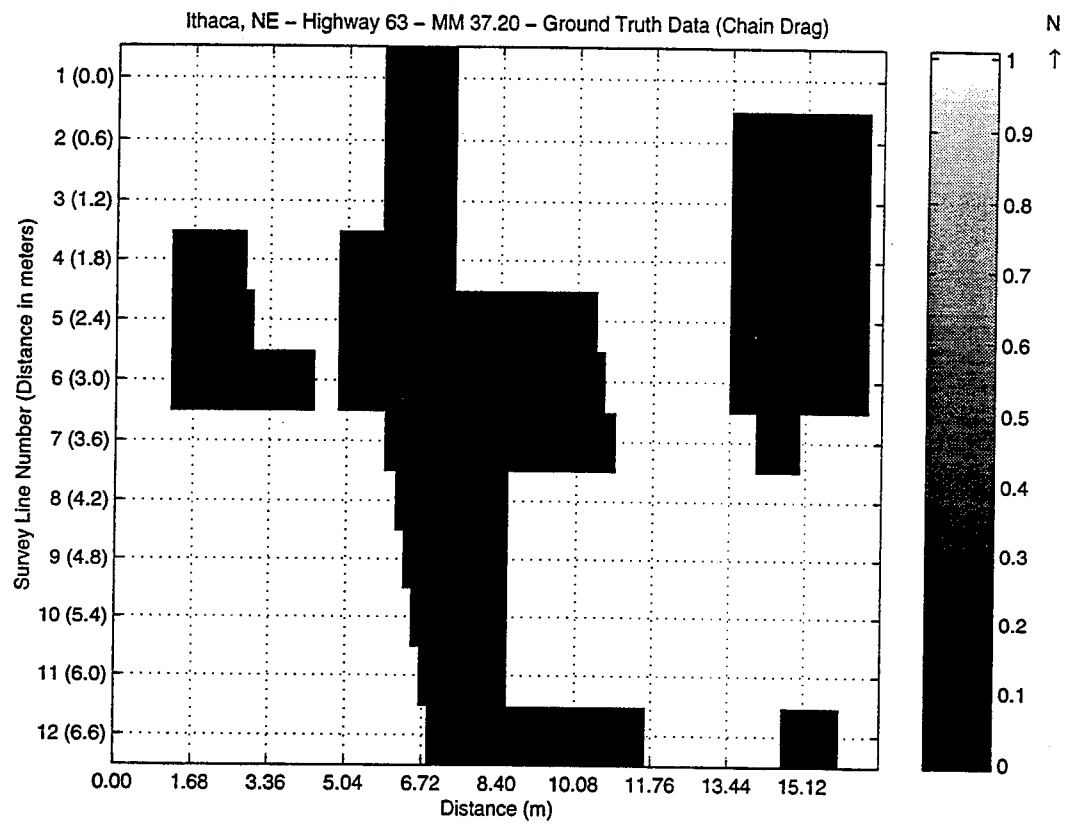


Figure 7.9: 2-D plot representing deterioration areas determined from a chain drag survey for the mile marker 37.20 (Highway 63) bridge.

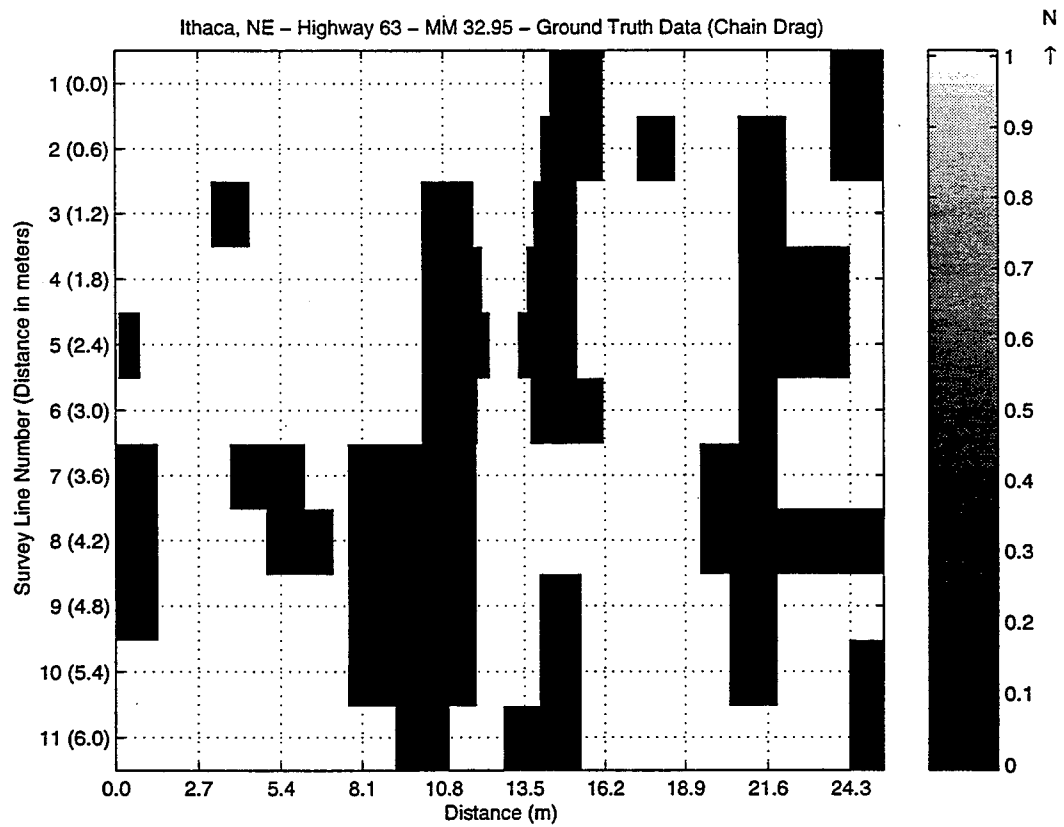


Figure 7.10: 2-D plot representing deterioration areas determined from a chain drag survey for the mile marker 32.95 (Highway 63) bridge.

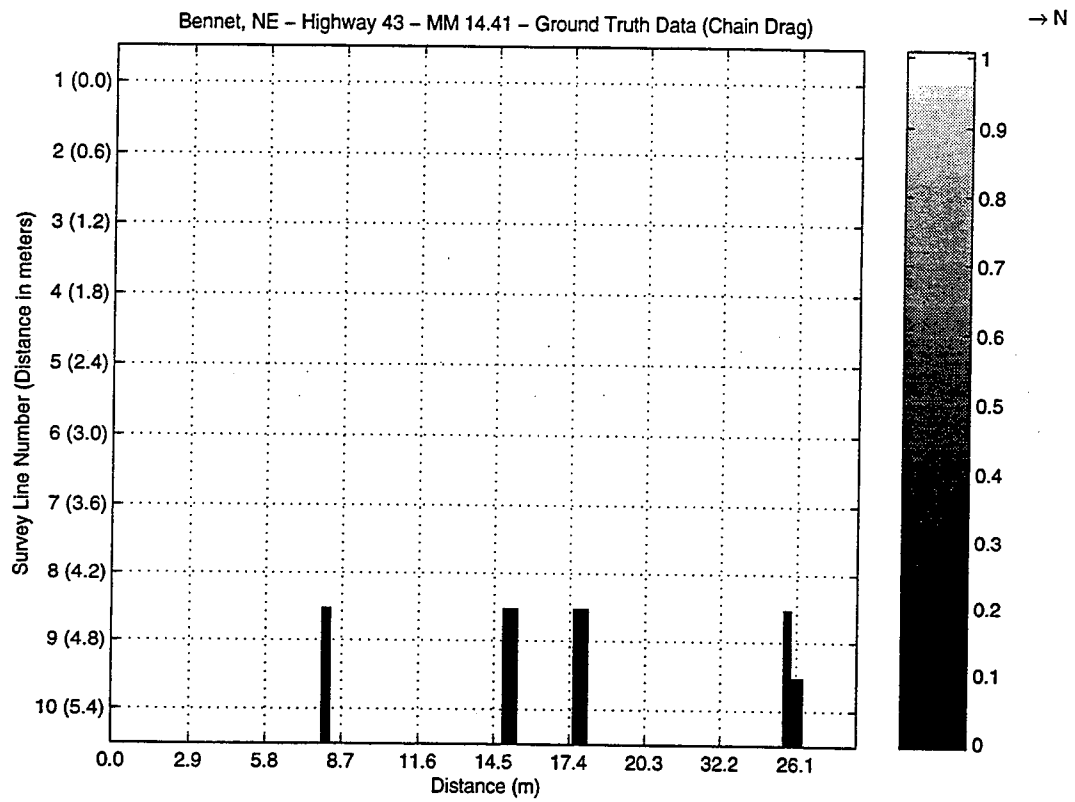


Figure 7.11: 2-D plot representing deterioration areas determined from a chain drag survey for the mile marker 14.41 (Highway 43) bridge.

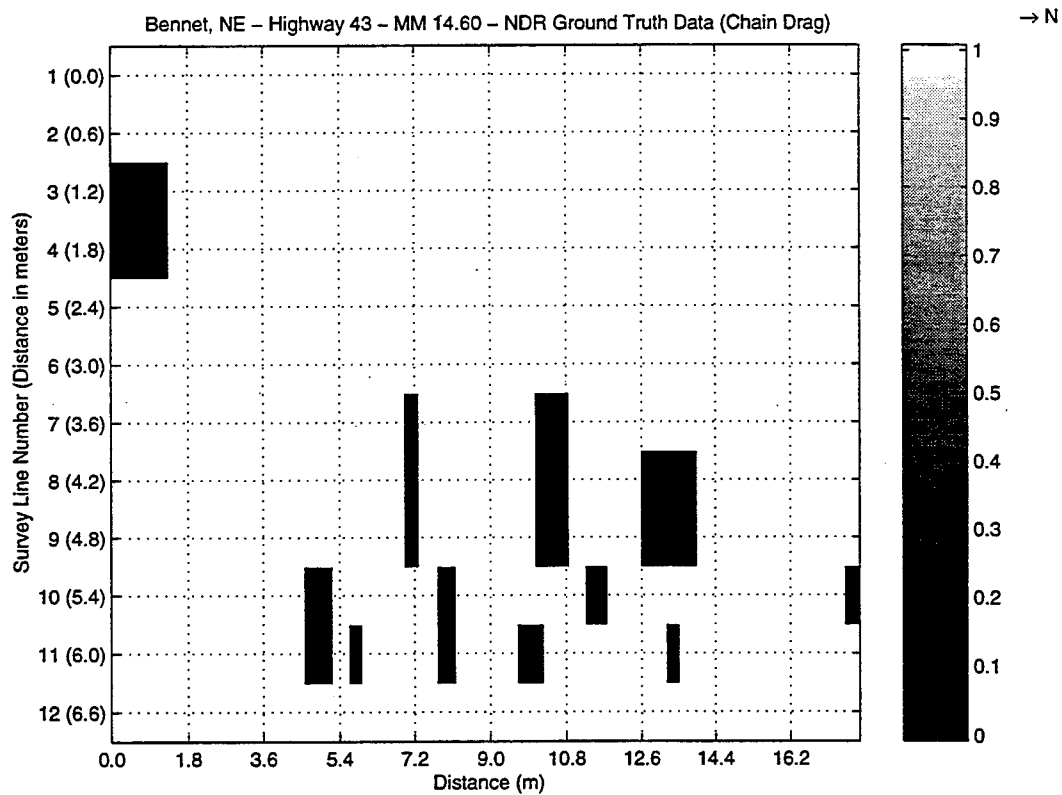


Figure 7.12: 2-D plot representing deterioration areas determined from a chain drag survey for the mile marker 14.60 (Highway 43) bridge.

is above that given by the ground truth data. Neither the 400 MHz nor 900 MHz data set agrees with the ground truth data as to which bridges are the best and worst. The results for the mile marker 14.41 and 14.60 and the Adams Street bridges may be high, however. It was found that the bridges at these locations have two different rebar spacings, 15.24 cm (6 in) and 30.48 cm (12 in). The survey lines containing the 15.24 cm rebar spacing show much more areas of deterioration than the survey lines with a 30.48 cm rebar spacing. This is evident in Figures 7.13 and 7.14, which are the 2-D plots of the 400 MHz and 900 MHz data, respectively, for the mile marker 14.41 bridge. Figure 7.15 shows the agreement between the two. The plots pertaining to the experimental data for the mile marker 14.60 and 33.50 bridges are given in Figures 7.16 through 7.18 and Figures 7.19 through 7.21, respectively.

When collecting 400 MHz data on the bridge at mile marker 14.60, the signal was not positioned correctly in the oscilloscope window. The majority of the surface reflection, therefore, was not recorded. It was found that the data could still be used to identify deteriorated areas. The threshold level of 0.823, however, proved to be too high. For convenience, the threshold level was adjusted until the percentage of deterioration matched that of the 900 MHz data.

The 400 MHz results for the asphalt-covered Louisville bridge, located at mile marker 79.70, was opposite of the results obtained at 900 MHz. Data was collected only for the east lane of this bridge. The 400 MHz data showed the area towards the center of the bridge to be bad, while the 900 MHz data showed that the majority of deterioration occurred near the shoulder of the bridge. The discrepancy could be due to the effects that the additional asphalt layer had on the variance. The 400 MHz pulse returns from the surface, asphalt-concrete interface, and rebars may have overlapped significantly, greatly affecting the variance.

Table 7.3: Experimental Data Analysis Results

Bridge Information		Results			
Highway/Street Nearest Town	Mile Marker	GT % Det.	400 MHz % Det.	900 MHz % Det.	400 and 900 MHz % Det.
N. 38th St. (EC) Lincoln, NE	N/A	N/A	6.99	21.66	3.82
Adams St. Lincoln, NE	N/A	N/A	45.69	35.97	24.32
HW 63 Ithaca, NE	33.50	33.43	9.75	69.15	6.56
HW 63 Ithaca, NE	34.87	18.99	61.36	45.43	20.59
HW 63 Ithaca, NE	37.20	30.77	85.41	71.74	60.24
HW 63 Ithaca, NE	32.95	30.34	39.65	71.59	25.95
HW 8 DuBois, NE	126.76	N/A	28.48	62.93	17.28
HW 43 Bennet, NE	14.41	1.49	30.53	34.78	19.06
HW 43 Bennet, NE	14.60 (see text)	6.06	7.78 (see text)	7.78	3.98
HW 50 Louisville, NE	79.70	N/A	51.59	88.57	49.85

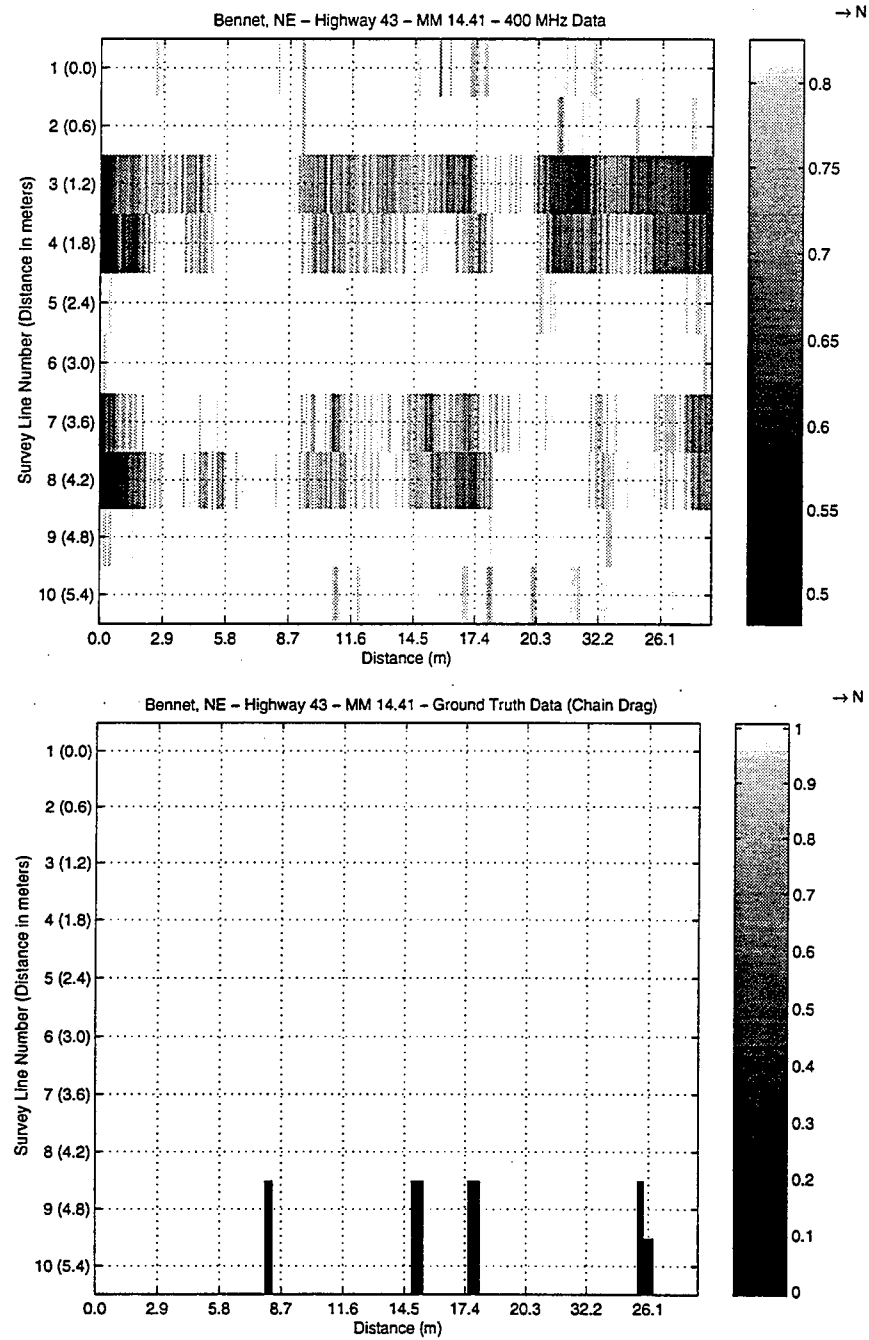


Figure 7.13: 2-D plot representing deterioration areas of the mile marker 14.41 (Highway 43) bridge according to the 400 MHz data. The bottom figure is the ground truth data and is provided for reference.

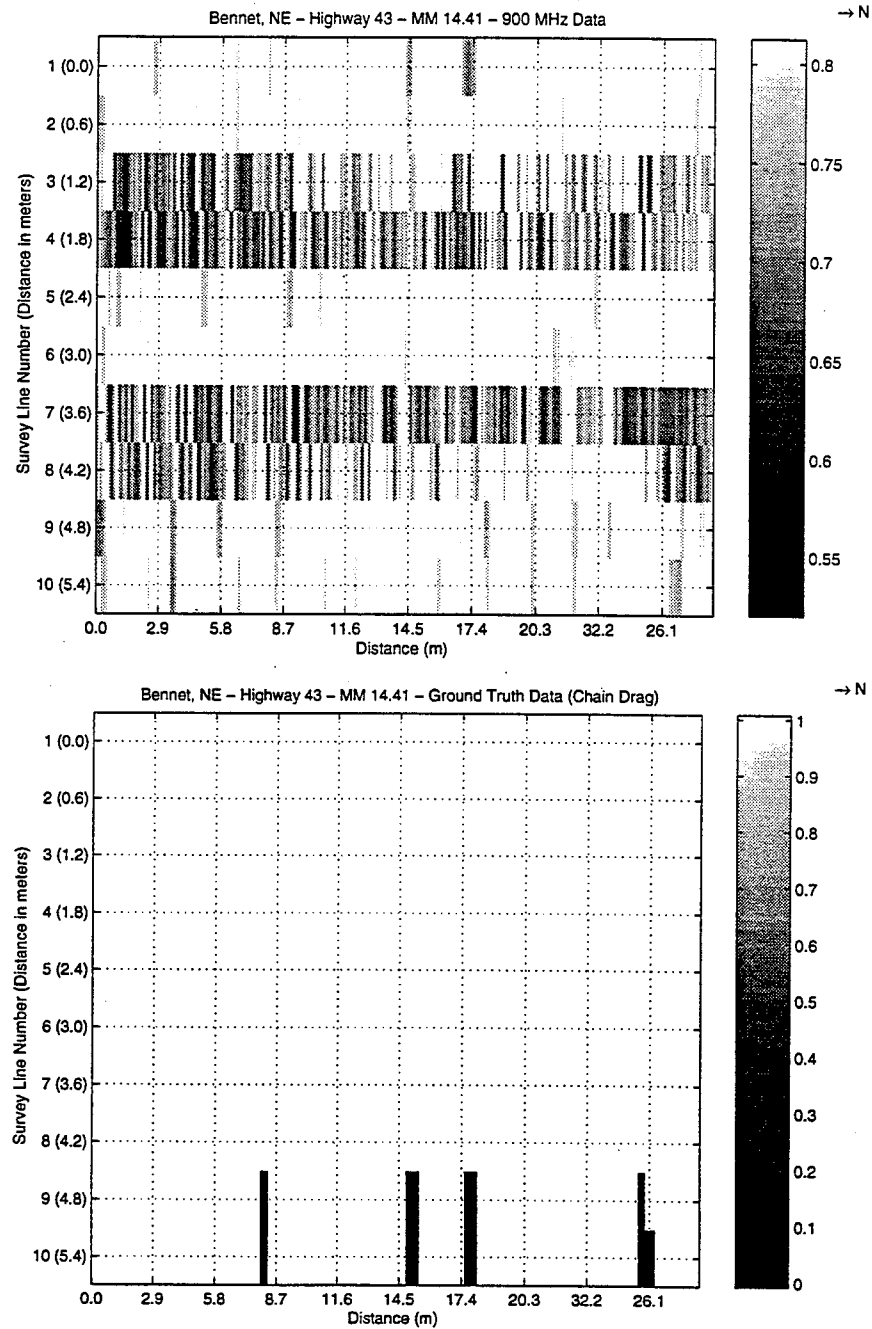


Figure 7.14: 2-D plot representing deterioration areas of the mile marker 14.41 (Highway 43) bridge according to the 900 MHz data. The bottom figure is the ground truth data and is provided for reference.

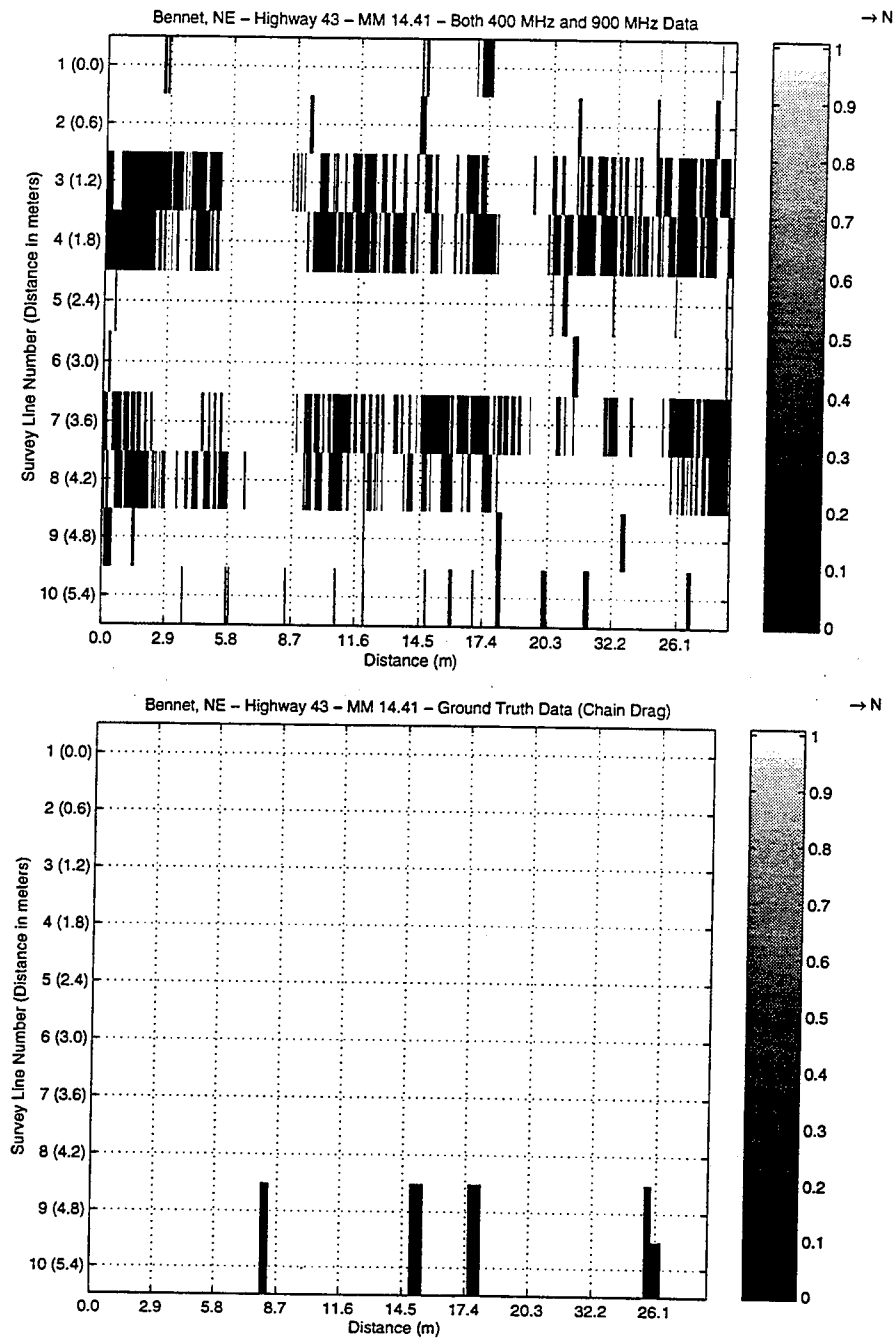


Figure 7.15: 2-D plot representing deterioration areas common to both the 400 and 900 MHz data for the bridge at mile marker 14.41 (Highway 43). The bottom figure is the ground truth data and is provided for reference.

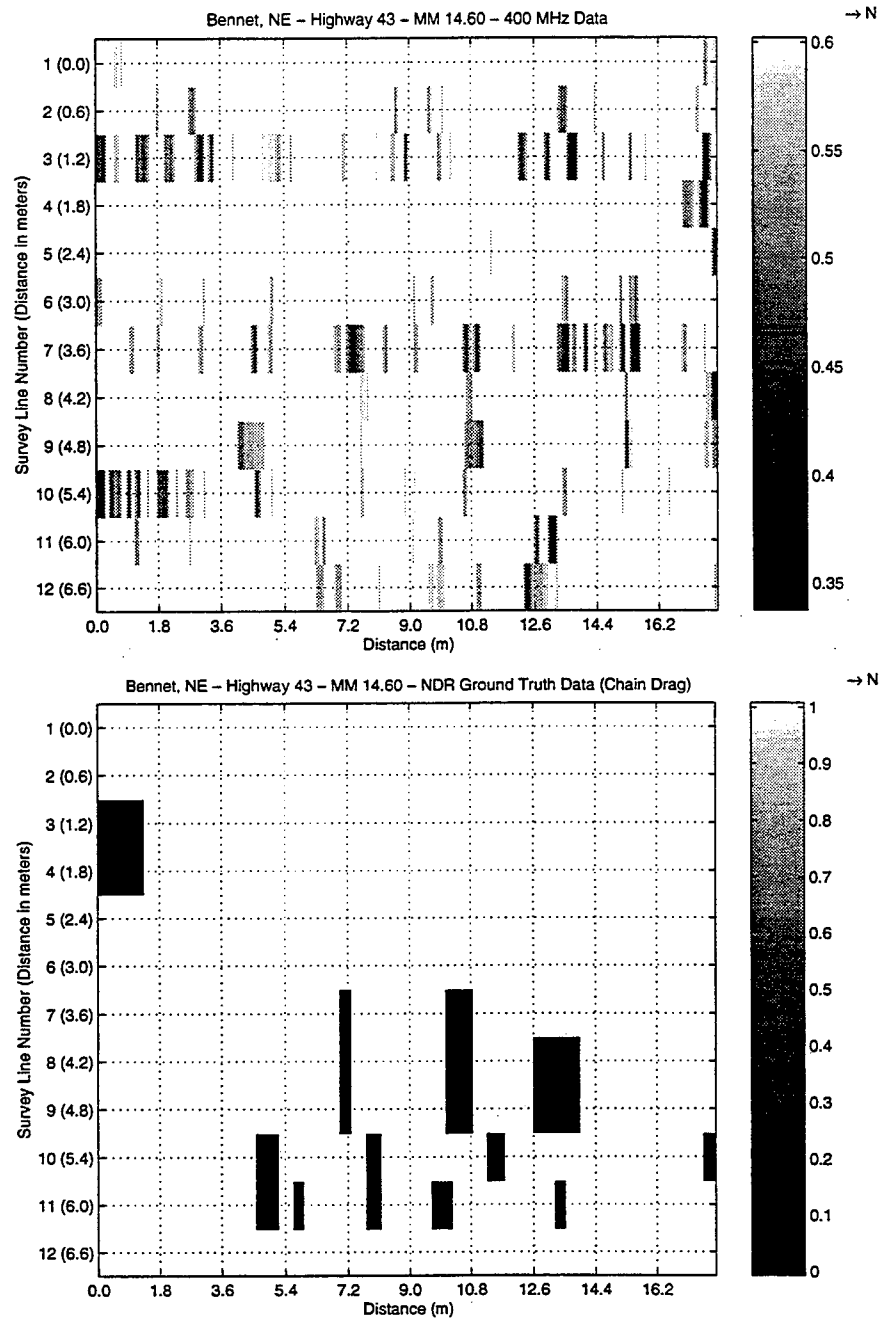


Figure 7.16: 2-D plot representing deterioration areas of the mile marker 14.60 (Highway 43) bridge according to the 400 MHz data. The bottom figure is the ground truth data and is provided for reference.

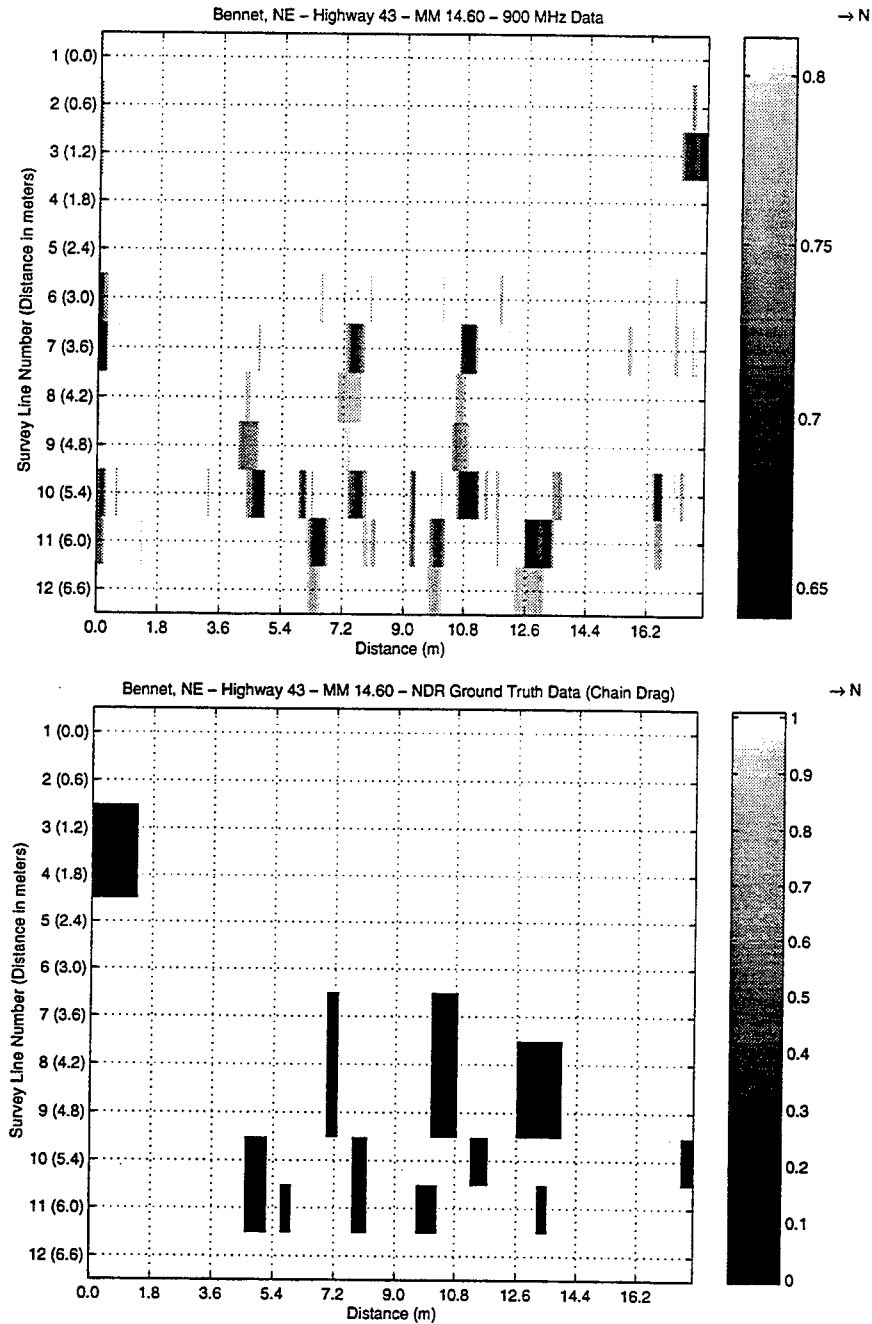


Figure 7.17: 2-D plot representing deterioration areas of the mile marker 14.60 (Highway 43) bridge according to the 900 MHz data. The bottom figure is the ground truth data and is provided for reference.

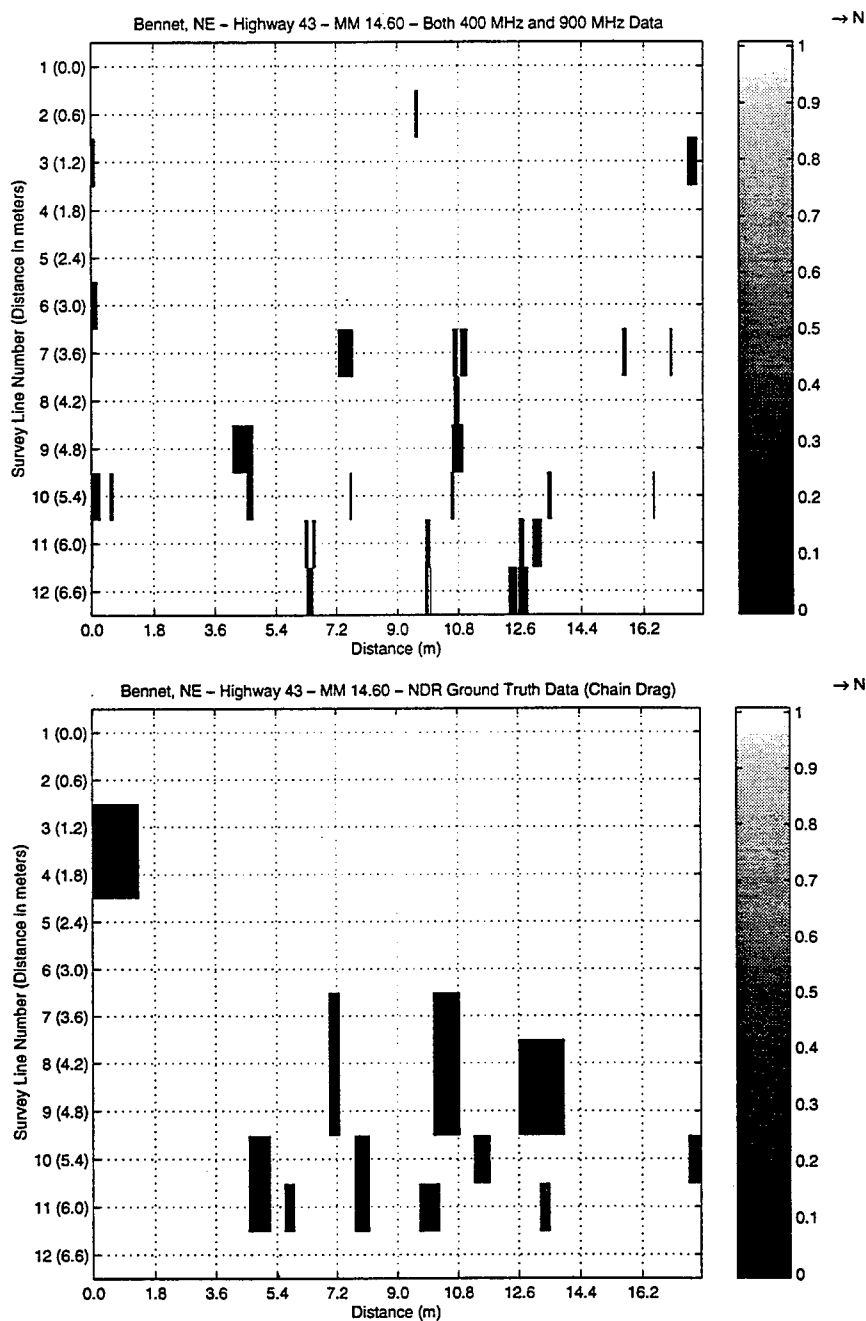


Figure 7.18: 2-D plot representing deterioration areas common to both the 400 and 900 MHz data for the bridge at mile marker 14.60 (Highway 43). The bottom figure is the ground truth data and is provided for reference.

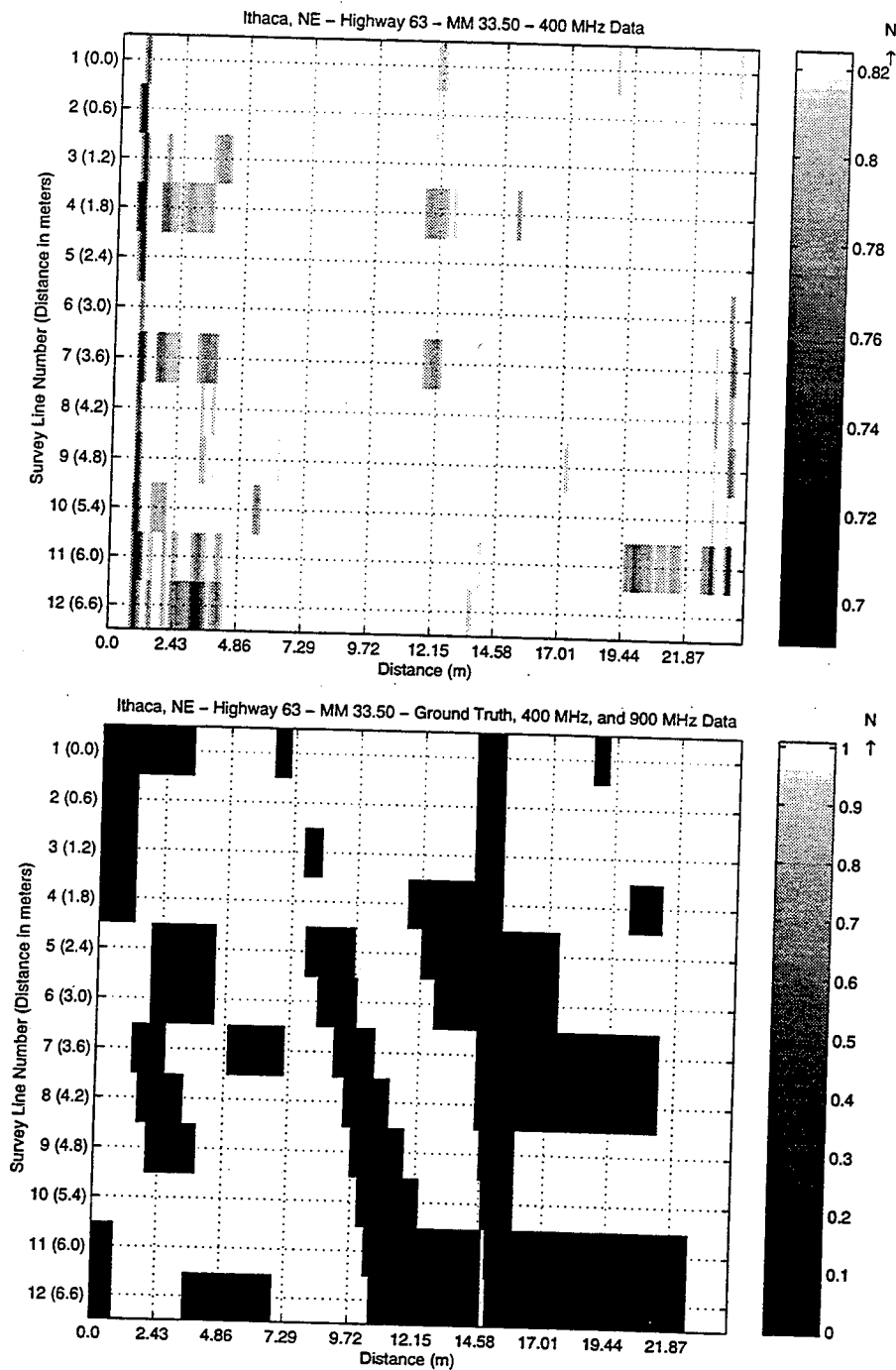


Figure 7.19: 2-D plot representing deterioration areas of the mile marker 33.50 (Highway 63) bridge according to the 400 MHz data. The bottom figure is the ground truth data and is provided for reference.

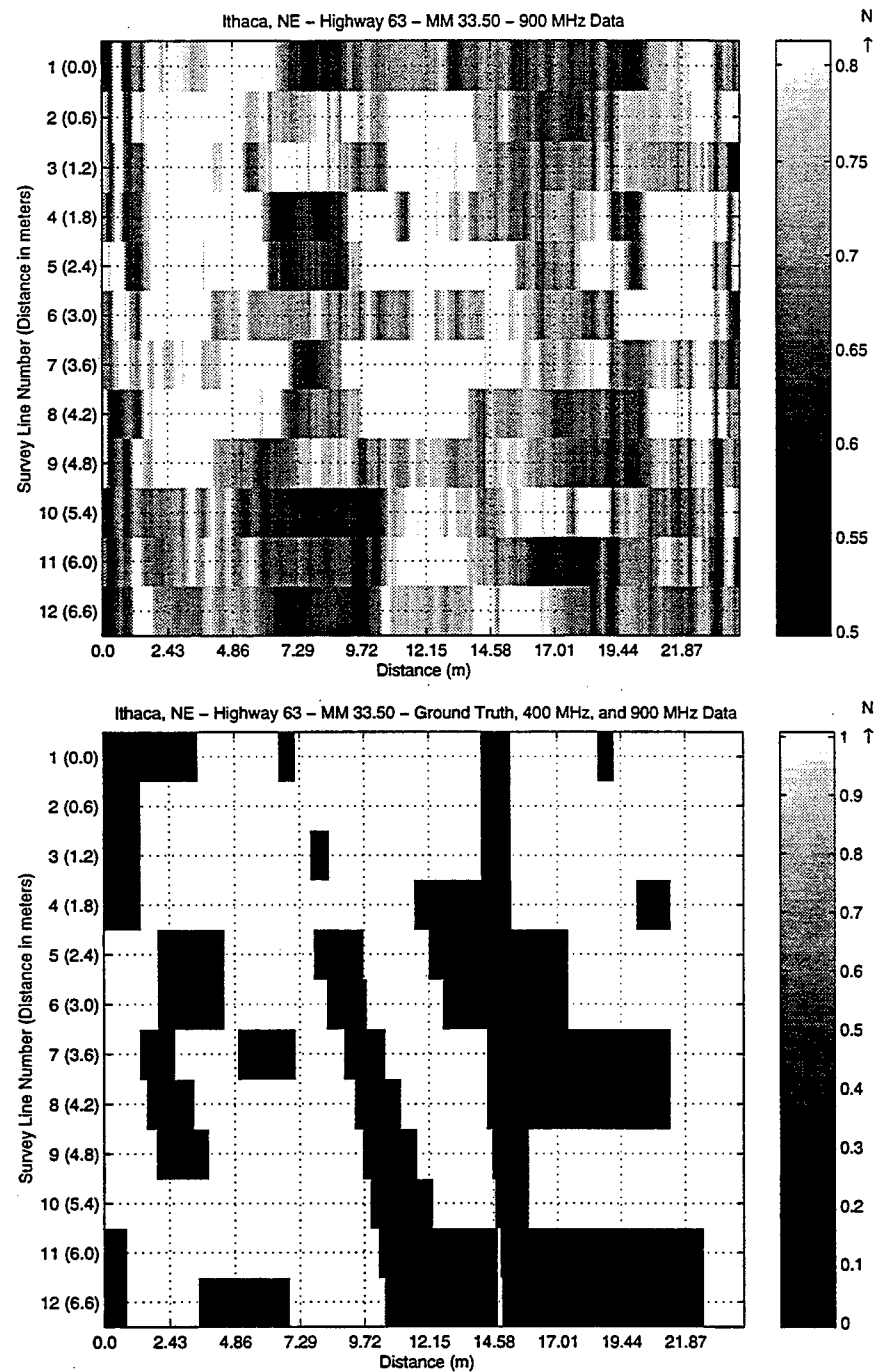


Figure 7.20: 2-D plot representing deterioration areas of the mile marker 33.50 (Highway 63) bridge according to the 900 MHz data. The bottom figure is the ground truth data and is provided for reference.

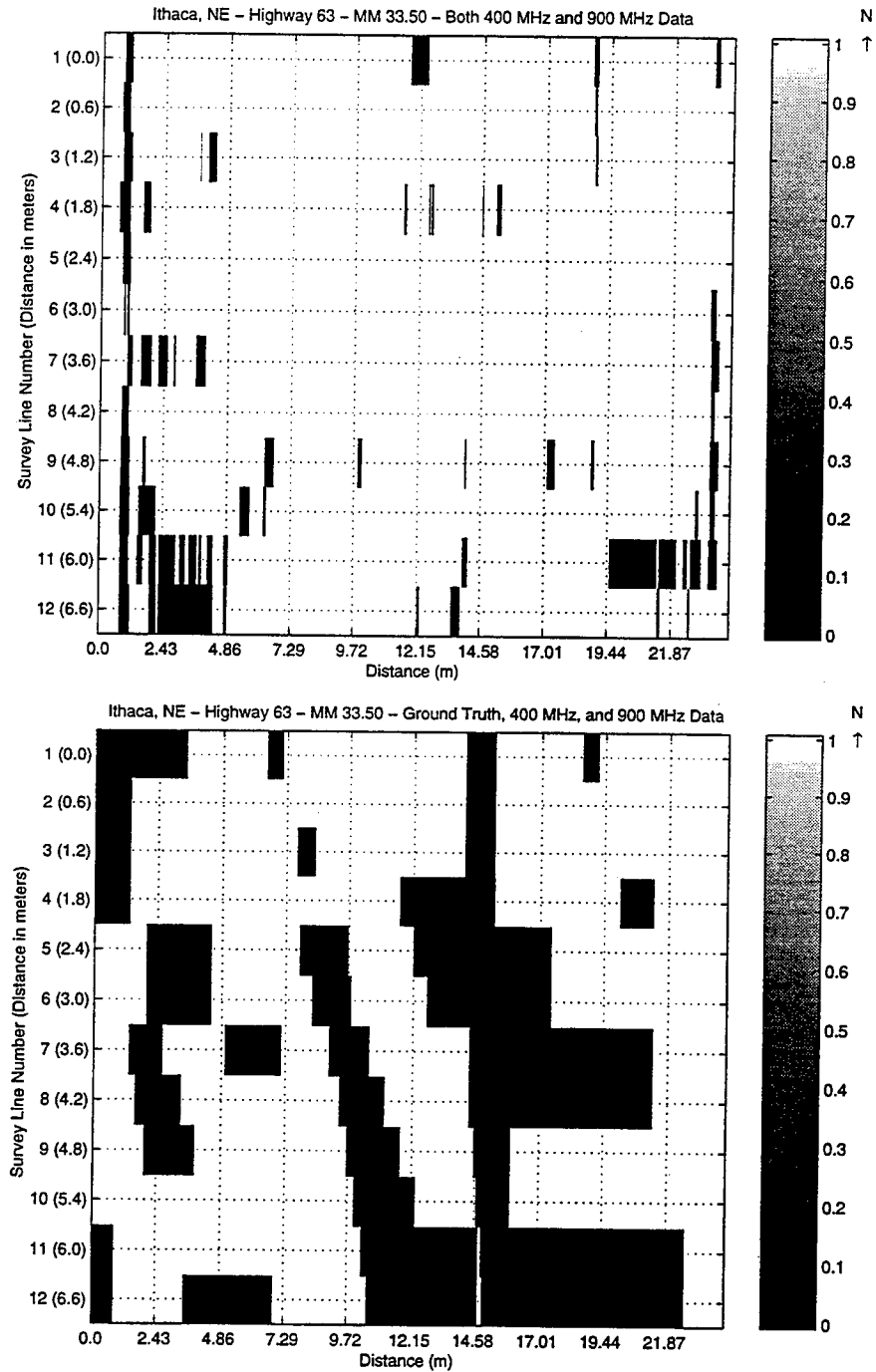


Figure 7.21: 2-D plot representing deterioration areas common to both the 400 and 900 MHz data for the bridge at mile marker 33.50 (Highway 63). The bottom figure is the ground truth data and is provided for reference.

7.3.4 Comparison of Experimental 400 MHz Data With Ground Truth Data

Results of comparisons made between the experimental 400 MHz data and the NDR ground truth (GT) data are summarized in Table 7.4. The third column represents the amount of bridge deck determined deteriorated from the ground truth data. The fourth column gives the percentage of bridge deck determined deteriorated from intersections of the experimental data with the ground truth data, and the last column gives an indication of how well the experimental data matched with the ground truth data relative to the ground truth data. Figures 7.22, 7.23, and 7.24 show the plots corresponding to the information given in the last column for the mile marker 14.41, 14.60, and 33.50 bridges, respectively.

The match between the two data sets were high for three of the Ithaca bridges. Since the experimental data showed a high percentage of deterioration, the chances for a match were much better. Visual comparisons of the 2-D plots suggest that the experimental data for the Bennet bridges were actually a much better match to the ground truth data than the Ithaca bridges. The Ithaca bridges have a different construction and much wider rebar spacing than the bridges at Bennet.

7.3.5 Comparison of Experimental 900 MHz Data With Ground Truth Data

Results of comparisons made between the experimental 900 MHz data and the NDR ground truth (GT) data are summarized in Table 7.5. The information is presented in the same manner as in Table 7.4. Corresponding plots for the three bridges of focus are given in Figures 7.25, 7.26, and 7.27.

Again, the match between the data sets seemed to be high for the Ithaca bridges. Visual comparisons of the 2-D plots revealed once again that the Bennet bridge data were better matches to the ground truth data than the data for the Ithaca bridges.

Table 7.4: Comparison of Experimental 400 MHz Data With Ground Truth (GT) Data

Bridge Information		Results		
Highway/Street Nearest Town	Mile Marker	GT % Det.	GT and 400 MHz % Det.	400 MHz Relative to GT % Match
HW 63 Ithaca, NE	33.50	33.43	3.26	9.75
HW 63 Ithaca, NE	34.87	18.99	13.40	70.56
HW 63 Ithaca, NE	37.20	30.77	26.76	86.97
HW 63 Ithaca, NE	32.95	30.34	13.33	43.94
HW 43 Bennet, NE	14.41	1.49	0.18	12.08
HW 43 Bennet, NE	14.60	6.06	0.81	13.37

Table 7.5: Comparison of Experimental 900 MHz Data With Ground Truth (GT) Data

Bridge Information		Results		
Highway/Street Nearest Town	Mile Marker	GT % Det.	GT and 900 MHz % Det.	900 MHz Relative to GT % Match
HW 63 Ithaca, NE	33.50	33.43	23.18	69.34
HW 63 Ithaca, NE	34.87	18.99	11.35	59.77
HW 63 Ithaca, NE	37.20	30.77	24.51	79.66
HW 63 Ithaca, NE	32.95	30.34	21.93	72.28
HW 43 Bennet, NE	14.41	1.49	0.19	12.75
HW 43 Bennet, NE	14.60	6.06	1.61	26.57

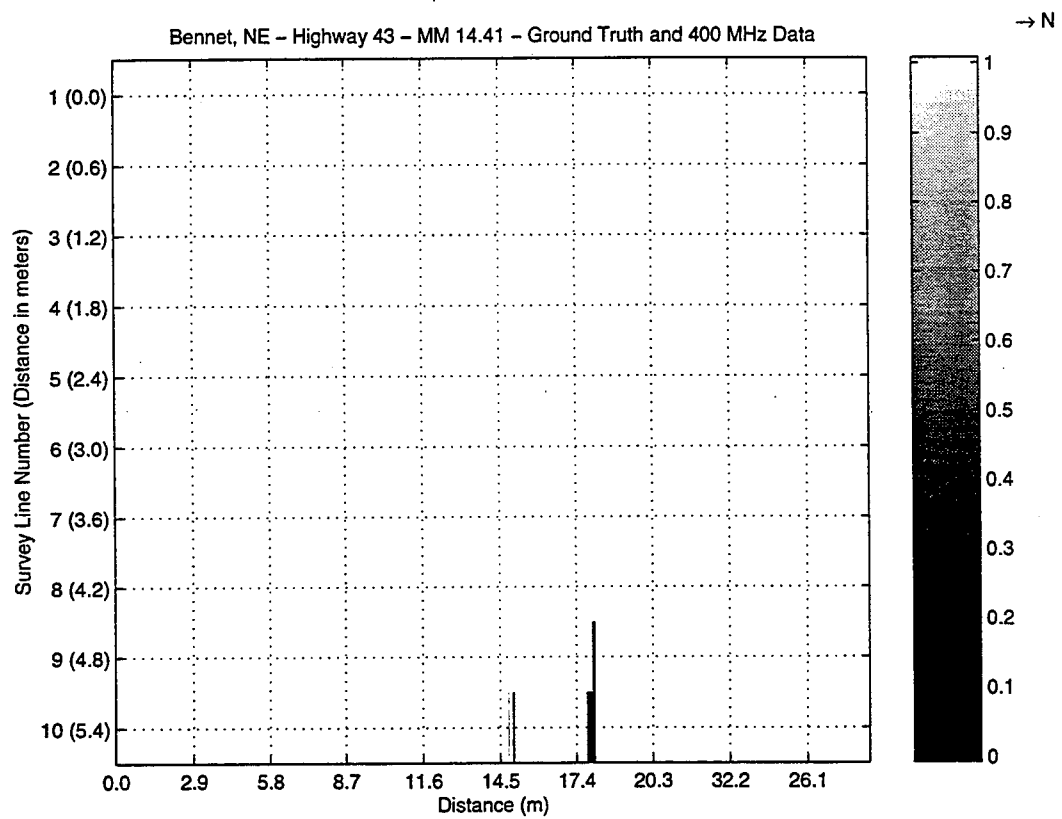


Figure 7.22: 2-D plot representing deterioration areas common to both the 400 MHz and ground truth data for the bridge located at mile marker 14.41 (Highway 43).

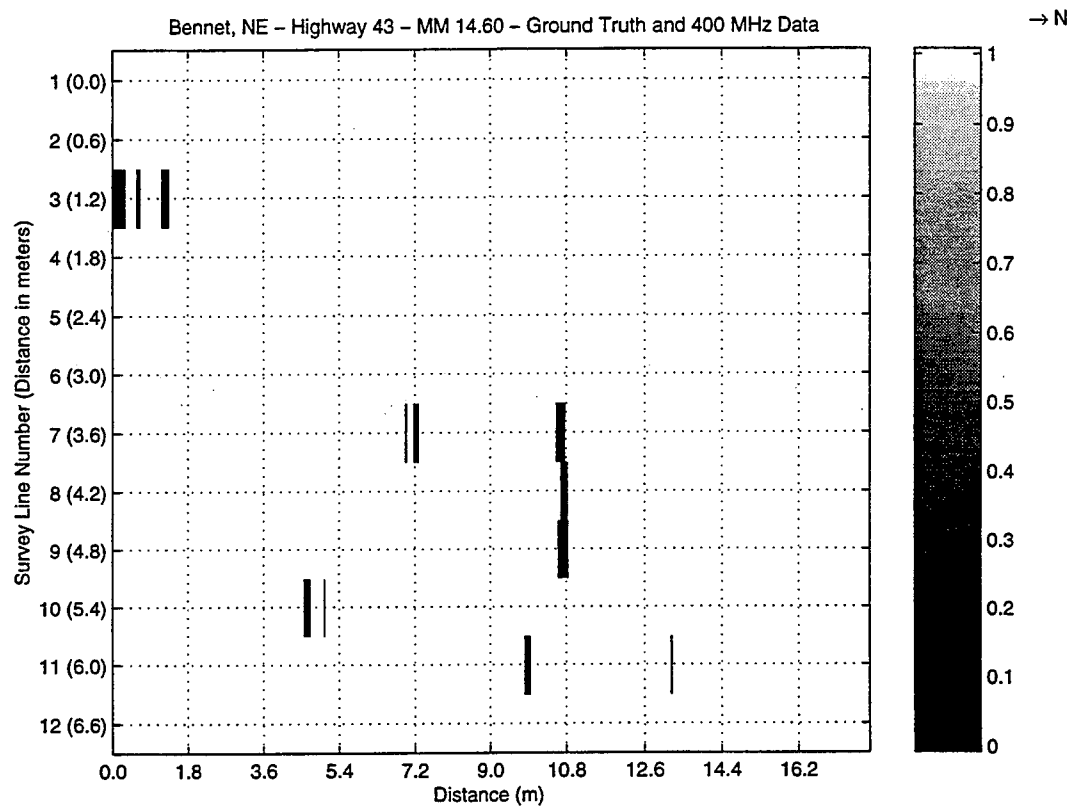


Figure 7.23: 2-D plot representing deterioration areas common to both the 400 MHz and ground truth data for the bridge located at mile marker 14.60 (Highway 43).

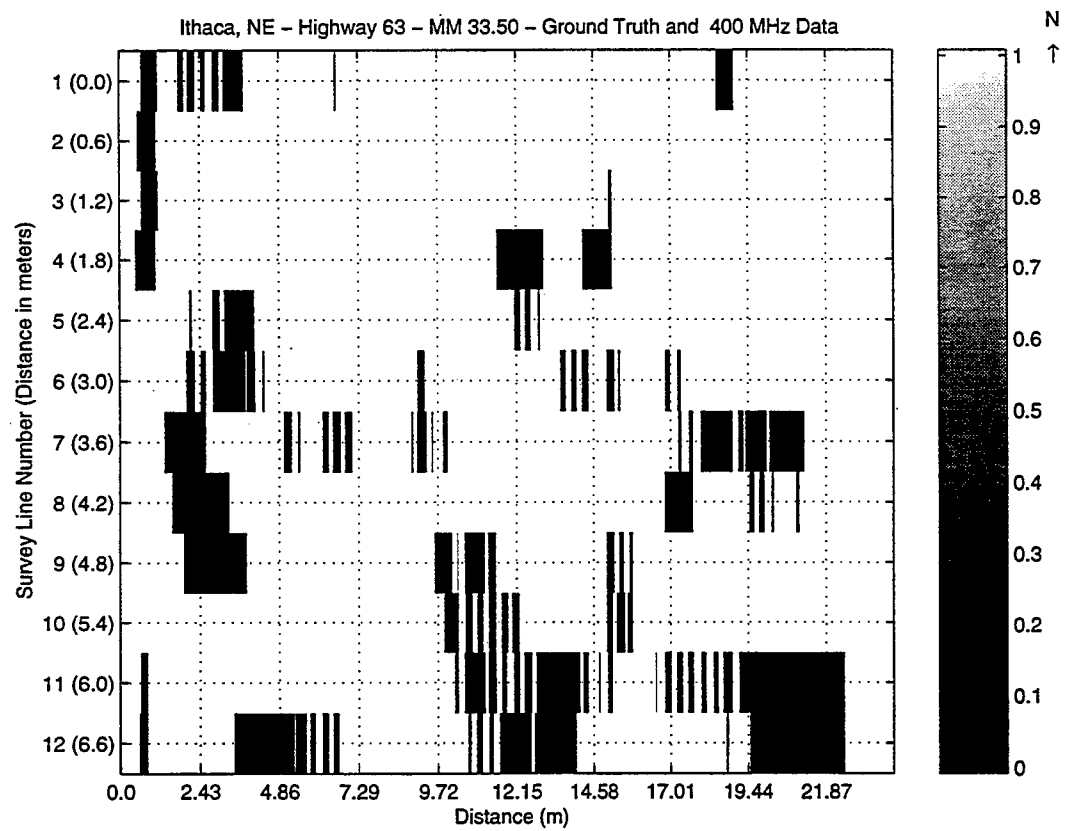


Figure 7.24: 2-D plot representing deterioration areas common to both the 400 MHz and ground truth data for the bridge located at mile marker 33.50 (Highway 63):

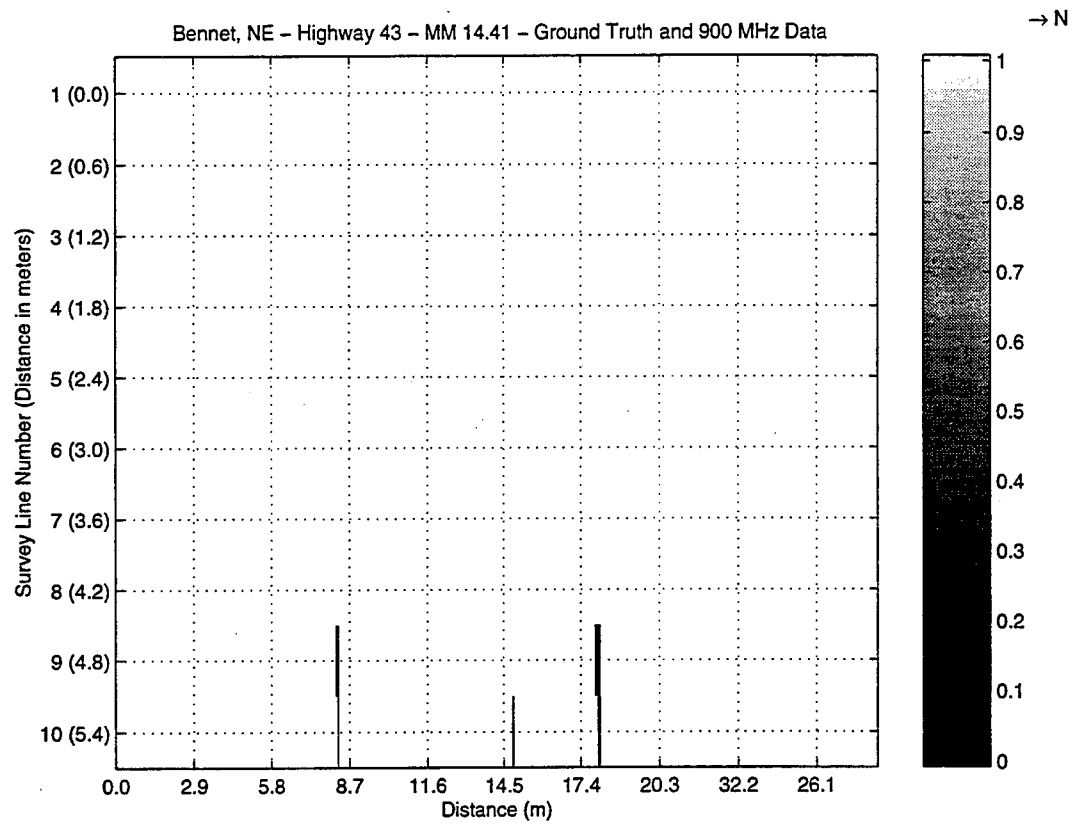


Figure 7.25: 2-D plot representing deterioration areas common to both the 900 MHz and ground truth data for the bridge located at mile marker 14.41 (Highway 43).

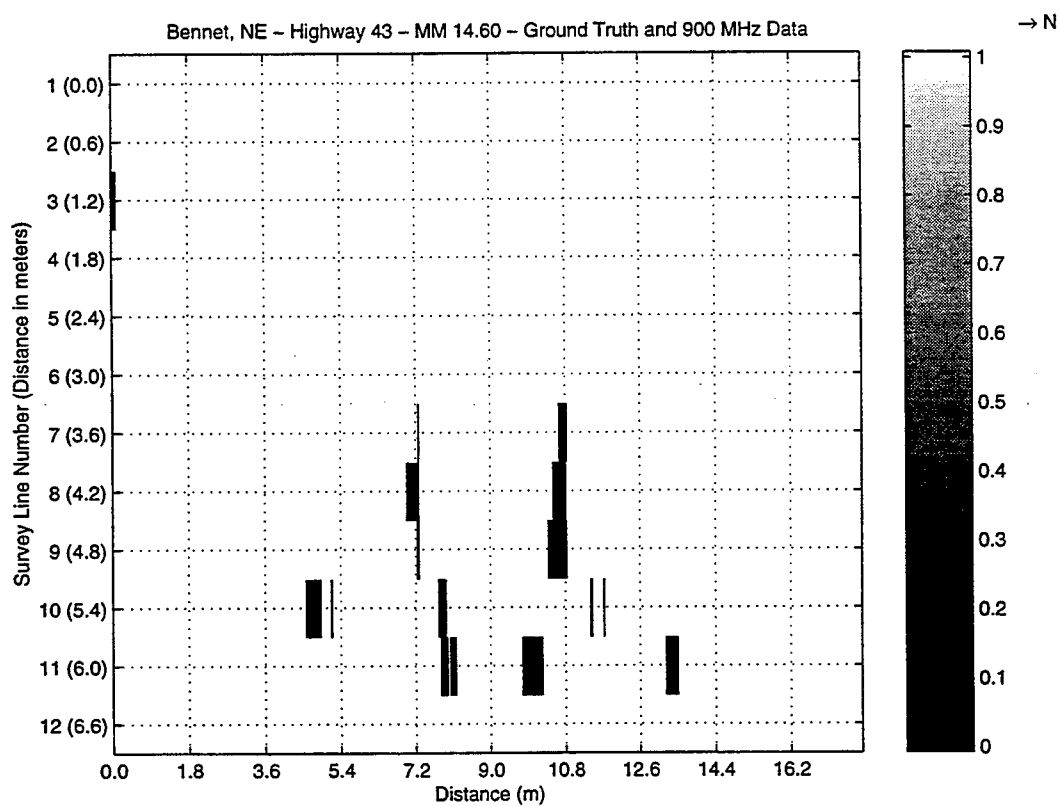


Figure 7.26: 2-D plot representing deterioration areas common to both the 900 MHz and ground truth data for the bridge located at mile marker 14.60 (Highway 43).

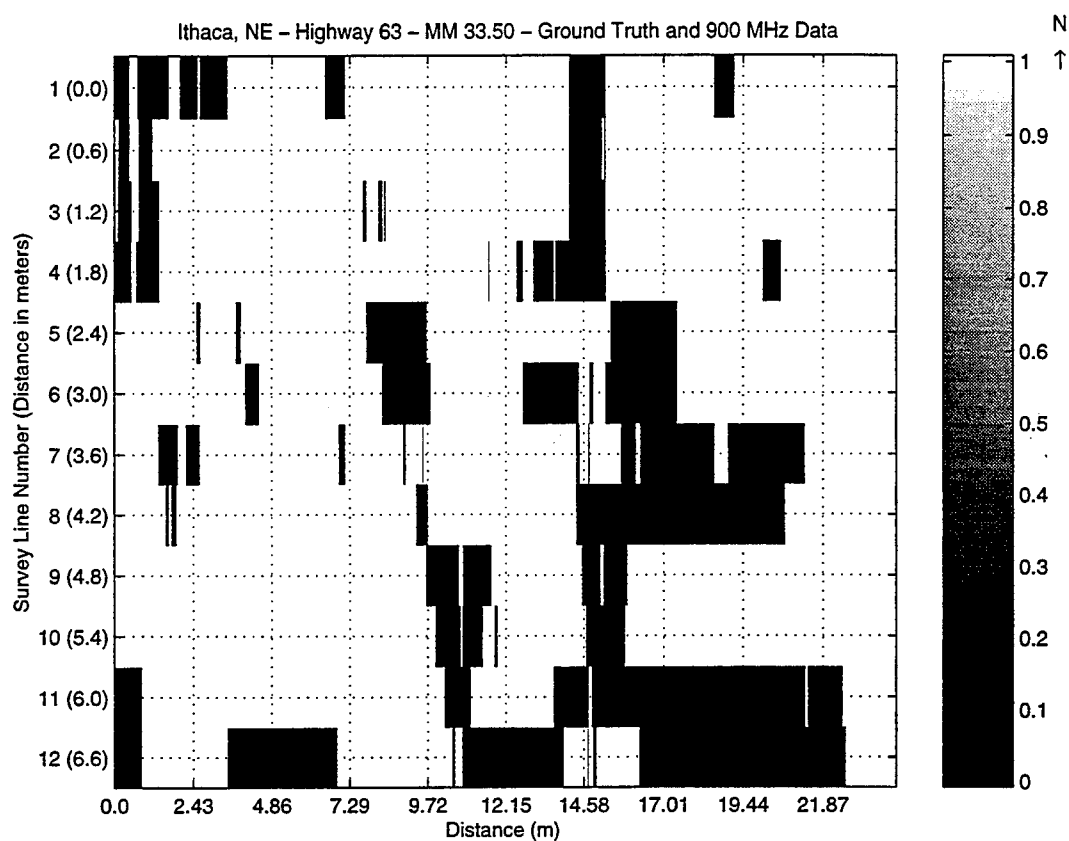


Figure 7.27: 2-D plot representing deterioration areas common to both the 900 MHz and ground truth data for the bridge located at mile marker 33.50 (Highway 63).

Table 7.6: Comparison of Experimental 400 and 900 MHz Data With Ground Truth (GT) Data

Bridge Information		Results		
Highway/Street Nearest Town	Mile Marker	GT % Det.	GT, 400, and 900 MHz % Det.	400 and 900 MHz Relative to GT % Match
HW 63 Ithaca, NE	33.50	33.43	2.48	7.42
HW 63 Ithaca, NE	34.87	18.99	7.97	41.97
HW 63 Ithaca, NE	37.20	30.77	20.37	66.20
HW 63 Ithaca, NE	32.95	30.34	8.39	27.65
HW 43 Bennet, NE	14.41	1.49	0.08	5.37
HW 43 Bennet, NE	14.60	6.06	0.48	7.92

7.3.6 Comparison of Experimental 400 and 900 MHz Data With Ground Truth Data

Results of comparisons made between all three data sets (the experimental 400 MHz data, 900 MHz data, and the NDR ground truth (GT) data) are summarized in Table 7.6. The information given in this table represents areas where the intersection of the 400 MHz and 900 MHz data sets intersects with the ground truth data set. In other words, it represents the percentage of deterioration agreed upon by all three data sets. Corresponding 2-D plots are given in Figures 7.28, 7.29, and 7.30 for the three chosen bridges.

The same general trend seen in the two previous comparisons were also seen here.

7.3.7 General Observations Using Constant Threshold Level Method

Using the threshold levels found from analysis of the the model bridge deck, the percentage of deterioration seemed to be grossly overestimated for all of the bridges, indicating a threshold

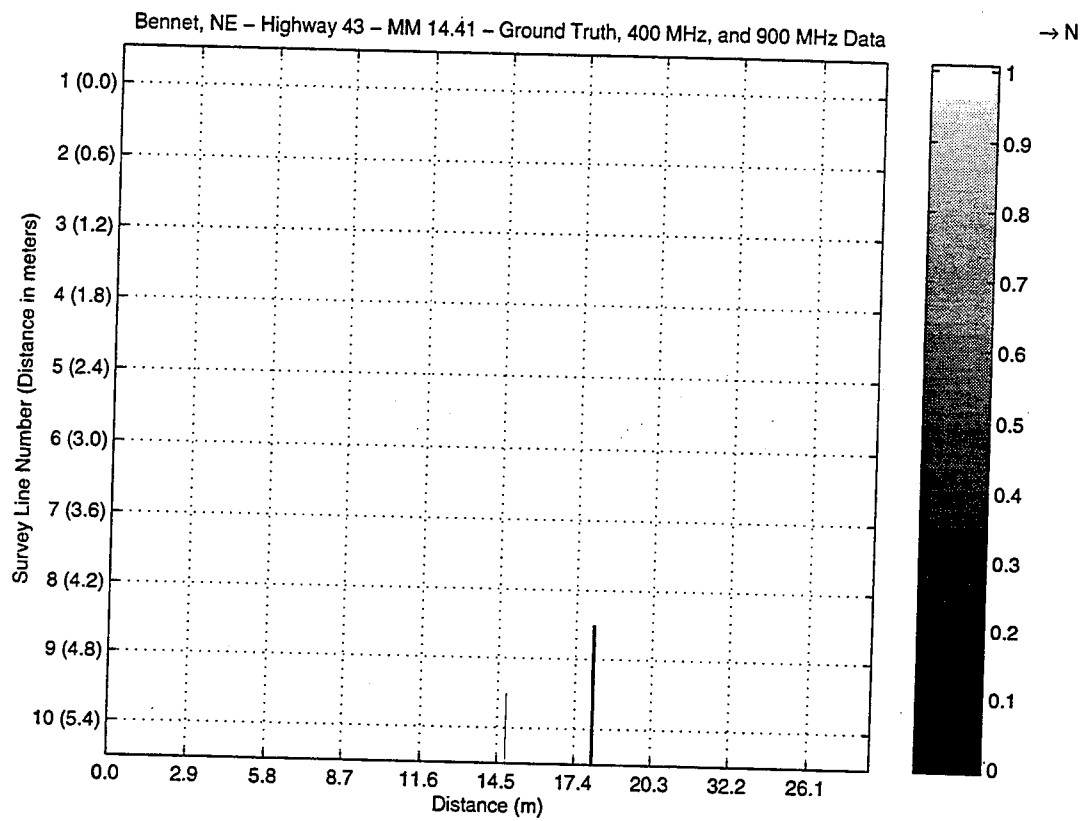


Figure 7.28: 2-D plot representing deterioration areas common to all three data sets for the bridge located at mile marker 14.41 (Highway 43).

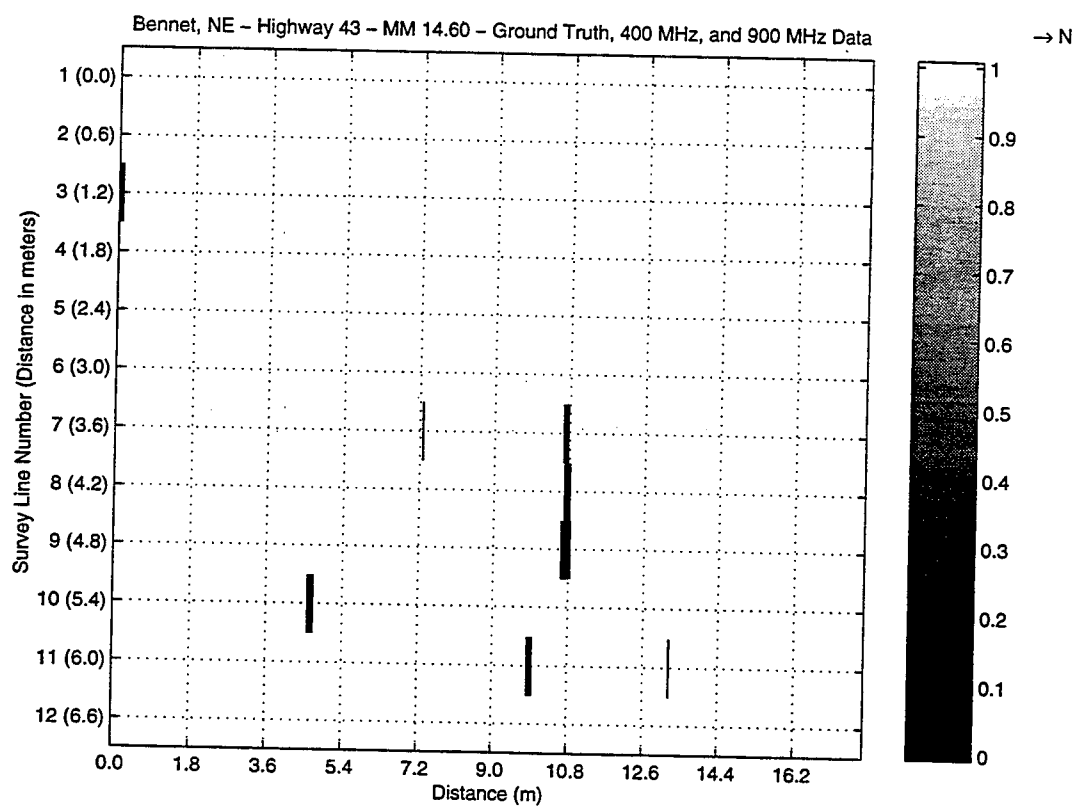


Figure 7.29: 2-D plot representing deterioration areas common to all three data sets for the bridge located at mile marker 14.60 (Highway 43).

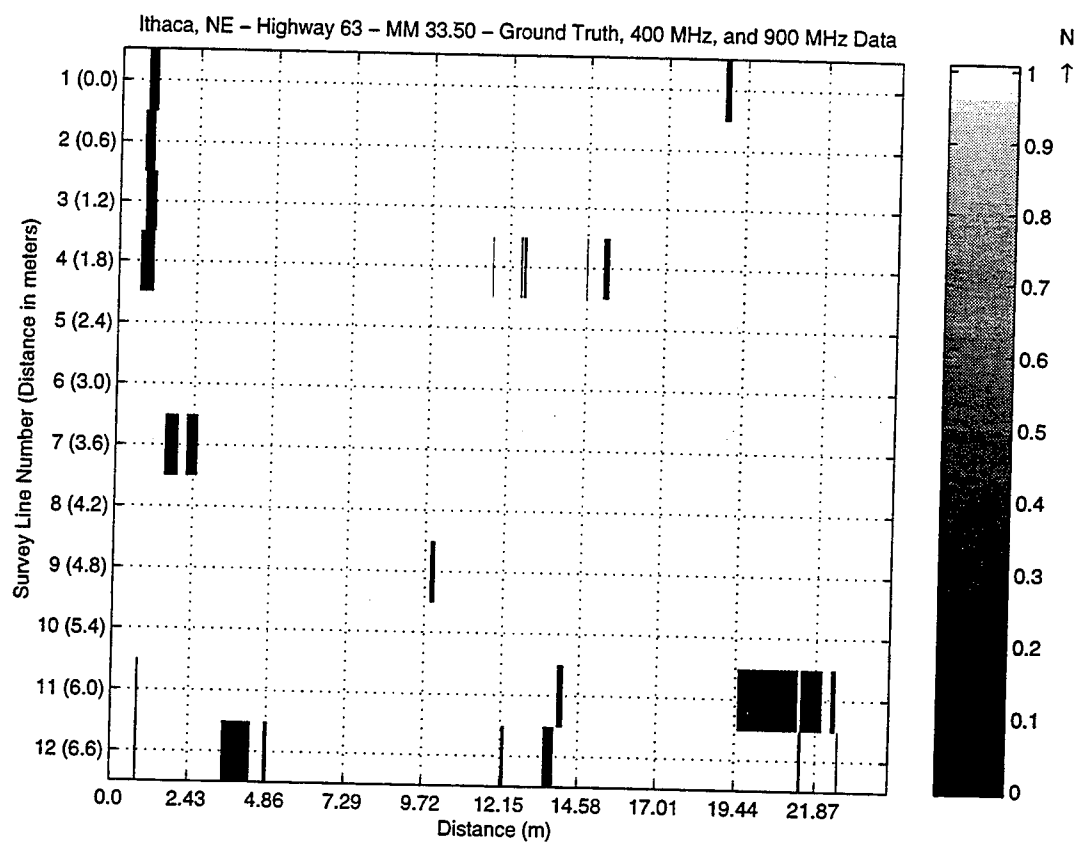


Figure 7.30: 2-D plot representing deterioration areas common to all three data sets for the bridge located at mile marker 33.50 (Highway 63).

level which was too high. Visual inspections of the 2-D plots suggest that the bridge decks with rebars spaced of 30.48 cm (12 in) and within 5 cm (2 in) of the deck surface seemed to match best with the ground truth data; the two Bennet bridges, the Adams Street Bridge, and the bridge on North 38th Street (East Campus) fell into this category. The other bridges had much wider rebar spacings and rebars located approximately 7 cm (3 in) below the surface. The model bridge deck had rebars with a spacing of 20.32 cm (8 in) and were covered with approximately 5 cm of concrete. From these observations, it seems that the threshold level will vary depending on the rebar layout of the bridge under investigation. It is believed that a lower threshold level would have been found for the bridges with the wider rebar spacing and thicker concrete cover if the model bridge deck more closely exhibited the characteristics of those bridges. Also, an asphalt overlay seemed to greatly affect the results.

Another factor affecting the results is the estimate of the technician performing the chain drag survey as to where the actual delaminated areas are located. If an the area is shifted by as little as one centimeter from the actual position on the 2-D plot, the results can change dramatically. Therefore, it is recommended that visual comparisons of the 2-D plots be used rather than the numbers listed in the tables when determining the amount of correlation between the data sets.

The string of rebars chosen by the algorithms as exhibiting the best mean variance used for normalization were also recorded. None of the rebars chosen by the 400 MHz algorithms matched with the rebars chosen by the 900 MHz algorithms for any of the bridges. This suggests that the choice of frequency did matter in this case. It is believed that the highest frequency possible should be used in order to better separate the surface and rebar returns.

7.4 Varying Threshold Level (VTL) Method

A second method, termed the Varying Threshold Level method, is briefly discussed here in which the threshold level is varied until the percentage of deterioration given by the

experimental data equals that given by the ground truth data. Of course, this method can only be used when ground truth data is available. All other parameters of the Constant Threshold Level method remain the same. Table 7.7 lists the threshold levels necessary to achieve the same level of deterioration as the ground truth data for the six bridges which had available ground truth data. Tables 7.8 through 7.11 list information similar to that given in Tables 7.3 through 7.6. 2-D plots of the experimental 400 and 900 MHz data for all six bridges are given in Figures 7.31 through 7.39.

7.4.1 General Observations Using Varying Threshold Level Method

As seen in Table 7.7, the threshold levels were different for each bridge and for each frequency. However, the threshold level for the 400 MHz data was nearly equal to the threshold level for the 900 MHz data for the three bridges located at mile markers 34.87, 37.20, and 14.41. It was also noted that the percentage of deterioration was very sensitive to the threshold level in certain ranges, often doubling with an addition of only 0.01 or 0.02 to the threshold level.

Visual inspections of the 2-D plots (Figures 7.31 through 7.39) suggest that the deterioration areas found using the Varying Threshold Level method were probably more realistic than those found using the Constant Threshold Level method. Although more research needs to be done, it is believed that data obtained using GPR are more accurate than that of the chain drag. Therefore, the optimum threshold levels probably lie just above those chosen for the Varying Threshold Level method. Observations of Tables 7.8 through 7.11 indicate that the experimental data compared fairly well with the ground truth data. The numbers were somewhat low, however. As noted in the Constant Threshold Level method section, the percentage of match between the experimental and ground truth data sets depends upon many factors, including the accuracy of the deterioration area locations according to the ground truth data. As before, it is suggested that visual comparisons of

Table 7.7: Threshold Levels Necessary to Match Ground Truth Data

Bridge Information		Threshold Levels	
Highway/Street Nearest Town	Mile Marker	400 MHz Threshold	900 MHz Threshold
HW 63 Ithaca, NE	33.50	0.8704	0.7050
HW 63 Ithaca, NE	34.87	0.7271	0.7380
HW 63 Ithaca, NE	37.20	0.6825	0.6628
HW 63 Ithaca, NE	32.95	0.8101	0.7233
HW 43 Bennet, NE	14.41	0.7600	0.7280
HW 43 Bennet, NE	14.60	0.5545	0.7927

the 2-D plots be used to judge the amount of correlation rather than the numbers listed in the tables. The Ithaca bridge data seem to match better than the Bennet bridge data. However, since the Ithaca bridges were more deteriorated than the Bennet bridges, the chances of matching the ground truth data were higher.

Table 7.8: Comparison of Experimental 400 and 900 MHz Data (VTL Method)

Bridge Information		Results	
Highway/Street Nearest Town	Mile Marker	GT % Det.	400 and 900 MHz % Det.
HW 63 Ithaca, NE	33.50	33.43	8.98
HW 63 Ithaca, NE	34.87	18.99	4.98
HW 63 Ithaca, NE	37.20	30.77	10.63
HW 63 Ithaca, NE	32.95	30.34	5.38
HW 43 Bennet, NE	14.41	1.49	0.09
HW 43 Bennet, NE	14.60	6.06	1.80

Table 7.9: Comparison of Experimental 400 MHz Data With Ground Truth (GT) Data (VTL Method)

Bridge Information		Results		
Highway/Street Nearest Town	Mile Marker	GT % Det.	GT and 400 MHz % Det.	400 MHz Relative to GT % Match
HW 63 Ithaca, NE	33.50	33.43	10.44	31.23
HW 63 Ithaca, NE	34.87	18.99	6.34	33.39
HW 63 Ithaca, NE	37.20	30.77	9.50	30.87
HW 63 Ithaca, NE	32.95	30.34	10.45	34.44
HW 43 Bennet, NE	14.41	1.49	0.05	3.36
HW 43 Bennet, NE	14.60	6.06	0.64	10.56

Table 7.10: Comparison of Experimental 900 MHz Data With Ground Truth (GT) Data (VTL Method)

Bridge Information		Results		
Highway/Street Nearest Town	Mile Marker	GT % Det.	GT and 900 MHz % Det.	900 MHz Relative to GT % Match
HW 63 Ithaca, NE	33.50	33.43	10.06	30.09
HW 63 Ithaca, NE	34.87	18.99	3.55	18.69
HW 63 Ithaca, NE	37.20	30.77	11.63	37.80
HW 63 Ithaca, NE	32.95	30.34	10.87	35.83
HW 43 Bennet, NE	14.41	1.49	0.00	0.00
HW 43 Bennet, NE	14.60	6.06	1.30	21.45

Table 7.11: Comparison of Experimental 400 and 900 MHz Data With Ground Truth (GT) Data (VTL Method)

Bridge Information		Results		
Highway/Street Nearest Town	Mile Marker	GT % Det.	GT, 400, and 900 MHz % Det.	400 and 900 MHz Relative to GT % Match
HW 63 Ithaca, NE	33.50	33.43	2.72	8.14
HW 63 Ithaca, NE	34.87	18.99	0.16	0.84
HW 63 Ithaca, NE	37.20	30.77	4.58	14.88
HW 63 Ithaca, NE	32.95	30.34	2.11	6.95
HW 43 Bennet, NE	14.41	1.49	0.00	0.00
HW 43 Bennet, NE	14.60	6.06	0.35	5.78

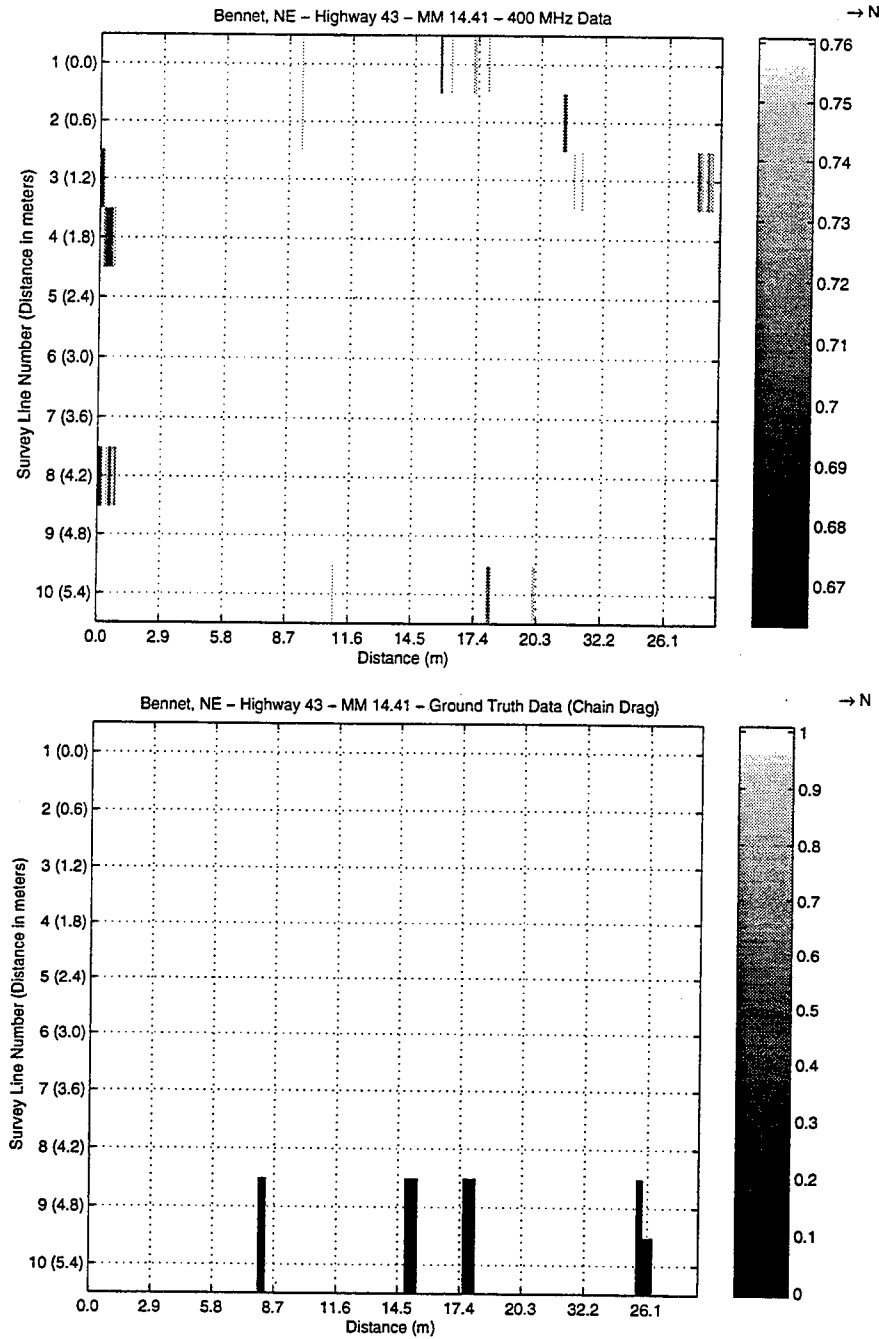


Figure 7.31: 2-D plot representing deterioration areas of the mile marker 14.41 (Highway 43) bridge according to the 400 MHz data (using VTL method). The bottom figure is the ground truth data and is provided for reference.

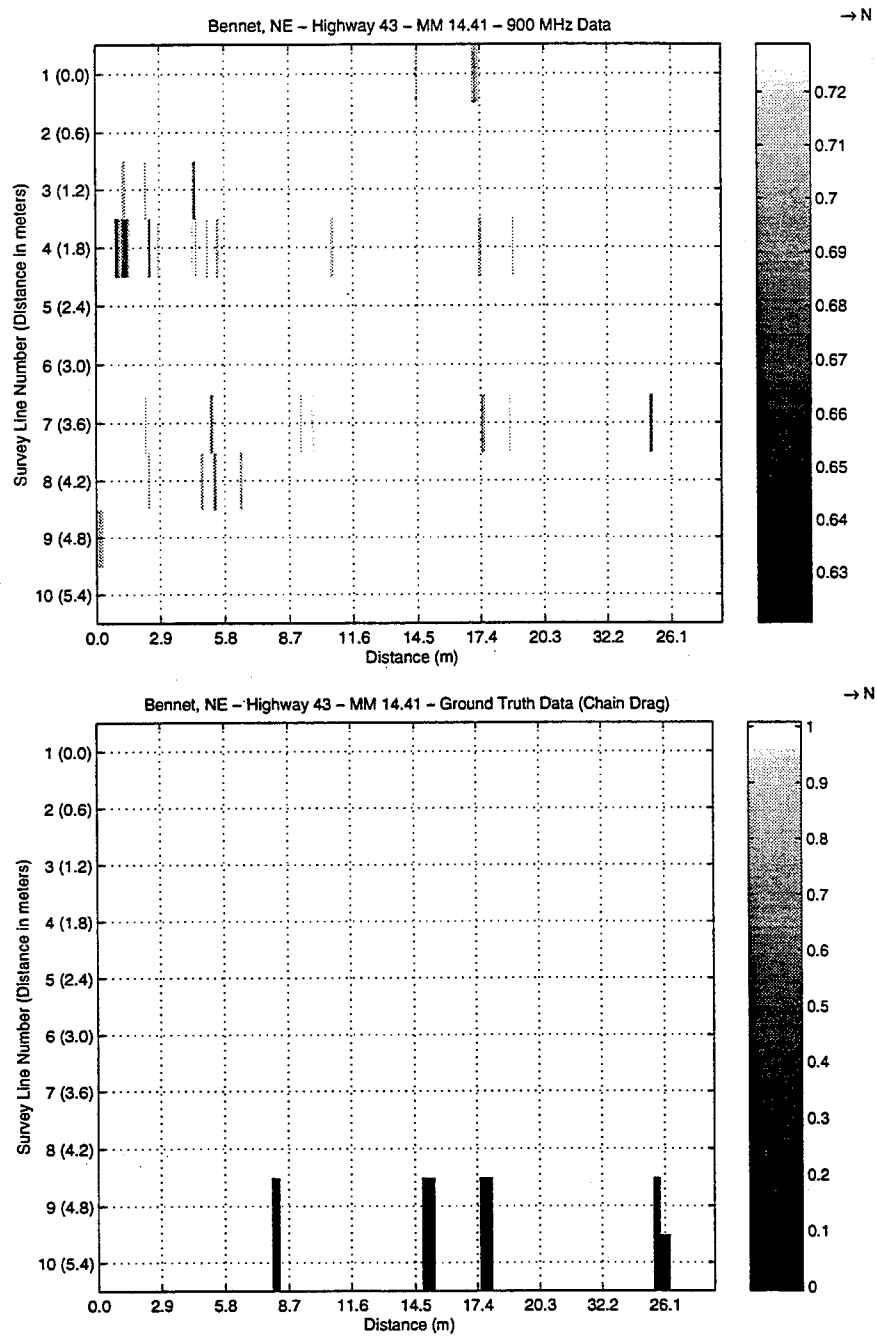


Figure 7.32: 2-D plot representing deterioration areas of the mile marker 14.41 (Highway 43) bridge according to the 900 MHz data (using VTL method). The bottom figure is the ground truth data and is provided for reference.

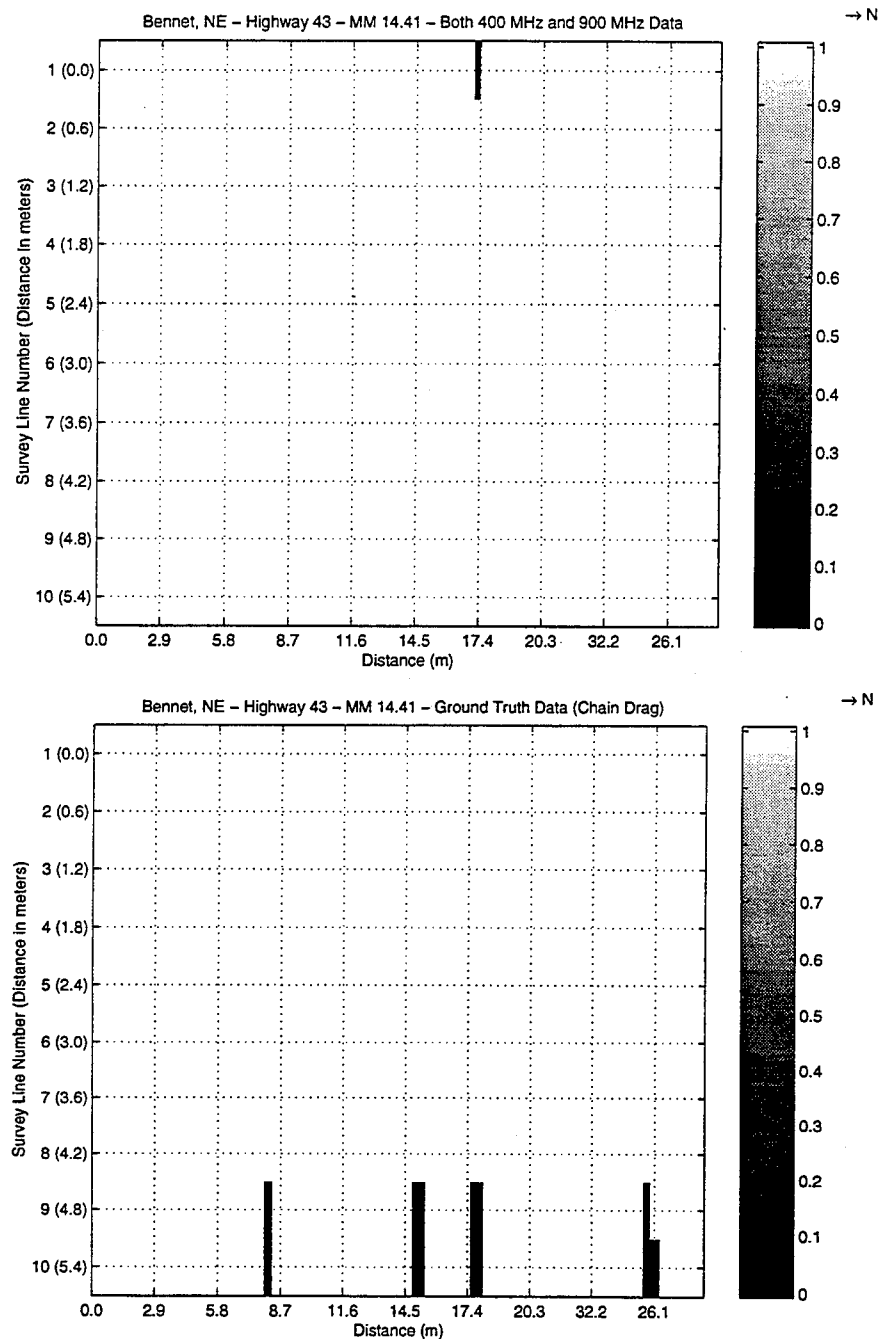


Figure 7.33: 2-D plot representing deterioration areas common to both the 400 and 900 MHz data for the bridge at mile marker 14.41 (Highway 43) (using VTL method). The bottom figure is the ground truth data and is provided for reference.

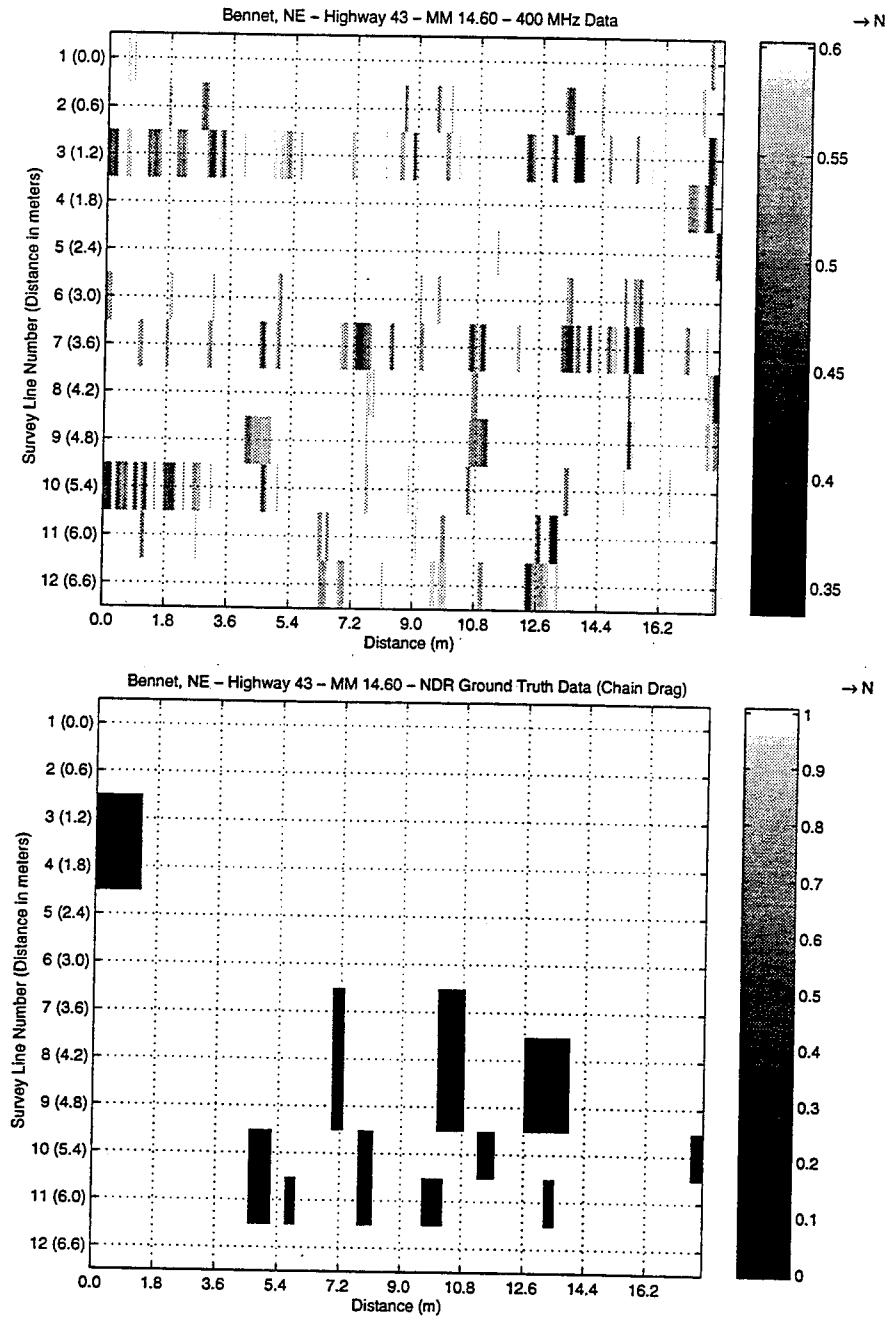


Figure 7.34: 2-D plot representing deterioration areas of the mile marker 14.60 (Highway 43) bridge according to the 400 MHz data (using VTL method). The bottom figure is the ground truth data and is provided for reference.

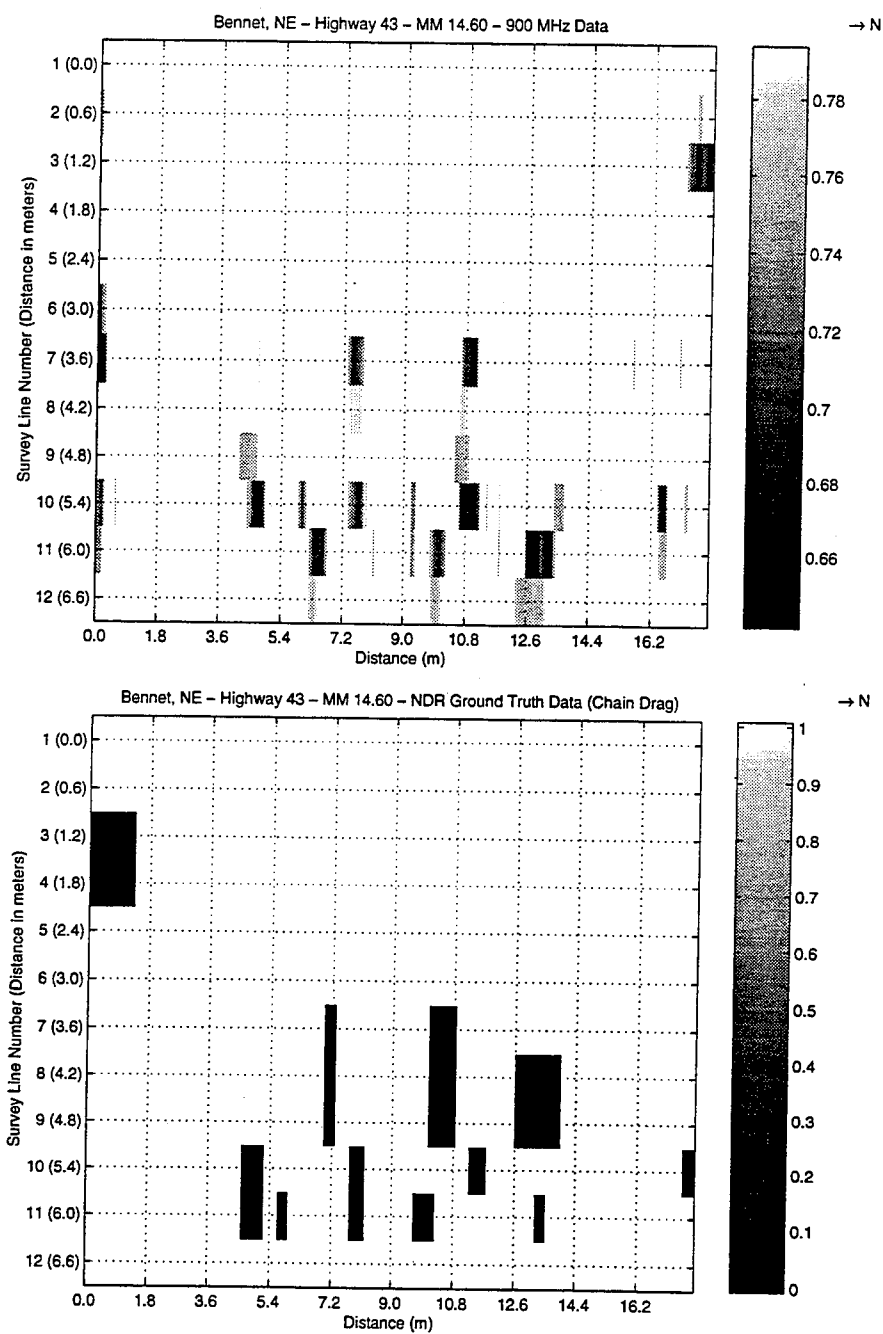


Figure 7.35: 2-D plot representing deterioration areas of the mile marker 14.60 (Highway 43) bridge according to the 900 MHz data (using VTL method). The bottom figure is the ground truth data and is provided for reference.

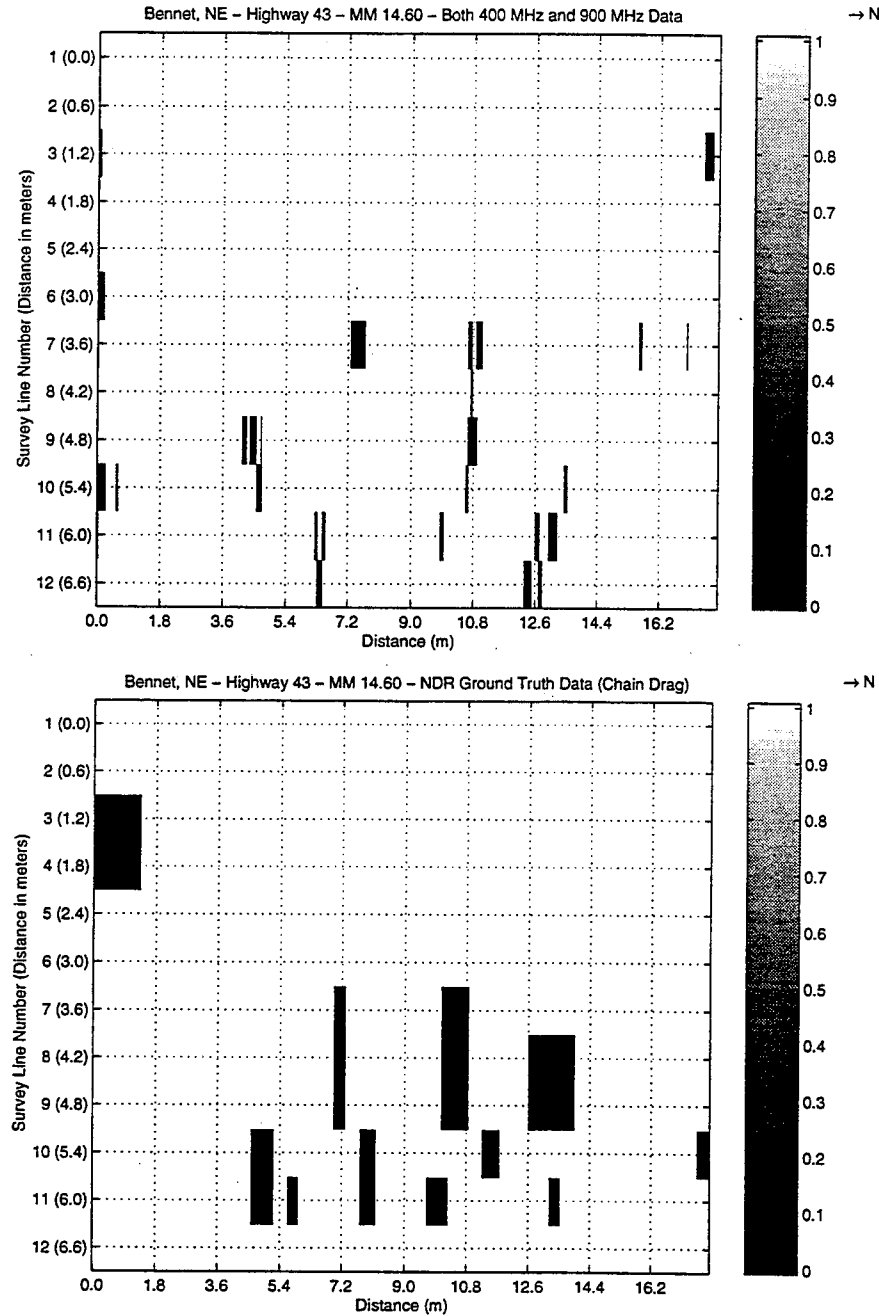


Figure 7.36: 2-D plot representing deterioration areas common to both the 400 and 900 MHz data for the bridge at mile marker 14.60 (Highway 43) (using VTL method). The bottom figure is the ground truth data and is provided for reference.

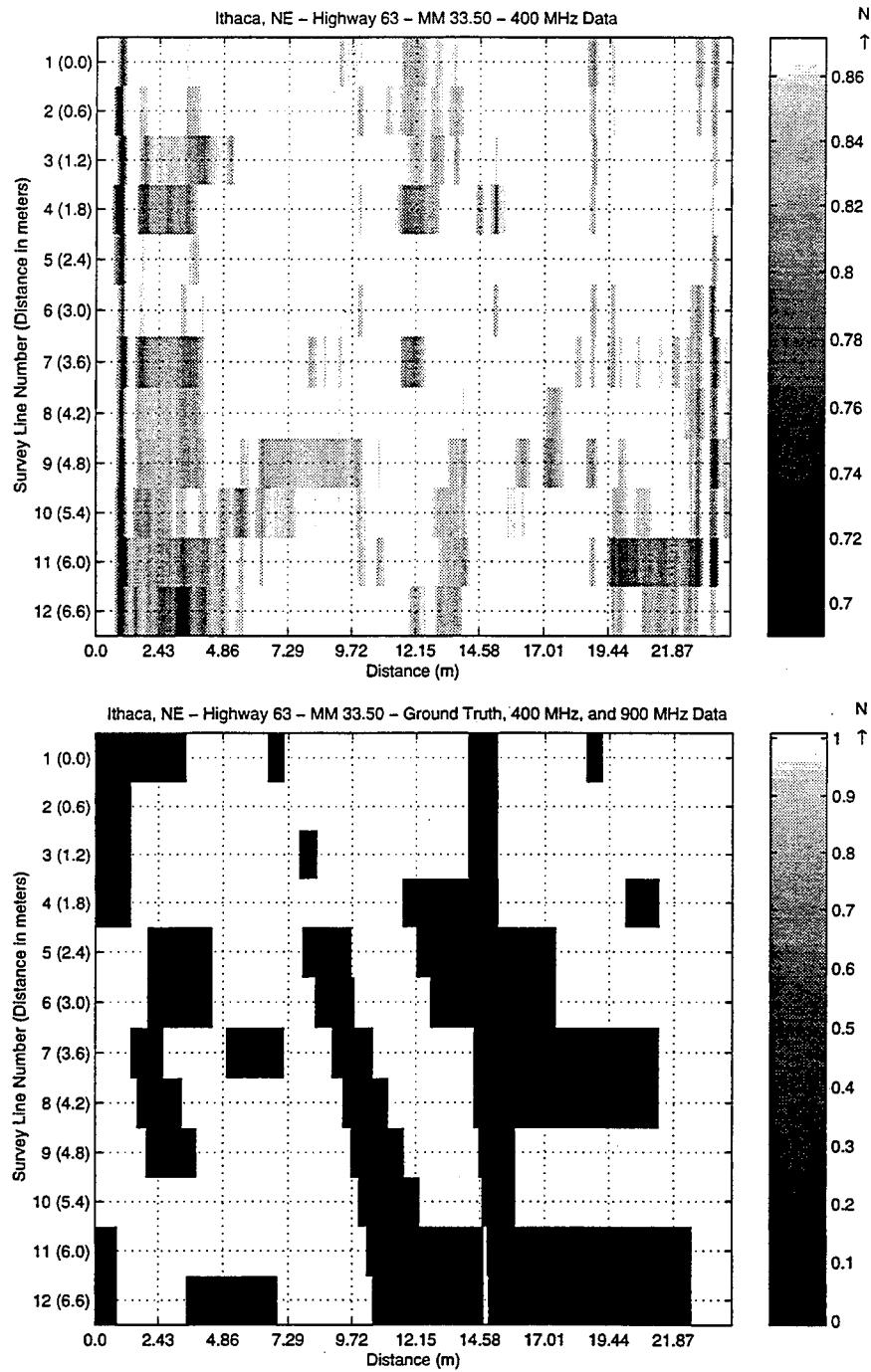


Figure 7.37: 2-D plot representing deterioration areas of the mile marker 33.50 (Highway 63) bridge according to the 400 MHz data (using VTL method). The bottom figure is the ground truth data and is provided for reference.

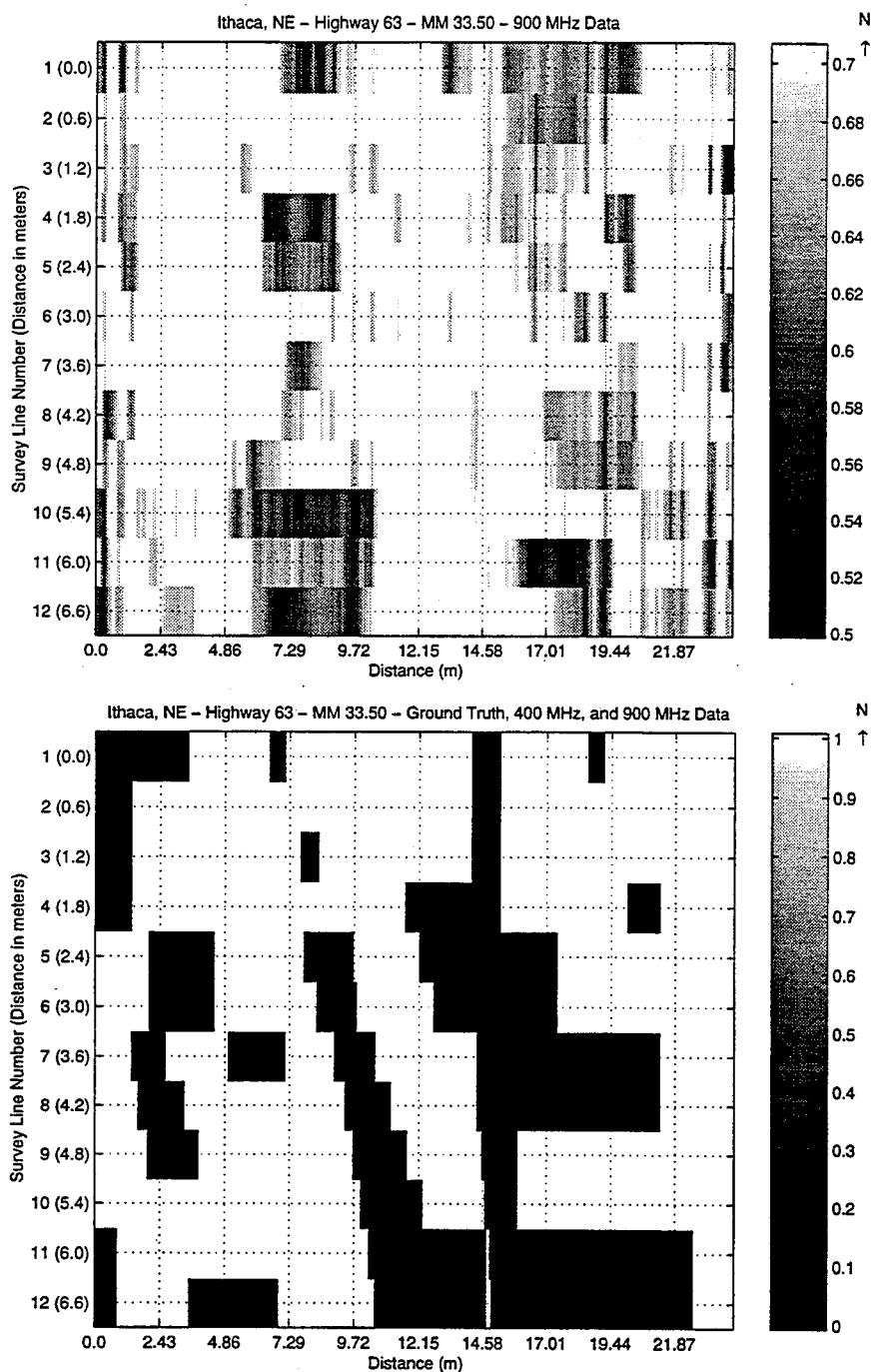


Figure 7.38: 2-D plot representing deterioration areas of the mile marker 33.50 (Highway 63) bridge according to the 900 MHz data (using VTL method). The bottom figure is the ground truth data and is provided for reference.

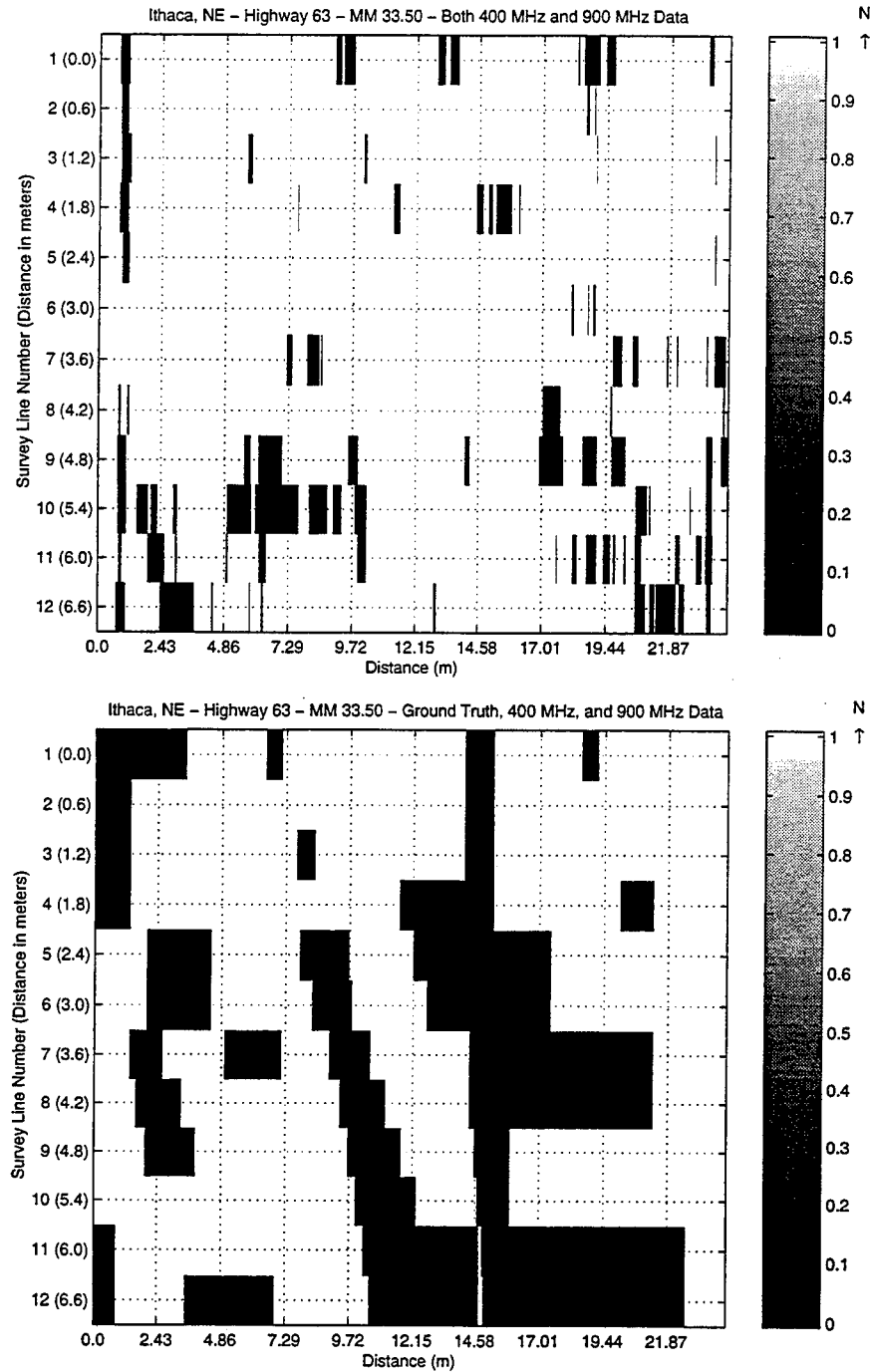


Figure 7.39: 2-D plot representing deterioration areas common to both the 400 and 900 MHz data for the bridge at mile marker 33.50 (Highway 63) (using VTL method). The bottom figure is the ground truth data and is provided for reference.

Chapter 8

Concluding Remarks and Future Research

The focus of this thesis involved using a pulsed, ground-penetrating radar system to detect rebar corrosion, and therefore areas of possible deterioration, in the upper layer of bridge decks. The radar system employed for collecting bridge deck data was the Geophysical Survey System, Inc. SIR System-10B. Both of the available multiplexed transducer channels were utilized. Data were collected on one channel using a GSSI Model 5103 400 MHz antenna, while a GSSI Model 3101D 900 MHz antenna collected data on the other. The purpose of doing this was to compare correlations and discrepancies between the two data sets in an attempt to obtain further insight into the effect of frequency on the results. It was shown that using the variance properties of the return signals, in addition to utilizing the geometric symmetry and repetition of the bridge deck structure, provided a viable means of detecting deterioration areas. Two methods were discussed. The first method, termed the Constant Threshold Level (CTL) method, used a universal threshold level for each frequency to distinguish good rebars from bad rebars. The second, or Varying Threshold Level (VTL), method involved adjusting the threshold levels for each bridge until the percentage of deterioration matched that of the chain drag ground truth data obtained by the Nebraska Department of Roads. Although the methods did not truly distinguish whether or not rebars are corroded, they did identify the extent of corrosion with respect to the least-corroded rebars of the bridge deck. The data were represented using two-dimensional plots representing the top view of the bridge deck. Visual observations of these plots suggest

that the Varying Threshold Level method produced more realistic results than the Constant Threshold Level method.

Results obtained from the Constant Threshold Level method indicated that the threshold levels found from analysis of a model bridge deck were too high, therefore grossly overestimating the amount of rebar corrosion and deterioration within a bridge deck. This suggests that the threshold levels may depend upon the construction of the bridge, namely the rebar layout. If this is the case, threshold levels should be found using a model which closely matches that of the bridge under investigation. It may also be possible that the threshold levels could be found from computer simulations.

The experimental data seemed to match the ground truth data well when viewing the 2-D plots obtained using the Varying Threshold Level method. This method was used to gauge how well the deterioration areas found via the ground truth data matched with the deterioration areas found from the experimental data when the overall percentage of deterioration was equal for both data sets. The bridges located near Ithaca, Nebraska seemed to provide the best results, with almost one-third of the experimental data matching the ground truth data. This may have been due to the fact that these bridges had the highest amount of deterioration, increasing the chances of matching.

The levels of rebar corrosion were referenced to the series of rebars exhibiting the highest mean variance as chosen by the Matlab algorithm within one survey line of the bridge deck. The rebars chosen for the 400 MHz data sets did not match the rebars chosen for the 900 MHz data sets for any of the bridges. This suggests that, *in this case*, the choice of frequency did affect the results. This may be due to the extreme overlap of the 400 MHz return pulses from each interface. It is recommended that a higher frequency antenna, corresponding to a shorter pulse duration, be used for monitoring rebar corrosion. The frequency should be high enough to ensure complete resolution of all subsurface layers, eliminating any possibility of pulse overlaps affecting the results. The highest frequency

antenna that GSSI currently manufactures, and the one recommended for future work, is the Model 4205, a horn antenna pair which operates at 2.5 GHz. Besides providing a much shorter transmit pulse than the two antennas used in this study, the Model 4205 is not a ground-coupled antenna, therefore eliminating any frequency loading effects. It can also be mounted on a rack attached to the vehicle, eliminating the need for a pullcart. The output power, however, is much lower than that of the Model 5103 and Model 3101D antennas.

A factor which may have affected the results was the choice of spacing between survey lines. With the exception of one bridge, all bridges were investigated using a 0.6 m (24 in) survey line spacing. Decreasing the distance between survey lines increases the number of survey lines needed to cover the bridge deck, corresponding to higher resolution of the data obtained. The resolution of the ground truth data is also increased since the information obtained from the 2-D Nebraska Department of Roads plots is interpolated and placed into a matrix equal to the size of the experimental data matrix. The main drawback, however, is the increase in both the amount of memory needed to store the data and the time required to collect, post-process, and analyze the data.

The areas of deterioration found using the chain drag method were estimated by the person performing the survey. Therefore, the exact areas of deterioration may not be exactly marked. This can greatly reduce the chances of the ground truth data matching with deteriorated areas found from the experimental data, especially if the deteriorated areas are small.

Much time could have been conserved if the data were collected using a survey wheel to automatically normalize the distances of all survey line files. Time could have also been saved if all appropriate filters and time window lengths had been set in the field prior to data collection. Although more time would have been required for set-up, much more time would have been saved during post-processing.

The overall results of the GPR system and data analysis algorithms are very encouraging and provides a starting point for future ground-penetrating radar research at the University of Nebraska-Lincoln as applied to civil engineering structures. It is believed that the use of a 2.5 GHz antenna would greatly improve the results. More algorithms need to be written to make the process more automated, user-friendly, and cost-effective. Also, more models need to be constructed to obtain a control data matrix which represents a variety of bridge deck constructions and conditions.

Bibliography

- Arcone, S. A., "Numerical Studies of the Radiation Patterns of Resistively Loaded Dipoles", *Journal of Applied Geophysics*, Vol. 33, Nos. 1-3, pp. 39-52, 1995.
- Carter, C. R., T. Chung, F. B. Holt, and D. G. Manning, "An Automated Signal Processing System for the Signature Analysis of Radar Waveforms From Bridge Decks", *Canadian Electrical Engineering Journal = Revue Canadienne de Genie Electrique*, Vol. 11, No. 3, pp. 128-137, July, 1986.
- Chen, H. L. R., U. B. Halabe, Z. Sami, and V. Bhandarkar, "Impulse Radar Reflection Waveforms of Simulated Reinforced Concrete Bridge Decks", *Materials Evaluation*, Vol. 52, No. 12, pp. 1382-1388, December, 1994.
- Chung, T., C. R. Carter, T. Masliwec, and D. G. Manning, "Impulse Radar Evaluation of Asphalt-Covered Bridge Decks", *IEEE Transactions on Aerospace and Electronic Systems*, Vol. 28, No. 1, pp. 125-137, January, 1992.
- Conyers, L. B., and D. Goodman, *Ground-Penetrating Radar: An Introduction for Archaeologists*, AltaMira Press, Walnut Creek, CA, 1997.
- Daniels, D. J., *Surface-Penetrating Radar*, The Institute of Electrical Engineers, London, United Kingdom, 1996.
- Delea, D., Geologist/Applications Engineer for Geophysical Survey Systems, Inc., Thirteen-page facsimile to Dr. Ram Narayanan of the University of Nebraska - Lincoln Electrical Engineering Department, *Re: Antenna Specifications and Spectra*, October 3, 1996.
- Goodman, D., "Ground-Penetrating Radar Simulation in Engineering and Archaeology", *Geophysics*, Vol. 59, No. 2, pp. 224-232, February, 1994.
- GSSI, *SIR System 10B User's Manual*, Geophysical Survey Systems, Inc., North Salem, NH, 1996.
- GSSI, *SIR System 10B Training Notes*, Geophysical Survey Systems, Inc., North Salem, NH, August, 1995.
- Hall, D. D., Unit Supervisor, Materials and Test Division, Nebraska Department of Roads, Numerous telephone interviews, June-December, 1997.
- Hamran, S.-E., D.T. Gjessing, J. Hjelmstad, and E. Aarholt, "Ground Penetrating Synthetic Pulse Radar: Dynamic Range and Modes of Operation", *Journal of Applied Geophysics*, Vol. 33, Nos. 1-3, pp. 7-14, 1995.

Johnk, C. T. A., *Engineering Electromagnetic Fields And Waves, 2nd Ed.*, John Wiley & Sons, New York, NY, 1988.

Kong, F.-N., and T. L. By, "Performance of a GPR System Which Uses Step Frequency Signals", *Journal of Applied Geophysics*, Vol. 33, Nos. 1-3, pp. 15-26, 1995.

Manning, D. G. and F. B. Holt, "Detecting Deterioration in Asphalt-Covered Bridge Decks", *Transportation Research Record*, Washington, D.C., pp. 10-20, January, 1983.

Olver, A. D., and L. G. Cuthbert, "FMCW Radar for Hidden Object Detection", *IEEE Proceedings. F, Communications, Radar, and Signal Processing*, Vol. 135, Pt. F, No. 4, pp. 354-361, August, 1988.

Skolnik, M. I., *Introduction to Radar Systems, 2nd Ed.*, McGraw-Hill, Inc., New York, NY, 1980.

Smith, S. S. and T. Scullion, "Development of Ground-Penetrating Radar Equipment for Detecting Pavement Condition for Preventive Maintenance", Strategic Highway Research Program Report No. SHRP-H-672, October, 1993.

Warhus, J. P., S. D. Nelson, J. E. Mast, and E. M. Johansson, "Advanced Ground-Penetrating Imaging Radar for Bridge Inspection", Lawrence Livermore National Laboratories, <http://www-dsed.llnl.gov/documents/em/jwpctta93.html> Lawrence Livermore National Laboratories, 1994 (URL valid as of December, 1997).

Warhus, J. P., J. E. Mast, and S. D. Nelson, "Imaging Radar for Bridge Deck Inspection", <http://lasers.llnl.gov/lasers/idp/mir/files/warhus-spie/spiepaper.html>, Lawrence Livermore National Laboratories, 1997 (URL valid as of December, 1997).

Yamaguchi, Y., Y. Maruyama, A. Kawakami, M. Sengoku, and T. Abe, "Detection of Objects Buried in Wet Snowpack by an FM-CW Radar", *IEEE Transactions on Geoscience and Remote Sensing*, Vol. 29, No. 2, pp. 201-208, March, 1991.

